

**IN-CHIP DEVICES FABRICATED WITH
NONLINEAR LASER LITHOGRAPHY DEEP
INSIDE SILICON**

A DISSERTATION SUBMITTED TO
THE GRADUATE SCHOOL OF ENGINEERING AND SCIENCE
OF BILKENT UNIVERSITY
IN PARTIAL FULFILLMENT OF THE REQUIREMENTS FOR
THE DEGREE OF
DOCTOR OF PHILOSOPHY
IN
ELECTRICAL AND ELECTRONICS ENGINEERING

By
Ahmet Turnalı
May 2019

In-chip devices fabricated with nonlinear laser lithography deep inside
silicon

By Ahmet Turnalı

May 2019

We certify that we have read this dissertation and that in our opinion it is fully
adequate, in scope and in quality, as a dissertation for the degree of Doctor of
Philosophy.

Fatih Ömer Ilday(Advisor)

Onur Tokel(Co-Advisor)

Ekmel Özbay

Alpan Bek

David Grojo

Abdullah Demir

Approved for the Graduate School of Engineering and Science:

Ezhan Kardeşan
Director of the Graduate School

ABSTRACT

IN-CHIP DEVICES FABRICATED WITH NONLINEAR LASER LITHOGRAPHY DEEP INSIDE SILICON

Ahmet Turnalı

Ph.D. in Electrical and Electronics Engineering

Advisor: Fatih Ömer Ilday

Co-Advisor: Onur Tokel

May 2019

The integration of photonic elements with electronic elements on the same chip is highly desirable, since it may lead to new generation of devices. One constraint in this direction is the limited space available on the wafer surface. Currently, conventional fabrication methods use only the top thin layer of the silicon platforms for device fabrication. Therefore, new architectural designs are necessary. Creating functional elements deep inside silicon without damaging the surfaces is a promising approach to overcome space bottleneck in electronic-photonic integration, since the bulk of the wafer can be utilized with this method.

Laser-written devices have been demonstrated in various transparent materials, such as glasses and polymers. When focused, high-energy laser pulses can induce nonlinear breakdown and change the morphology of the interaction region enclosed by the material. This process enables the fabrication of a diverse set of devices, including interconnects, optical waveguides and quantum photonic devices. However, so far, similar approaches did not succeed in silicon. We demonstrated a similar enabling method inside silicon, where nonlinear effects were exploited to generate highly controllable modifications deep inside silicon. We used these modifications as building blocks to create in-chip elements.

We developed a simple, intuitive model to understand the structure formation in more detail, which indicated that nonlinear interaction between counter-propagating beams causes the self-focusing of the beam, resulting in disruption in crystal structure. Propagation of the pulses are reconfigured by the previously modified region. The focal point of the pulse shifts, elongating the structure. These elongated structures can provide the necessary phase shift to build diffractive optical elements embedded in Si, among other optical elements. We demonstrated this concept by fabricating binary and grayscale Fourier holograms and a binary Fresnel hologram projecting four layers forming a 3D image. In an extension of this work, the algorithm is developed for greyscale Fresnel holograms and

increased the possible numbers of projections layers three orders of magnitude. Moreover, we used in-chip modifications for creating optical waveguides inside silicon with the lowest losses reported so far. By selectively etching the modifications, we showed a second set of applications. We sculpted the silicon with this method to fabricate micropillars, through-Si vias and microfluidic channels. Further, we extended the method to other semiconductors and nanostructured the bulk GaAs. We also investigated the possibility of new processing regimes by using Bessel beams and 2 μm laser pulses.

Keywords: silicon, subsurface, three dimensional, laser processing, in-chip, computer generated hologram, waveguide, selective etching.

ÖZET

DOĞRUSAL OLMAYAN LAZER LİTOGRAFİSİ İLE SİLİSYUM İÇERİSİNDE YONGA-İÇİ AYGITLARIN ÜRETİLMESİ

Ahmet Turnalı

Elektrik-Elektronik Mühendisliği, Doktora

Tez Danışmanı: Fatih Ömer İlday

İkinci Tez Danışmanı: Onur Tokel

Mayıs 2019

Fotonik elemanların elektronik elemanlarla aynı çip üzerinde birleştirilmesi, yeni nesil cihazlara yol açabileceği için oldukça arzu edilir. Bu yöndeki bir kısıtlama, yonga plakası yüzeyinde mevcut sınırlı alandır. Günümüzde, geleneksel üretim yöntemleri, cihaz imalatında yalnızca silisyum platformların en üst ince katmanını kullanmaktadır. Bu nedenle, yeni mimari tasarımlar gereklidir. Yüzeyle zarar vermeden silisyumun derinliklerinde işlevsel elemanlar oluşturmak, yonga plakasının tamamını erişime açacağından, elektronik-fotonik entegrasyonda alan darboğazını aşmak için umut verici bir yaklaşımdır.

Lazerle yazılan cihazlar, cam ve polimer gibi çeşitli saydam malzemelerde gösterilmiştir. Odaklandığında, yüksek enerjili lazer darbeleri, doğrusal olmayan kırılmaya neden olabilir ve malzeme tarafından çevrelenmiş etkileşim bölgesinin yapısını değiştirebilir. Bu işlem, optik ara bağlantılar, optik dalga kılavuzları ve kuantum fotonik aygıtlar dahil olmak üzere çeşitli aygıtların üretimini mümkün kılar. Bununla birlikte, şimdiye kadar, benzer yaklaşımlar silisyumda başarılı olamadı. Bu tezde, silisyum içinde yüksek oranda kontrol edilebilir modifikasyonlar üretmek için doğrusal olmayan etkilerin kullanıldığı benzer bir üç-boyutlu etkinleştirme yöntemi gösterdik. Bu değişiklikleri yonga-ıç elemanlar oluşturmak için yapıtaşları olarak kullandık.

Yapı oluşumunu daha ayrıntılı olarak anlamak için basitleştirilmiş bir model geliştirdik. Bu model, karşı-yayılan ışınlar arasındaki doğrusal olmayan etkileşimin ışının özodaklanmasına neden olduğunu ve kristal yapısında bozulmaya yol açtığını işaret etti. Bir sonraki atımın yayılması, daha önceden değiştirilmiş bölgenin odak noktalarını kaydırması ile, yeniden yapılandırılarak yapı daha da uzatılır. Bu uzatılmış yapılar, diğer optik elemanlarla beraber Si içine gömülü kırınımlı optik elemanlar oluşturmak için gerekli faz kaymasını

sağlayabilir. Bu kavramı, ikili ve gri tonlamalı Fourier hologramları ve üç boyutlu bir görüntü oluşturan dört katmanlı yansıtan ikili Fresnel hologramı üreterek gösterdik. Ayrıca, gri tonlamalı Fresnel hologramları için bu algoritmayı daha da geliştirdik ve mümkün olan izdüşüm katmanlarını yaklaşık bin kat arttırdık. Ayrıca, şu ana kadar bildirilen en düşük kayıplarla silikon içinde optik dalga kılavuzları oluşturmak için yonga-içi değişiklikleri kullandık. Değişiklikleri kimyasal seçici bir şekilde yaparak ikinci bir uygulama grubu gösterdik. Bu yöntemle silisyumu, mikrosütunlar, Si-yolu ve mikroakışkan kanalları imal etmek için yonttuk. Dahası, yöntemi diğer yarı iletkenlere genişlettik ve GaAs'ın yüzey altını nanoyapılandırdık. Ayrıca Bessel ışınlarını ve $2 \mu\text{m}$ 'luk lazer atımlarını kullanarak yeni işleme rejimlerinin olasılığını da araştırdık.

Anahtar sözcükler: silikon, yüzey altı, üç boyutlu, lazer işleme, yonga-içi, bilgisayar ürünü hologram, dalga kılavuzu, seçici yontma.

Acknowledgement

I would like to thank my supervisors F. Ömer Ilday and Onur Tokel for their continuous support, guidance and patience during my studies.

I would like to express my gratitude to Hamit Kalaycıođlu, Parviz Elahi and Ghaith Makey for their help at the critical stages of my thesis.

I would like to thank Denizhan Koray Kesim, Özgün Yavuz, Ali Murat Sözen, Aqıq Ishraq, Rana Asgari Sabet, Mertcan Han, Gizem Gençođlu for scientific and non-scientific discussions.

I would like to thank Petro Deminskyi, Tahir Çolakođlu and Mona Zolfaghari Borra for their efforts in chemical etching of silicon.

I would like to thank my committee members Ekmel Özbay, Alpan Bek, David Grojo and Abdullah Demir for reviewing my thesis.

I acknowledge the financial support from TÜBİTAK BİDEB for my PhD studies.

Contents

1	Introduction	1
2	Theoretical background of subsurface modifications inside silicon	5
2.1	Carrier generation and recombination mechanisms in silicon . . .	6
2.2	Heat generating mechanisms and temperature profile in silicon . .	9
2.3	Propagation of light in silicon	11
2.4	Light propagation under nonlinear feedback conditions	13
2.4.1	Single-pulse model implementation	13
2.4.2	Single-pulse simulation results	15
2.5	Description of the theoretical model	17
3	In-chip computer generated holograms (CGH)	23
3.1	Generation of CGHs with a modified iterative Fourier algorithm .	24
3.2	Implementation of the holograms	28
3.3	Development of a new algorithm for dynamic hologram generation	32
4	Laser-written waveguides deep inside silicon	36
4.1	Laser-written depressed-cladding waveguides inside bulk silicon . .	37
4.1.1	Waveguide fabrication	38
4.1.2	Optical characterization	41
4.2	Femtosecond laser written waveguides deep inside silicon	46
5	3D sculpting in Si with preferential etching	50
5.1	Chemical etching process	51
5.2	Examples of applications with developed etchant	52

5.2.1	Micropillar arrays	52
5.2.2	Through-Si vias	53
5.2.3	Cantilever-like structures	54
5.2.4	Silicon slicing	55
5.2.5	Microfluidic channels	56
6	Investigation of new processing regimes for in-chip structures	58
6.1	Spatial-control of laser-written in-chip Si structures with Bessel beams	59
6.1.1	Bessel beam generation	59
6.1.2	In-chip structures and characterization	61
6.2	Processing at 2 μm	63
6.2.1	Results	63
6.2.2	Development of burst-mode thulium system	65
6.3	Subsurface structuring of GaAs	67
7	Conclusion	71
A	Paraxial approximation for nonlinear wave equation	91

List of Figures

2.1	We used experimental parameters to show carrier density evolution. The black curve is the laser intensity profile, and the red curve is the carrier density profile.	8
2.2	For each temporal slice, we calculated the intensity distribution (I_{env}) using the refractive index, temperature and carrier distributions from the previous iteration.	14
2.3	(a) Intensity distribution for the undressed beam case. (b) Intensity distribution of the dressed beam case. (c) Intensity evolution in the modification region. The blue curve represents the dressed beam case, and the red curve is for the undressed case. The double peak is because of the delay in the thermal lensing, which becomes effective a few ns after FCI. This indicates the competition between the two effects. (d) Thermal evolution in the modification region. In the dressed beam case (blue curve), temperature reaches the melting temperature of silicon, whereas in the undressed beam case (red curve), maximum temperature is limited to 800 K. . . .	16
2.4	(a) Schematic showing the pulse propagation for the cases with and without counter-propagating beam. We coated 200 nm thick Si_3N_4 to prevent reflection so that the focused beam can pass through the back surface without any reflection. (b) IR transmission microscope images of the subsurface structures, which are formed only in the double-side polished region.	21
2.5	Measured structure lengths (red circles) are good agreement with the model's prediction (blue line).	22

3.1 Quality comparison of images reconstructed with different algorithms. (a) The original image. The rest is the simulation result of the constructed image of (b) grayscale kinoform (256 Levels) generated by adaptive-additive IFTA. (c) binary kinoform generated without IFTA. (d) binary kinoform generated with binarized adaptive-additive IFTA. (e) binary kinoform generated with binarized adaptive-additive IFTA after increasing noise space. 25

3.2 Flow of the modified adaptive-additive iterative Fourier algorithm. The final hologram is implemented inside Si. 27

3.3 Optical reconstruction setup for the Fourier holograms embedded inside silicon. 29

3.4 Implementation of binary hologram and the experimental reconstruction. (a) The original image with high spatial frequency components. (b) Full hologram designed with the modified algorithm. Inset shows the zoomed in version. (c) IR microscope image of a portion of the embedded hologram in Si. (d) The simulation of the reconstructed image. (e) Experimentally reconstructed image. . . 30

3.5 Implementation of *Mona Lisa* hologram and the experimental reconstruction. (a) The original grayscale image. (b) Full hologram designed with the modified algorithm. Inset shows the zoomed in version. (c) IR microscope image of a portion of the embedded hologram in Si. (d) The simulation of the reconstructed image. (e) Experimentally reconstructed image. 31

3.6 Illustration of the optical setup for Fresnel image reconstruction. We expanded the beam to from a larger image for capturing. Each slice of the total image is separated from each other by approximately 7 cm. 32

3.7 (a) Normalized inner product of two checkerboard patterns as a function of pixel number N . Both images have random phase between $0-2\pi$. As N increases, their inner product approximates to zero, indicating orthogonality. (b) Comparison of two-plane projection simulations generated with and without random phase. Adding random phase eliminated the crosstalk between the images. 33

3.8	(a) Illustration of the optical setup used in image reconstruction. (b) Simultaneous projection of high-resolution grayscale images. Target planes are separated by 15 cm. (c) Recorded image of a four-layer projection of a rotating cube.	34
4.1	(a) Schematic of the experimental setup for waveguide fabrication and <i>in-situ</i> imaging of the writing process. A nanosecond laser operating at $1.55 \mu\text{m}$ is used for device fabrication and IR transmission microscope is used for characterization. MOPA: Master-Oscillator Power Amplifier; HWP: half-wave plate; PBS: polarizing beam splitter. (b) IR transmission microscope image of a single-line modification. Laser entrance surface is the polished side surface (x - y plane) and laser propagation direction is z -axis. To elongate the structures, scanning direction is set along the laser propagation direction.	39
4.2	(a) Illustration of the longitudinal-writing scheme to form tubular waveguides. (b) IR transmission microscope image showing the exit ports of an array of waveguides. (c) IR image of the top view of a single waveguide.	41
4.3	(a) The near-field image of the coupled light from the waveguide output taken with $60\times$ objective. (b) Near-field intensity profile data measured from (a). Blue circles and red crosses correspond to measured data from horizontal axis and vertical axis, respectively. Solid curves are Gaussian fits to the measured data of the same color.	43
4.4	(a) Far-field image of the uncoupled light, after passing through unmodified silicon (control experiment). (b) Far-field image of the coupled light. (c) Far-field intensity profiles measured from coupled light (blue crosses) and uncoupled light (black circles). Solid curves are Gaussian fits to the measured data of the same color.	44
4.5	Scattered light intensity (orange dots) is used to characterize the waveguide loss. 10-pixel moving average filter is applied to get the general profile. Blue curve represents the fitted curve.	45

4.6 IR images obtained with InGaAs camera when the waveguide is located (a) 200 μm away from the focal plane closer to the camera, (b) 200 μm further away from the imaging plane. (c) Using such IR images and inverse Abel transform Δn profile is calculated. Red solid line is obtained from the average of the five waveguides, whereas black dashed lines show individual measurements. 47

4.7 (a) i. Far-field image of the uncoupled light (control experiment), ii. Far-field image of the coupled light, iii. Near-field image of the coupled light. (b) Far-field intensity profiles measured from coupled light (blue circles) and uncoupled light (orange crosses). Solid curves are Gaussian fits to the measured data of the same color. 48

5.1 (a) SEM image of the cross-section of the laser processed region before etching. Laser propagation direction is $+z$. (b) Cross-section SEM image of the modified region after 10 minutes of KOH etching. (c) Cross-section SEM image of the modified region after treated with the developed etchant. Due to high selectivity, the etched region has a sharp contrast. 52

5.2 SEM image of the high-aspect ratio pillars covering 1.5 mm \times 1 mm area. The inset is the zoomed-in image of a portion of the same area. 53

5.3 (a) A single circular motion is enough for the laser processing of vias. (b) An array of cylinders can be created in large area. (c) After polishing both sides of the sample, Si wafer is placed into etchant for two minutes. (d) Highly uniform array of vias can be obtained with the method. 54

5.4 SEM image of through-Si-vias that cut across the entire chip. . . 55

5.5 (a) Cantilever length can be designed during the scanning and can be few millimeters long. (b) SEM image of the 30 μm -thick walls. 55

5.6 (a) Cross-section SEM image of the sliced Si during etching before it is fully detached. (b) SEM image of the sliced sample after etch treatment. 56

5.7 (a) The illustration of the cooling experiment. Inset shows the temperature profile before (i) and after (ii). (b) SEM image of a buried microfluidic channel. 57

6.1 The schematic showing the experimental setup for generating Bessel beam. MOPA: Master-oscillator-power-amplifier; M1- M3: silver mirrors; L1- L4: plano-convex lenses; HWP: half-wave plate; PBS: polarizing beam splitter; SLM: Spatial light modulator. 60

6.2 (a) Simulation of transverse profile of a Bessel pattern at the focal point of the aspheric lens. (b) Horizontal intensity profile of the pattern shown in (a). 61

6.3 Infrared transmission microscope images of longitudinally-written structures from the top. In-chip structures written using Bessel beam with core diameter (a) $\sim 1 \mu\text{m}$ and (b) $3 \mu\text{m}$. Scale bar is $10 \mu\text{m}$ for both images 62

6.4 SEM images of transversely written structures from the cross-section. (a) Submicron structures written using Bessel beam with core diameter of $\sim 1 \mu\text{m}$. (b) Zoomed-in image showing 150-nm void. 63

6.5 IR microscope images of in-chip modifications written with $2 \mu\text{m}$ pulses. Pulse energies are (a) $10 \mu\text{J}$ and (b) $1 \mu\text{J}$ 64

6.6 Schematic of the burst-mode Tm fiber laser system. 66

6.7 (a) Output spectrum is centered around 1980 nm. (b) Pulse duration is measured as 15 ps. 66

6.8 Effect of the pulse energy on the structures, (a) When the pulse energy is close to the modification threshold, random modifications are formed. (b) Above the threshold energy, modifications get more continuous with relatively lower uniformity. (c) Uniformity increases as the energy increases further. Laser propagation direction is +z, scanning direction is alternating between +y and -y with each line. 69

6.9 SEM image of nanogratings (a) Cross-section image of the buried structures. (b) Zoomed in image of periodic nanostructures in (a). (c) Towards the end of the modification, single nanostructures are also possible. Laser propagation direction is z, scanning direction is y. 70

Chapter 1

Introduction

Capability of fabricating optical elements that manipulate and detect light on the same chip with electronic elements is a critical step in the direction of new generation microchips [1–3]. However, until recently a method to induce structural modifications or creating functional elements deep inside Si did not exist. Such an approach is highly desirable, since successful integration of photonics and data-transfer elements created inside Si wafers with conventional electronic circuits may lead to new generations of devices. Currently, silicon-on-insulator (SOI) platform is the main architectural approach for fabricating optical elements for Si-photonics applications [3]. In this platform, conventional techniques such as e-beam lithography and chemical etching are used to fabricate active and passive optical elements on wafer surface. In spite of its remarkable successes, this approach uses only the top thin layer of SOI platform, wasting the bulk of the wafer for positioning functional elements.

Different functionalities have been obtained with laser writing methods by patterning silicon surface. Laser diffraction on silicon surface can create micropillar arrays and surface ripples [4, 5]. Surface treatment of silicon with lasers can increase the infrared light absorption, making them desirable in thermal imaging and photovoltaic applications [6, 7]. Similarly, laser treatment can modify the surface properties and can turn the silicon superwicking [8]. These examples

demonstrate that optical and physical properties of silicon can be controlled by laser-silicon interaction. However, these effects take place on the surface.

A promising approach for fabricating three-dimensional, embedded structures is through laser micro-fabrication of transparent materials [9]. Variants of these 3D techniques have been extensively applied to glasses and polymers in the past decade [10]. In these methods, depending on the time scale, intensity and energy of the laser pulse, photons can nonlinearly transfer their energy to the medium to create a seed electron population (i.e., multi-photon ionization) and also to phonons to induce a nonlinear breakdown [11, 12]. The exploitation of these processes have allowed the fabrication of various optical devices, including waveguides [13], optical interconnects [14], resonators [15] and quantum photonic circuits [16], buried in the bulk of materials, such as glasses and lithium niobate crystals, with important applications in integrated optics [17, 18]. In an analogous but distinct fashion, such an enabling technique is recently demonstrated for Si [19], where, first, nonlinear optical effects are used to create controlled structures deep inside in Si [20, 21], and second, these structures are engineered to create functional in-chip elements, without altering the wafer surface.

In previous attempts to modify the bulk of the silicon, mostly ultrafast lasers have been used. The earliest attempt in this field was done to create optical waveguides [22]. However, the waveguides could be written in a very narrow region close to the surface, not in the whole wafer. Following efforts failed in forming fully buried modifications without surface damage due to absorption or plasma-shielding [23, 24]. To reach the modification threshold, pulse energies were increased to 90 μJ but, this approach did not succeed in inducing subsurface modifications. Nonlinear dynamics of these processes are analyzed in detail in several studies [25, 26]. Therefore, the range of modifications were limited to either interfaces [22] or close to the backsurface [27].

Possibility of fabricating subsurface modifications inside silicon was shown using nanosecond pulses and first reported in Ref. [28, 29]. Similar studies confirmed the initial results [30]. So far, device types fabricated inside silicon with nanosecond pulses remained limited and only optical waveguiding with positive refractive

index change was demonstrated [31] as an addition to our studies [19, 32].

In this thesis, we report the generation of laser induced rod-like structures with adjustable lengths deep inside silicon. We demonstrate, both numerically and experimentally, that a feedback mechanism plays a role in the formation of these high aspect ratio structures. Further, we use the “in-chip” structures as building blocks in fabrication of numerous photonic devices, including holograms and waveguides. The morphological difference created with the laser exposure enables selective etching, which we utilize for silicon sculpting. With this procedure, we demonstrate 3D structures such as micropillars, vias and microchannels.

In chapter 2, we explain the effective physical mechanisms in modification formation. Specifically, we give details about how carrier and temperature profiles evolve when nanosecond laser pulses interact with silicon. We also propose a simple model that shows why counter-propagating beams create in-chip structures and how structures elongate.

Chapter 3 contains the algorithm we developed for in-chip hologram generation and their implementation. We demonstrate the first diffractive elements fully buried inside silicon, binary Fourier and Fresnel holograms, and optically characterize them. An algorithm that enhances state-of-art 3D projection is presented in this chapter.

In chapter 4, we present two types of optical waveguides, depressed cladding waveguides written by using nanosecond laser and type-I waveguides, where waveguide core is laser-written, with femtosecond laser. We give details about their fabrication process and their optical properties.

Chapter 5 constitutes the results of selective etching of the laser modified regions and the microstructures as the final products. We describe the etchant and demonstrate micropillars, through-Si vias, silicon slicing and chip cooling with microfluidic channels.

In chapter 6, we investigate different regimes for creating in-chip structures. We give details about our studies in structure formation with Bessel beams and

nanosecond pulses with 2 μm wavelength. We demonstrate nanostructuring in bulk GaAs with a similar method we developed.

Chapter 2

Theoretical background of subsurface modifications inside silicon

In order to generate in-chip modifications, specifically to fabricate rod-like, high aspect ratio modifications inside Si, we utilize nonlinear interactions between silicon and the nanosecond pulses. The approach we take is an extension of nonlinear laser lithography (NLL), which exploits nonlinear feedback mechanisms in 2D [33]. This enables us to form structures at any position in the bulk Si, without damage on the wafer surfaces. In this chapter, we explain the physical mechanism and give background information about the concepts regarding the structure formation.

2.1 Carrier generation and recombination mechanisms in silicon

Carrier dynamics is the driving force that effects thermal profile and pulse behavior inside Si. Consequently, to fully understand the structure formation, first we investigate the free electron generation and recombination mechanisms in Si to get carrier profile. Following that we analyze how this profile contributes to the nonlinear effects in pulse propagation, such as thermal focusing and diffraction.

Linear absorption of silicon decreases to zero for the wavelengths higher than $1.12 \mu\text{m}$. If the intensity is high enough, an electron can be excited to the conduction band by two-photon absorption (TPA). Coefficient of the absorption varies with the intensity and result in an intensity profile different than predicted by Beer-Lambert Law. Diffusion and recombination of the generated carriers in Si changes the profile as well. Therefore, we should analyze all these mechanisms in Si.

In our experiments, free carriers are generated with photo-ionization processes, especially with the TPA process. In this process, to generate an electron-hole pair, two photons must be absorbed simultaneously. The carrier generation rate in that case is calculated as $\xi = \beta_2 I(t)^2 / 2hf$, where β_2 is the TPA coefficient, $I(t)$ is the instantaneous intensity, h is the Planck constant and f is the photon frequency. Considering no recombination and Gaussian light source, the carrier density is given as:

$$N_{\text{avg}} = \int_{-\infty}^{\infty} \xi(t) dt = \int_{-\infty}^{\infty} \frac{\beta I(t)^2}{2hf} dt = \int_{-\infty}^{\infty} \frac{\beta I_0^2 \exp(-2t^2/\tau_{\text{pulse}}^2)}{2hf} dt = \frac{\sqrt{\pi} \beta I_0^2}{2\sqrt{2}hf} \tau_{\text{pulse}}, \quad (2.1)$$

where I_0 is the peak intensity and τ_{pulse} is the pulse duration. For the experimental parameters we use ($\tau_{\text{pulse}} = 3 \text{ ns}$, $P_{\text{avg}} = 2 \text{ W}$, $w_0 = 3 \mu\text{m}$), we expect to reach carrier density in the order of 10^{21} cm^{-3} , which would be above the critical density for modification. We use the calculated upper limit of the carrier density to decide which relaxation mechanism is dominant. In the recombination processes,

radiative mechanism is limited due to silicon's indirect bandgap [34]. Therefore, we neglect radiative and Shockley-Read-Hall (SRH) processes in our calculations [35]. Auger recombination plays a major role for the carrier densities $N > 10^{18}$ - 10^{19} cm^{-3} . This mechanism also prevents the carrier density to reach the upper limit.

Therefore, we can modify the rate equation of the free carrier density as:

$$\frac{dN}{dt} = \frac{\beta I^2}{2hf} \left(1 - \frac{N}{N_{at}}\right) - \gamma_3 N^3, \quad (2.2)$$

where N_{at} is the atomic density in the crystal and γ_3 is the Auger recombination constant [36]. First term in the right-hand side of the equation represents the carrier generation due to TPA and the second term is the Auger recombination. We can calculate the recombination time using $\tau_{rec} = 1/\gamma_3 N^2$, which is comparable to the pulse duration for $N \approx 10^{19} \text{ cm}^{-3}$. Thus, pulse length and average carrier density determine the time scale of the carrier density evolution. We confirm this claim by solving Eq. 2.2 numerically. It is shown in Fig. 2.1 that the carrier density is in the range of $10^{19} - 10^{20} \text{ cm}^{-3}$. Moreover, the carrier density profile has the same trend with the pulse profile.

Next, we consider the effect of diffusion on the carrier density. Diffusion should be included in the equations, if the carriers are able to exit the interaction region during the excitation or before they recombine. Therefore, we need to compare the diffusion length in that time period with the beam diameter at the focal plane. Diffusion length is given as, $L_{diff} = \sqrt{6D\tau_{pulse}} \ll w_0$, where D is the diffusion constant and S is the beam diameter. For silicon, $D_{carrier} = 2k_B T_e \mu_e \mu_h / (e(\mu_e + \mu_h))$, where k_b is the Boltzmann constant, T_e is the electron temperature, μ_e is the electron mobility and μ_h is the hole mobility. At $T = 300 \text{ K}$, L_{diff} is calculated as $1.8 \mu\text{m}$, smaller than $w_0 = 3 \mu\text{m}$. Carrier mobilities of Si decreases as the temperature increases [37], further reducing the diffusion length. Thus, we can neglect diffusion in Eq. 2.2.

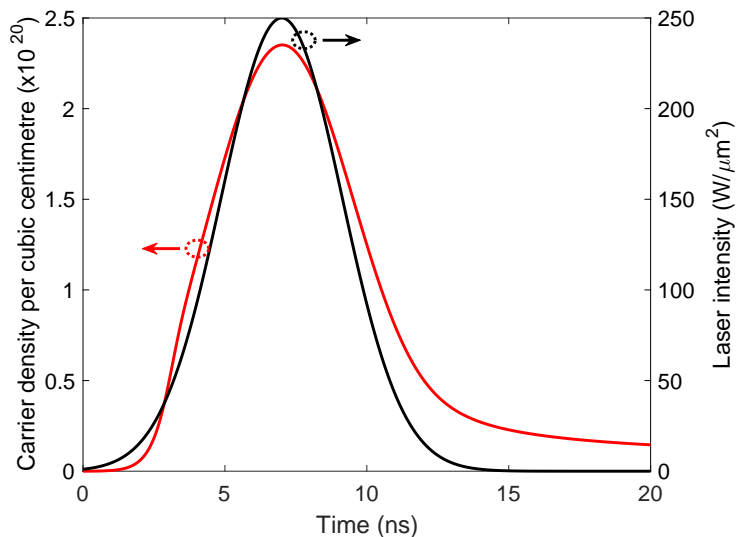


Figure 2.1: We used experimental parameters to show carrier density evolution. The black curve is the laser intensity profile, and the red curve is the carrier density profile.

A similar simplification is valid for the avalanche ionization in carrier generation. In avalanche ionization, a free carrier can transfer some of its energy to an electron in the valence band and create an electron-hole pair. The process can be added to Eq. 2.2 as:

$$\frac{dN}{dt} = \left(\frac{\beta I^2}{2hf} + \delta\right)\left(1 - \frac{N}{N_{at}}\right) - \gamma_3 N^3. \quad (2.3)$$

where δ is the avalanche ionization coefficient. δ is written as the function of electron temperature and given as, $\delta(T_e) = 3.6 \times 10^{10} \exp(-1.5E_g/k_B T_e)$, where T_e is the electron temperature and E_g is the bandgap energy. Physically, impact ionization is the inverse of Auger recombination. For impact ionization to be effective in the carrier generation, it should cancel out the Auger recombination. The maximum generation rate due to impact ionization is $\sim 2 \times 10^5 \text{ cm}^3\text{s}^{-1}$ at $T = 1600 \text{ K}$ (silicon melting temperature). However, Auger recombination rate is equal to that value for the intensities as low as $\sim 7 \times 10^{17} \text{ cm}^{-3}$. As we demonstrated earlier, carrier densities are two orders of magnitude higher than this equilibrium density, eliminating avalanche ionization as an effective

mechanism for carrier generation. Therefore, Eq. 2.2 stands out as the final rate equation for the carrier densities.

2.2 Heat generating mechanisms and temperature profile in silicon

Similar to the analysis for the carrier density profile in section 2.1, we have to investigate heat generation and diffusion mechanisms to get the thermal profile in silicon. Heat equation governs the temperature behavior and it is written as:

$$\rho C_p(T) \frac{dT}{dt} - \nabla \cdot (\kappa \nabla T) = Q, \quad (2.4)$$

where ρ is the Si density (2.33 g/cm³), $C_p(T)$ is the specific heat [38], κ is the thermal conductivity (1.6 W/cm K) [39], T is lattice temperature and Q is the heat generation rate. Since $L_{\text{diff}} = \sqrt{6D_{\text{heat}}\tau_{\text{pulse}}} \ll S$, where S is the laser spot size, $D_{\text{heat}} = \frac{\kappa}{\rho C_p}$, heat generation translates to ΔT .

While modeling the temperature profile, we did not use two-temperature model due to following: During the interaction, first, electrons gain energy due to laser and through electron-electron collisions, they are thermalized. With that process, electrons become a heat source for the lattice. Electron-phonon coupling neutralize the temperature difference between the lattice and the carriers. For Si, thermal relaxation of the electrons take 500 fs [40]. In our case, we can assume thermal equilibrium between the lattice and the electron, since we use nanosecond pulses in our experiment, which is much larger than the relaxation time. This assumption makes two-temperature model unnecessary.

Therefore, we can list the effective heat generation mechanisms in Si as follows:

- 1. Two-photon absorption based heating:** The difference between the energy of two absorbed photons and the bandgap of Si heats the sample. The rate

due to this process is:

$$Q_{\text{TPA}} = \beta I^2 \left(1 - \frac{N}{N_{\text{at}}}\right) \left(1 - \frac{E_{\text{gap}}}{E_{\text{photon}}}\right). \quad (2.5)$$

where E_{gap} is the band gap energy and E_{photon} is the total energy of the absorbed photons.

2. Heating due to Auger recombination: In Auger recombination, transferred energy to another free carrier as the result of recombination increases the heat. Heating rate due to this mechanism is [41]:

$$Q_{\text{rec}} = E_{\text{gap}} \gamma_3 N^3, \quad (2.6)$$

3. Free carrier absorption (FCA) based heating: The free carriers generated by any of the mechanisms we discussed in 2.1 can continue absorbing energy. Therefore, this intraband absorption can generate a nonlinear absorption profile, which leads to heating. FCA decreases the real part of the refractive index due to Kramers-Kronig relations, known as free carrier index (FCI) change.

We can use Drude model to estimate the changes in FCA ($\Delta\alpha_{\text{FCA}}$) and in FCI (Δn_{FCI}), specifically their temperature dependence [42]:

$$\Delta\alpha_{\text{FCA}} = \frac{e^3 \lambda^2 \Delta N}{4\pi^2 c^3 \epsilon_0 n} \left(\frac{1}{m_{\text{ce}}^*{}^2 \mu_{\text{e}}} + \frac{1}{m_{\text{ch}}^*{}^2 \mu_{\text{h}}} \right) \quad (2.7)$$

$$\Delta n_{\text{FCI}} = -\frac{e^2 \lambda^2 \Delta N}{8\pi^2 c^2 \epsilon_0 n} \left(\frac{1}{m_{\text{ce}}^*} + \frac{1}{m_{\text{ch}}^*} \right) \quad (2.8)$$

where c is the speed of light, ϵ_0 is the vacuum permittivity, n is the refractive index and m_{ce}^* and m_{ch}^* are the effective masses of electrons and holes, respectively. From the Eq. 2.7 and Eq. 2.8, it is seen that both $\Delta\alpha_{\text{FCA}}$ and Δn_{FCI} depends on the carrier density (ΔN) linearly. The only temperature dependent terms that modify these effects are mobilities ($\mu_{\text{e}}, \mu_{\text{h}}$) and the effective masses ($m_{\text{ce}}^*, m_{\text{ch}}^*$)

of the carriers. For silicon, effective masses change by the band structure and weakly depend on the temperature, whereas the carrier mobilities are strongly temperature dependent. Therefore, we expect Δn_{FCI} not to change with temperature. We calculated that Δn_{FCI} changes only 15 %, when the temperature is increased from room temperature to silicon's melting temperature ($T = 1600$ K), confirming our assumption.

In the literature, experimental formulation of $\Delta\alpha_{\text{FCA}}$ and Δn_{FCI} are given as [43]:

$$\Delta\alpha_{\text{FCA}} = \Delta\alpha_{\text{h}} + \Delta\alpha_{\text{e}} = 0.51 \times 10^{-20} \lambda^2 T N + 1.01 \times 10^{-20} \lambda^2 T N, \quad (2.9)$$

$$\Delta n_{\text{FCI}} = -[8.8 \times 10^{-22} N + 8.5 \times 10^{-18} N^{0.8}], \quad (2.10)$$

where T is the equilibrium temperature, showing no temperature dependence of Δn_{FCI} . The heating rate due to the FCA is written as $Q_{\text{FCA}} = \Delta\alpha_{\text{FCA}} I$.

The total heat generation rate is the summation of all the mechanisms explained here and it is calculated as $Q = Q_{\text{TPA}} + Q_{\text{rec}} + Q_{\text{FCA}}$. It should be noted that we have nonlinearities in the heat generation due to the carrier interaction, similar to nonlinearity of light absorption. We can exploit these mechanisms to generate energy localization for creating in-chip Si structures.

2.3 Propagation of light in silicon

Pulse propagation inside silicon and interaction of counter-propagating beams can be obtained by solving Maxwell equations with the methods such as Finite Element Method (FEM) or Finite Difference Time Domain (FDTD). However, coupled mechanisms of carrier and heat generations increases complexity of these techniques. Moreover, in order to get the complete profile over the whole Si wafer thickness, which is typically three orders of magnitude larger than the laser wavelength, these methods require extensive computational power. Therefore, we use nonlinear paraxial equation (NPE) to understand the light propagation evolution inside silicon (Appendix A). It is given as [44]:

$$\frac{\partial A}{\partial z} = \frac{i}{2k} \nabla_T^2 A + \frac{ikA}{n_0} (\Delta n_{\text{total}} + i\Delta k_{\text{total}}), \quad (2.11)$$

where k is the wavenumber in Si, A is the electric field profile, Δn_{total} is the total change in the real part of the refractive index and Δk_{total} is the total change in the imaginary part of the refractive index. Δn_{total} can be decomposed into three parts:

$$\Delta n_{\text{total}} = \Delta n_{\text{Kerr}} + \Delta n_{\text{FCI}} + \Delta n_{\text{Thermal}}, \quad (2.12)$$

where

1. Δn_{Kerr} represents the refractive index change due to Kerr response of Si and given as $\Delta n_{\text{Kerr}} = n_2 I$, where n_2 is the Kerr coefficient. For silicon, at 1.5 μm , Kerr coefficient is $n_2 = 5 \times 10^{-14} \text{ cm}^2/\text{W}$ [45].
2. Δn_{FCI} is the index change due to the free carrier absorption. The numerical value can be calculated using $\Delta n_{\text{FCI}} = -[8.8 \times 10^{-22} N + 8.5 \times 10^{-18} N^{0.8}]$ as explained in section 2.2.
3. $\Delta n_{\text{Thermal}}$ is the thermally induced refractive index change. As the temperature changes, the refractive index of Si changes according to the relation, $\Delta n_{\text{Thermal}} = 1.86 \times 10^{-4} \Delta T$ [46, 47].

In the imaginary part of the refractive index of silicon, the total change is expressed with two terms:

$$\Delta k_{\text{total}} = \Delta k_{\text{TPA}} + \Delta k_{\text{FCA}}, \quad (2.13)$$

where the terms are:

1. Δk_{TPA} is the two-photon absorption loss and it is represented as $\Delta k_{\text{TPA}} = \frac{\alpha_{\text{TPA}} \lambda_0}{4\pi} = \frac{\beta I \lambda_0}{4\pi}$. Here, α_{TPA} ($=\beta I$) is the attenuation coefficient (cm^{-1}).

2. Δk_{FCA} : Free-carrier absorption coefficient increases with the free carrier density, as can be seen in $\Delta\alpha_{\text{FCA}} = \Delta\alpha_{\text{h}} + \Delta\alpha_{\text{e}} = 0.51 \times 10^{-20} \lambda^2 TN + 1.01 \times 10^{-20} \lambda^2 TN$ (Eq. 2.9). Δk_{FCA} can be calculated using the equation, $\Delta k_{\text{FCA}} = \alpha_{\text{FCA}} \lambda_0 / 4\pi$.

2.4 Light propagation under nonlinear feedback conditions

The major diffractive effects in in-chip structure formation are the thermal lensing due to $\Delta n_{\text{thermal}}$ and FCI diffraction due to Δn_{FCI} . At low intensities, a single laser beam can not generate subsurface modifications, since FCI diffraction prevents self-focusing and thermal lensing is not strong enough. However, in the case of two counter-propagating laser beams, a nonlinear coupling can favor the thermal lensing and creates a self-focusing feedback process. Experimentally, this process is initiated when the reflected beam from the Si-air interface couples to the incident beam inside silicon. In that case, beam self-focuses and subsurface modifications are generated. With every pulse, the process restarts at a slightly shifted position, due to the effect of previously modified areas on the next pulse's propagation. As a result, modifications elongate with every pulse, forming high-aspect ratio structures, analogous to the moving-focus model in filamentation [48]. The model we present here gives an intuition into the subsurface modification dynamics with a single laser pulse. Multi-pulse effects will be summarized later with a simple model in section 2.5

2.4.1 Single-pulse model implementation

The method we use to obtain carrier and temperature profile should be able to handle nonlocal feedback and high optical nonlinearities. Therefore, we chose split step Fourier method, which is a common tool to numerically solve nonlinear differential equations [49]. Briefly, the method assumes linear and nonlinear terms

act independently for small step sizes. For each step, the method first solves linear term in the frequency domain and then the nonlinear term in the spatial domain separately [49].

In the simulations, we set the temporal step size to 10 ps, the approximate round trip time of the light in 500 μm thick wafer, since we can consider the temperature and carrier distribution in that time duration quasi-stationary. The conceptual diagram of the pulse propagation is shown in Fig. 2.2.

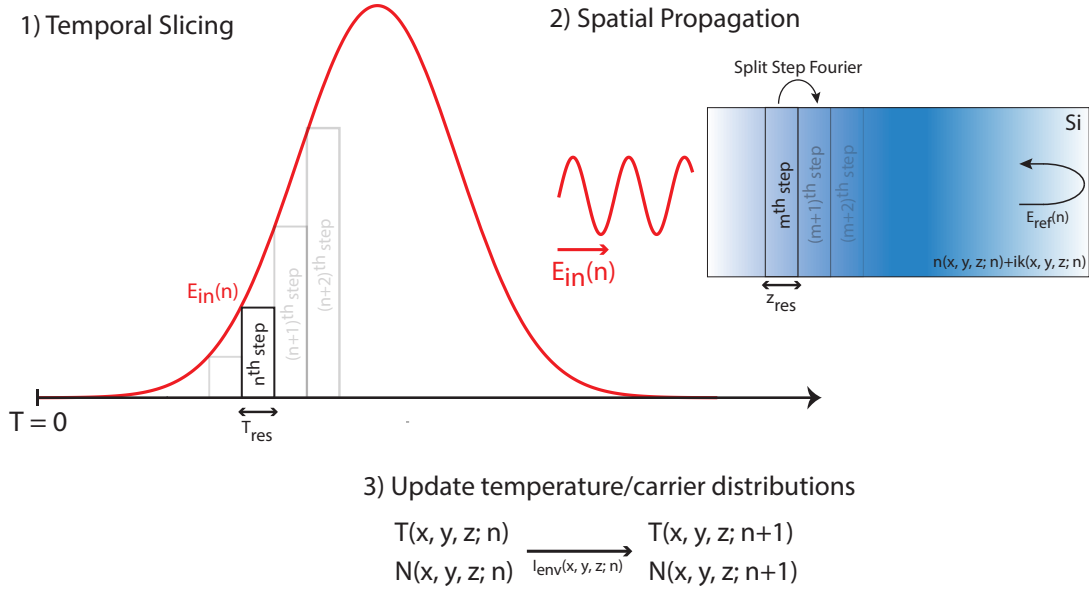


Figure 2.2: For each temporal slice, we calculated the intensity distribution (I_{env}) using the refractive index, temperature and carrier distributions from the previous iteration.

For each temporal slice, we calculate the intensity distribution (I_{env}) with split step Fourier method using the refractive index ($n_{\text{total}}, k_{\text{total}}$), carrier density (N) and lattice temperature obtained in the previous iteration as the input. In the first half of the spatial step size ($\Delta z/2$), field is propagated linearly. Propagation of the nonlinear term is calculated for Δz and the simulation for that specific step is completed by calculating the new field by another linear $\Delta z/2$. In total, both linear and nonlinear propagation terms are obtained for one spatial step size, Δz . We repeat this procedure for each temporal slice until the total time is equal to pulse duration. It should be noted that an interference pattern is expected

to form, when two counter propagating pulses interact. However, the oscillatory period of the expected pattern is $\lambda_{\text{Si}}/2 = 225 \text{ nm}$, which is much smaller than the critical lengths such as the spot size or the diffusion lengths. Therefore, its effect smears out and we use the intensity envelope (I_{env}) in the simulations:

$$I \propto |E_{\text{forward}} + E_{\text{backward}}|^2 \leq (|E_{\text{forward}}| + |E_{\text{backward}}|)^2 = I_{\text{env}}. \quad (2.14)$$

2.4.2 Single-pulse simulation results

Experimentally, we observed that a weakly focused, low power beam can not generate subsurface modifications without a second, counter-propagating beam, namely a *dressing* beam. To confirm this observation theoretically, we simulated two scenarios. In the first scenario, we simulated a single pulse focusing without the dressing beam. In the second case, we added a counter-propagating beam that enables the nonlinear coupling.

In the experiments, we realized the second case by using a double side polished wafer and focusing the beam beyond the laser exit surface, such that 30 % of the incident beam is reflected from the air-Si interface, forming the counter-propagating beam. Although, the incident beam (dressing beam) has more energy (14 μJ) than the reflected beam (4.2 μJ), its peak intensity is lower since it is focused after the sample and have larger beam diameter at the interaction region.

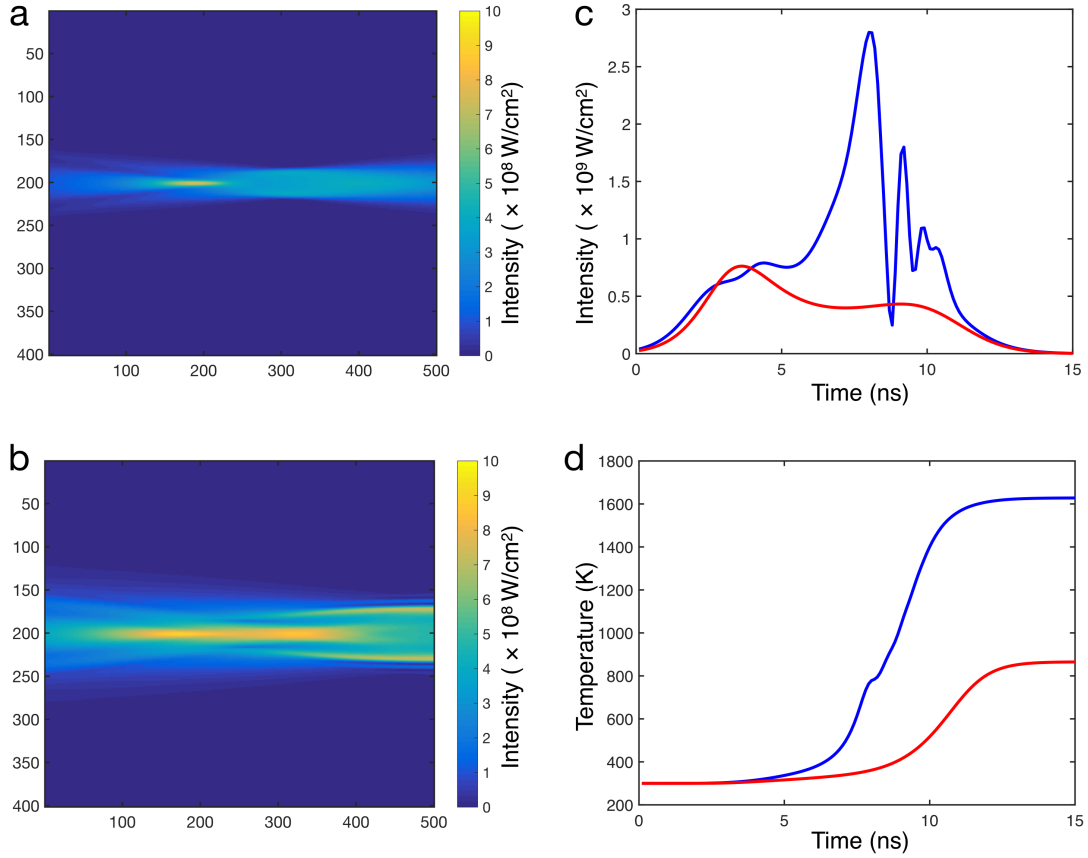


Figure 2.3: (a) Intensity distribution for the undressed beam case. (b) Intensity distribution of the dressed beam case. (c) Intensity evolution in the modification region. The blue curve represents the dressed beam case, and the red curve is for the undressed case. The double peak is because of the delay in the thermal lensing, which becomes effective a few ns after FCI. This indicates the competition between the two effects. (d) Thermal evolution in the modification region. In the dressed beam case (blue curve), temperature reaches the melting temperature of silicon, whereas in the undressed beam case (red curve), maximum temperature is limited to 800 K.

The simulation results are shown in Fig. 2.3. In the undressed beam case, both intensity and temperature increases are limited. In the first few nanoseconds, the beam is diffracted due to FCI (Fig. 2.3(c)). After a few nanoseconds, beam focusing starts due to thermal nonlinearity. The delay between two competing mechanisms is expected, since the main heating mechanism is due to intraband absorption, which requires free carriers generated with two-photon absorption.

In the second case (Fig. 2.3(b)), the only change in the simulation conditions is the addition of a counter-propagating, dressing beam. In this case, due to nonlinear coupling between the beams, intensity reaches the experimentally observed threshold value and temperature increases strongly, after a certain delay. Such dramatic increase in the intensity is associated with self-focusing [50], which results in the morphology change of silicon.

2.5 Description of the theoretical model

We developed a simple model to explain the structure formation and elongation in Si. The model predicts the general characteristics of the modifications, which are experimentally confirmed. The three claims of the model are (i) a feedback mechanism supplied by a counter-propagating beam is necessary for structure formation, (ii) each pulse elongates the structures due to the nonlinear feedback and (iii) the total structure length saturates for high number of pulses.

We follow an approach similar to the mathematical induction method. We start to model the process with the single pulse case, then we first extend it to two-pulse case and finally to any number of pulses. Two equations, nonlinear paraxial equation (NPE) and heat equation, govern the pulse propagation, as explained in detail in section 2.3. Briefly, Δn_{total} term in Eq. 2.11 represents the feedback between two opposing effects originated from thermal nonlinearity and free carrier induced (FCI) refractive index change. These two effects behave as converging lens with a positive focal length, f_{therm} and diverging lens with a negative focal length, f_{FCI} , respectively. The beam self-focuses and collapses, if thermal lensing is stronger than the diffraction induced by FCI. The modification as the result of this first feedback mechanism initiates a second feedback for the elongated structures.

When the next pulse arrives, the modification that was formed shifts the collapsing point of the pulse with a mechanism similar to moving focus model of

self-focusing. We use the lens equation, $\frac{1}{l_2} = \frac{1}{f_t} + \frac{1}{l_1}$ to calculate the focal transition, where l_1 and l_2 are the focal positions of the first and second pulses, and f_t is the shift in the focal length per pulse. Here, we introduce a measure of the competition between the lensing effects, $\eta = \frac{f_{\text{therm}}}{f_{\text{FCI}}}$, and we defined $f_t = \frac{f_{\text{therm}}}{(1+\eta)}$. For subsurface modification to start, $-1 < \eta < 0$ must be satisfied, since by definition $\eta < 0$ and for self-focusing $f_t > 0$, indicating $-1 < \eta$.

When we extend this case to the n^{th} modification, we can calculate l_n using the equation $\frac{1}{l_n} = \frac{n-1}{f_t} + \frac{1}{l_1}$. In that case, the total focal shift, giving the total length of the subsurface modifications, is written as:

$$\delta l_n = \frac{l_1^2(n-1)}{f_t + l_1(n-1)}. \quad (2.15)$$

The free parameters in Eq. 2.15 to calculate the total structure length is f_t and n . This term is a function of f_{therm} and f_{FCI} . Thus, in order to find f_t numerically, we first calculate f_{therm} and f_{FCI} , which requires carrier and temperature profiles in silicon.

After the first pulse, the total carrier density δN_{tot} is written as:

$$\delta N_{\text{tot}} = \delta N_1 + \delta N_2 + \delta N_3, \quad (2.16)$$

where δN_i represents the carrier density generated by forward propagating beam ($i = 1$), backward propagating beam ($i = 2$) and their coupling ($i = 3$). In the case of incident beam is Gaussian, carrier densities are given as:

$$\delta N_i(z, r) \approx \frac{\beta I_i^2(z) \delta t}{2E} e^{-\frac{4r^2}{w_i^2(z)}}, \quad (2.17)$$

where β is two-photon-absorption coefficient, I is the intensity, δt is pulse width, r is the radial distance, E is the photon energy and w is the beam radius. Therefore, the total refractive index change due to FCI is:

$$\delta n_{\text{FCI}}(z, r) \approx -A \delta N_{\text{tot}}(z, r) = - \sum_{i=1}^3 \frac{A \beta I_i^2(z) \delta t}{2E} e^{-\frac{4r^2}{w_i^2(z)}}, \quad (2.18)$$

where $A = 8.8 \times 10^{-22} \text{ cm}^3$ is constant [51].

Similarly, assuming the temperature and the intensity have the same spatial profile, we can write the total temperature change as:

$$\delta T_i(z, r) \approx \frac{\beta I_i^2(z) \delta t}{\rho c} e^{\frac{-4r^2}{w_i^2(z)}}, \quad (2.19)$$

where ρ is density and c is specific heat capacity. The refractive index change due to the temperature change is:

$$\delta n_{\text{therm}}(z, r) \approx \sum_{i=1}^3 \frac{\beta I_i^2(z) \delta t}{\rho c} \frac{dn}{dT} e^{\frac{-4r^2}{w_i^2(z)}}. \quad (2.20)$$

Both Eq. 2.18 and Eq. 2.20 can be further simplified by using the paraxial ray approximation and expand the terms around the optical axis. The equation set becomes:

$$\delta n_{\text{FCI}}(z, r) \approx - \sum_{i=1}^3 g_i(z) \left(1 - \frac{4r^2}{w_i(z)^2} \right) \quad (2.21)$$

$$\delta n_{\text{therm}}(z, r) \approx \sum_{i=1}^3 h_i(z) \left(1 - \frac{4r^2}{w_i(z)^2} \right), \quad (2.22)$$

where $g_i(z) = A \frac{\beta I_i^2(z) \delta t}{2E}$ and $h_i(z) = \frac{\beta I_i^2(z) \delta t}{\rho c} \frac{dn}{dT}$ are $\delta n_{\text{FCI},i}(z, 0)$ and $\delta n_{\text{therm},i}(z, 0)$, respectively. When we average these terms over the propagation direction, refractive index profiles reach their general form:

$$\delta \bar{n}(r) = \delta \bar{n}_0 \left(1 - \frac{4r^2}{\bar{w}^2} \right), \quad (2.23)$$

where \bar{n} , \bar{w} indicates average values.

We can use matrix optics formalism to characterize the ray paths of the paraxial beam propagating in a medium, where refractive index is r-dependent. The

paraxial ray equation for this case can be written as:

$$\frac{\partial n}{\partial r} = n(r) \frac{d^2 r}{dz^2}. \quad (2.24)$$

By plugging Eq. 2.23 into Eq. 2.24, we obtain the propagation equation as:

$$\frac{d^2 r}{dz^2} + z_0^2 r = 0, \quad (2.25)$$

where $z_0^2 = \frac{8}{\bar{w}^2}$. Transmission matrix of the medium obtained from this equation is [52]:

$$T = \begin{bmatrix} \cos(z z_0) & \frac{1}{z_0} \sin(z z_0) \\ -z_0 \sin(z z_0) & \cos(z z_0) \end{bmatrix} \quad (2.26)$$

which is the equivalent of the transmission matrix of a lens with a focal length, f [52, 53]:

$$f = \frac{1}{\delta \bar{n}_0 z_0}. \quad (2.27)$$

Here, we assume refractive index changes in forward and backward directions are the same and represent them at $r = 0$ as $\bar{g}_3 = \alpha \bar{g}_1 = \alpha \bar{g}_2$ and $\bar{h}_3 = \gamma \bar{h}_1 = \gamma \bar{h}_2$, where α and γ are strength of coupling terms. Thus, we rewrite f_{FCI} and f_{therm} as:

$$f_{FCI} \approx -\frac{1}{\delta \bar{n}_{0,FCI} z_0 (2 + \alpha)} = \frac{2E}{A \beta I^2 \delta t z_0 (2 + \alpha)}, \quad (2.28)$$

$$f_{therm} \approx \frac{1}{\delta \bar{n}_{0,therm} z_0 (2 + \gamma)} = \frac{\rho c}{\beta I^2 \delta t \frac{dn}{dT} z_0 (2 + \gamma)}. \quad (2.29)$$

One of the claims of the model is that a feedback mechanism supplied by a counter-propagating beam is necessary for structure formation. In order to see this, we set the coupling terms to zero, $\alpha = \gamma = 0$, in Eq. 2.28 and Eq. 2.29 and use the experimental parameters to obtain the rest of relevant terms. For the parameter set of $\lambda = 1.55 \mu\text{m}$, $\bar{w} = 3 \mu\text{m}$, $\delta t = 5 \text{ ns}$, and $E_p = 10 \mu\text{J}$, we calculated refractive index changes and the focal lengths as $\delta \bar{n}_{0,FCI} = -8.3 \times 10^{-5}$ and $\delta \bar{n}_{0,therm} = 1.4 \times 10^{-6}$, and $f_{therm} = 7.4 \times 10^6 \mu\text{m}$ and $f_{FCI} = -2.5 \times 10^5 \mu\text{m}$.

From these results, $\eta = \frac{f_{\text{therm}}}{f_{\text{FCI}}} \approx -30$ is found, which indicates a diverging lens effect and doesn't satisfy the structure formation condition of $-1 < \eta < 0$.

This claim can be tested experimentally by eliminating the back surface reflection, which provides the counter-propagating beam. We coated half of a surface of the wafer with an anti-reflection layer such that the focused beam does not reflect back into the Si sample (Fig. 2.4(a)). We scanned the laser through the interface between double-side polished and the coated regions. As predicted, the subsurface structures did not form in the coated region due to the absence of the feedback (Fig. 2.4(b)).

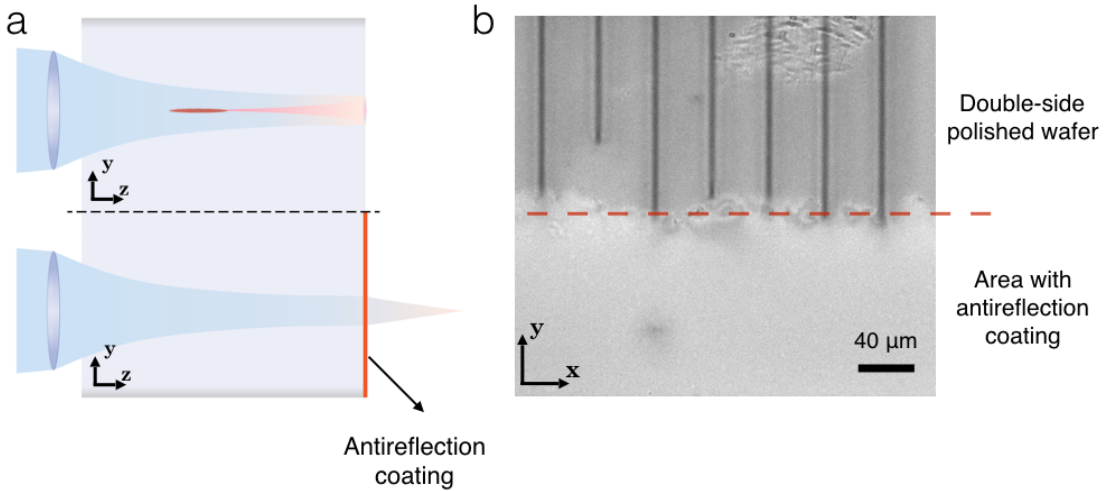


Figure 2.4: (a) Schematic showing the pulse propagation for the cases with and without counter-propagating beam. We coated 200 nm thick Si_3N_4 to prevent reflection so that the focused beam can pass through the back surface without any reflection. (b) IR transmission microscope images of the subsurface structures, which are formed only in the double-side polished region.

The model also suggests that each pulse elongates the structures and elongation stops before the surface damage. We use nonzero α and γ in the model together with an η between -1 and 0. We generated subsurface modifications with different number of pulses and measured the structure lengths. We compared the experimental data with the structure length predicted by the model (Fig. 2.5). We used f_t as a fitting parameter and set $f_t = 26$ mm. From Eq. 2.28 and Eq. 2.29 we can estimate α and γ as:

$$\gamma = \frac{f_{\text{therm}}^0}{f_t} - \alpha \frac{f_{\text{therm}}^0}{f_{\text{FCI}}^0}, \quad (2.30)$$

where f_{FCI}^0 and f_{therm}^0 FCI induced and thermal focal lengths in the case of no feedback.

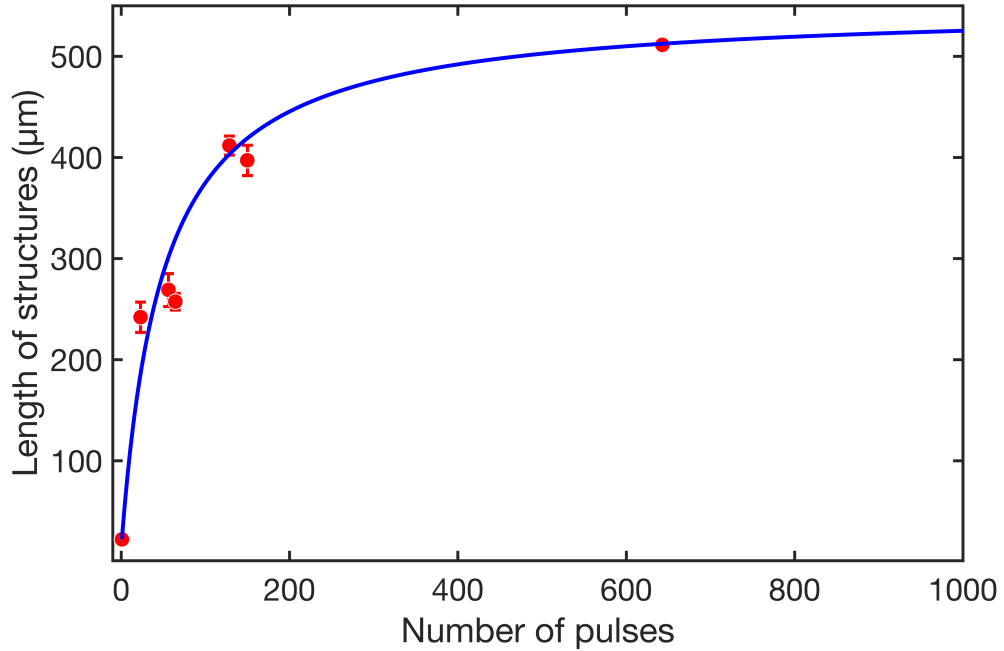


Figure 2.5: Measured structure lengths (red circles) are good agreement with the model's prediction (blue line).

In summary, we developed a simple model that explains the experimental observations such as the effect of the interaction between two counter-propagating beams for in-chip structure formation and the elongation of the structures with the increased number of pulses.

Chapter 3

In-chip computer generated holograms (CGH)

Building optical devices based on spatial phase control is possible by using the subsurface modifications inside silicon. We constructed the first diffractive optical elements buried in Si, including gratings, Fresnel zone plates and holographic components [19]. Due to the wide transparency window of silicon from $1.2 \mu\text{m}$ to $7 \mu\text{m}$, extending the diffractive optics capability into Si may have applications in areas such as wavefront correction and spectroscopy for near and mid-IR [54, 55].

Holograms are diffractive optical elements that modulate the phase and/or the amplitude of the light at the image plane [54]. Particularly, computer generated holograms (CGHs) found use in various fields including optical manipulation [56], imaging and microscopy [57]. Since the holographic medium affects the overall quality of the holograms, there has been extensive studies on recording media and different materials have been tested for this purpose such as liquid crystals [58], photorefractive materials [59] and metamaterials [60]. However, these mediums have certain limitations. For example, in order to have high efficiencies with metasurface holograms, they have to be illuminated with circularly polarized light. Metamaterial holograms are not CMOS compatible and they have high losses. In-chip Si holograms overcome these limitations and can be integrated to

silicon photonics.

It is possible to fabricate holograms on surfaces or in the bulk of materials. Previously, volume holograms embedded in the materials have been reported in glasses [61, 62] and photorefractive polymers [63, 64]. We demonstrated that the bulk of silicon can be used to create similar volume holograms thanks to the phase control provided by the method we developed. Phase holograms result in better image quality with the same number of pixels compared to the amplitude holograms. Moreover, buried holograms are expected to endure longer than the surface holograms. We designed the algorithm for CGHs inside silicon and implemented both Fourier- and Fresnel-type CGHs for 2D wavefront structuring and 3D image formation, respectively.

3.1 Generation of CGHs with a modified iterative Fourier algorithm

Fourier holograms and Fresnel holograms diffractions happen in far field and near field, respectively. Compared to Fresnel holograms, Fourier holograms can be generated with lower computational power and creates higher quality 2D images with the same pixel number. However, Fresnel holograms can generate better depth perception in 3D. Practically, Fourier holograms can be projected to the near field with a Fourier lens, which transforms Fresnel diffraction equation to Fraunhofer regime [65]. Therefore, we selected Fresnel CGHs for 3D image generation and Fourier CGHs for wavefront structuring in 2D.

There are several algorithms for CGH design such as Lee algorithms, Detour Phase algorithms and Iterative Fourier Transform Algorithms (IFTA) [54, 65]. The main approach in these algorithms is to modulate the amplitude or the phase to reconstruct an image. We used a modified version of IFTA to design the holographic mask to be processed inside Si. One of the modifications we implemented was to change the spectral condition of adaptive-additive IFTA [66].

Additionally, to improve the reconstructed image quality, in the iterative generation process the noise space was expanded. Through these changes, algorithm can produce both binary and grayscale images with binary phase holograms (binary kinoforms).

Generally, binary holograms perform poorly compared to grayscale holograms [67]. In our algorithm, we solved this problem with the expanded noise space in the iterative process. By doing so, we reduced speckles at the target plane and improved the image quality. The comparison of several versions of CGH algorithm is shown in Fig. 3.1. Binary kinoform generated without IFTA created the image with the lowest image quality (Fig. 3.1(c)). Quality was improved when we simulate the same image with the binary kinoform generated with the binarized adaptive-additive IFTA (Fig. 3.1(d)). Speckles were reduced and the quality of the image was further improved when we used the modified adaptive-additive IFTA, as expected (Fig. 3.1(e)). It performs similarly to a 256-level grayscale hologram (Fig. 3.1(b)).



Figure 3.1: Quality comparison of images reconstructed with different algorithms. (a) The original image. The rest is the simulation result of the constructed image of (b) grayscale kinoform (256 Levels) generated by adaptive-additive IFTA. (c) binary kinoform generated without IFTA. (d) binary kinoform generated with binarized adaptive-additive IFTA. (e) binary kinoform generated with binarized adaptive-additive IFTA after increasing noise space.

We summarized the general flow of the algorithm in Fig. 3.2. At the initial steps of the method, we implemented the same procedure as in the adaptive-additive IFTA, where random phase is added to the target image (Steps 1, 2). At the hologram plane, amplitude of the complex field is eliminated (Step 5) and adding random noise compensates for this loss. Starting from the step 3, our

algorithm starts to deviate from the adaptive-additive IFTA. Customarily, some constraints are imposed on the amplitude distribution at hologram and image planes in kinoforms and phase can be distributed freely in both planes. Therefore, phase spaces can be considered as free parameters that can be exploited. In order to take advantage of this space on the whole plane, we applied a DC bias to the amplitude distribution so that the phase is not weighted by zero amplitude at any position (Step 3). DC bias may decrease the image contrast and hologram efficiency. Thus, the value should be chosen accordingly. In the next step, the target image was framed with random amplitude and phase to increase the noise space (Step 4). An appropriate frame size does not increase the experimental noise levels. At the iterative block of the algorithm (Step 5-7), first, the phase distribution is binarized and the amplitude distribution is flattened (Step 5). In step 6, the image is reconstructed by taking the inverse Fourier transform of the generated hologram. If the mean square error between the source and the simulated image is within the designed range, the loop ends. Otherwise, amplitude distribution of the simulated image is modified using the adaptive-additive equation [68] and iteration continues.

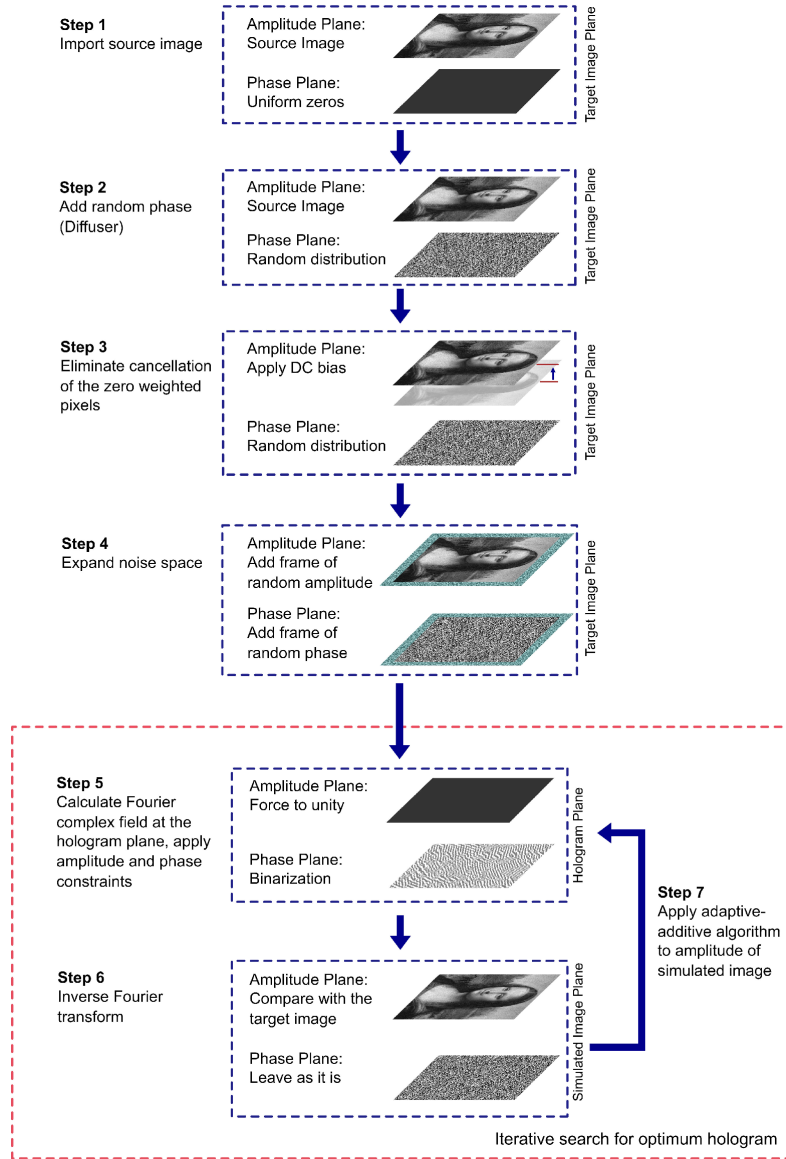


Figure 3.2: Flow of the modified adaptive-additive iterative Fourier algorithm. The final hologram is implemented inside Si.

The modifications in Step 3 and 4 of IFTA increased the degree of freedom of the algorithm and improved the quality of the binary phase holograms to the level of grayscale holograms (Fig. 3.1). The binary Fourier holograms we designed and implemented in silicon enabled us to project both binary and grayscale images.

We improved this algorithm for high quality 3D image projection without directly solving Fresnel diffraction equation. To this end, we sliced a 3D image

and generated each slice as binary Fourier hologram. Using proper binarization and normalization steps, we combined this stack of Fourier holograms into a single hologram. We superimposed Fresnel zone plates with different focal points on the final hologram to form each image on a different plane. Therefore, we had the computation tool for generating Fourier phase holograms (binary and grayscale), together with the binary Fresnel phase holograms.

3.2 Implementation of the holograms

For the implementation of the first type of Fourier hologram, we chose a binary image containing high spatial frequencies. For the second type, to demonstrate the wavestructuring capability, we selected a grayscale image (Da Vinci's Mona Lisa). We used the experimental setup illustrated in Fig. 3.3 for the image reconstruction. Briefly, on the optical axis, we have a Fourier lens before the hologram to form the image in the near field and a diverging lens after the hologram to expand the image for better imaging. We placed a spatial filter to keep only the first order and eliminate the rest. Due to the limitations in the imaging camera (Canon, SX710 HS), we used 1030 nm laser as the light source for convenience. However, as will be shown in chapter 4, the modifications can be used at other near-infrared wavelengths.

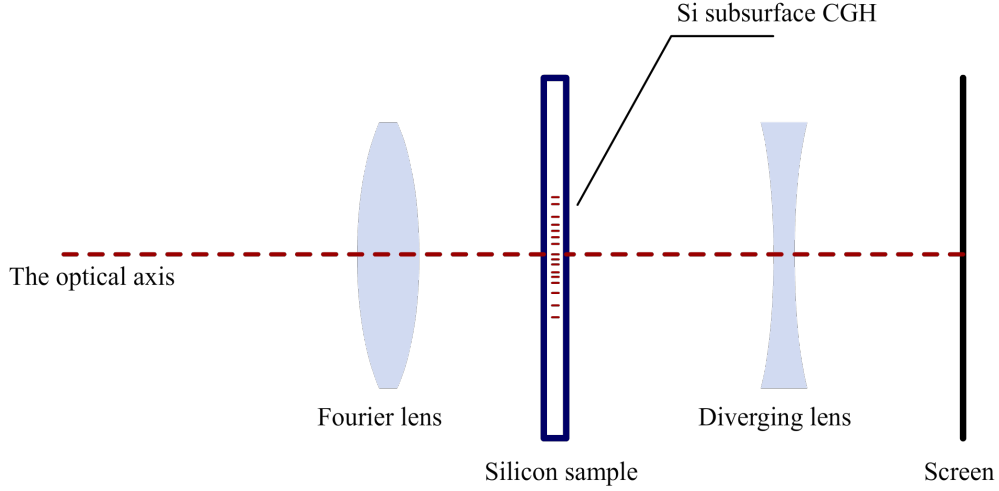


Figure 3.3: Optical reconstruction setup for the Fourier holograms embedded inside silicon.

Binary image and grayscale image reconstructions are shown in Fig. 3.4 and Fig. 3.5, respectively. Simulations and experiments are in good agreement. Reconstructed images have more speckle than the simulation results, mostly due to the parasitic interference on the CMOS sensors, which is a practical limitation which can be overcome. Binary image has a size of 600×600 pixels, whereas grayscale image size is 800×600 pixels. In both cases, pixel size is $10 \mu\text{m}$ and since it is approximately one order of magnitude larger than the wavelength, we can apply scalar diffraction theory. Potentially, pixel size can be reduced to the modification resolution ($\sim 2 \mu\text{m}$), which allows the metasurface hologram fabrication with in-chip structures for the wavelength range of $5\text{-}7 \mu\text{m}$.

We also implemented a binary Fresnel hologram, designed with the algorithm explained in section 3.1. We selected the same hologram parameters as for the Fourier holograms, a pixel size of $10 \mu\text{m}$ and 800×600 pixels hologram size. For the simplicity, we selected a target image of rotating rectangles on the optical axis, forming a twisted rectangular prism. The whole image was composed of four layers, each of them is the rotated version of the previous layer by $\pi/2$ (Fig. 3.6).

We evaluated the hologram efficiency by taking the power ratio between the

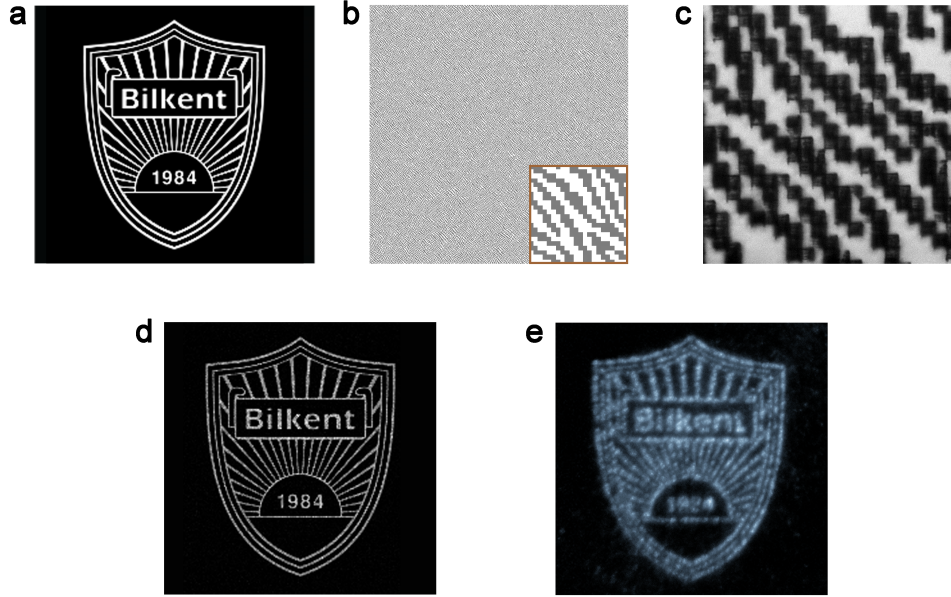


Figure 3.4: Implementation of binary hologram and the experimental reconstruction. (a) The original image with high spatial frequency components. (b) Full hologram designed with the modified algorithm. Inset shows the zoomed in version. (c) IR microscope image of a portion of the embedded hologram in Si. (d) The simulation of the reconstructed image. (e) Experimentally reconstructed image.

first order and the zeroth order [69]. For the measurements, we fabricated an in-chip phase grating with 50 lines/mm groove frequency using $10 \mu\text{m} \times 10 \mu\text{m}$ pixels over an area of $2 \text{ mm} \times 2 \text{ mm}$. For this diffractive element, efficiency can be calculated as [69]:

$$R = F(4/\pi^2)\sin(\Delta\phi/2)^2/(1 - F + F\cos(\Delta\phi/2))^2 \quad (3.1)$$

where F is the filling factor and $\Delta\phi$ is the phase modulation depth. For $\lambda = 1.03 \mu\text{m}$, we measured the power ratio as 150 %. This corresponds to $\Delta\phi = 0.69\pi \pm 0.04\pi$, which is in good agreement with the interferometric measurement of $\Delta\phi = 0.69\pi \pm 0.01\pi$.

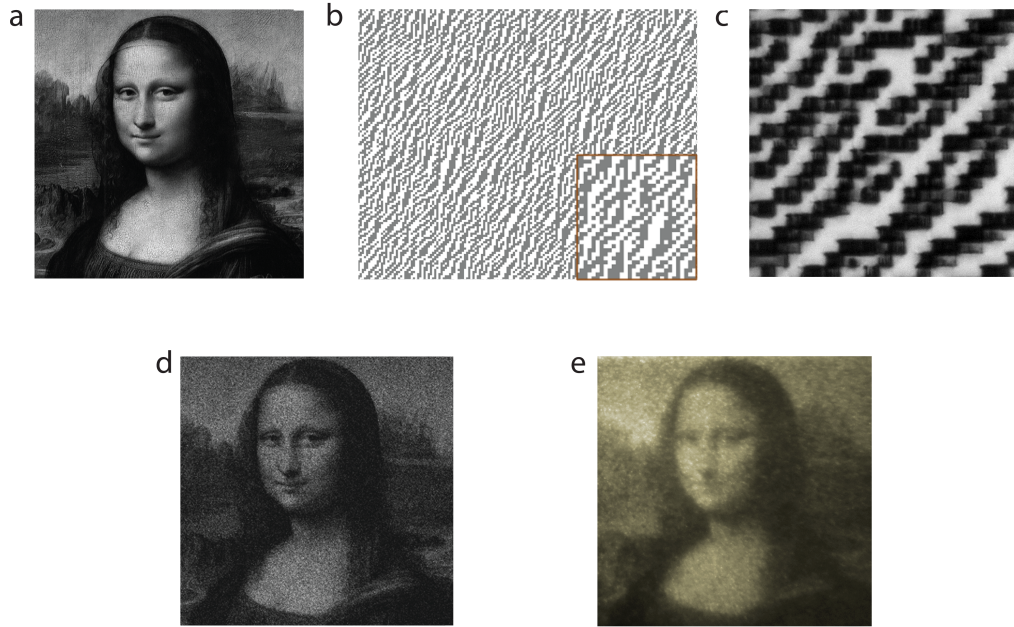


Figure 3.5: Implementation of *Mona Lisa* hologram and the experimental reconstruction. (a) The original grayscale image. (b) Full hologram designed with the modified algorithm. Inset shows the zoomed in version. (c) IR microscope image of a portion of the embedded hologram in Si. (d) The simulation of the reconstructed image. (e) Experimentally reconstructed image.

It should be noted that in-chip Si holograms can operate with both circular and linear polarizations. This simplifies the operational requirements, which potentially makes the in-chip holograms useful for communications and optical information processing [65]. Additionally, combining the in-chip holograms with surface holograms may pave the way towards generating more complex images by modulating both phase and amplitude separately.

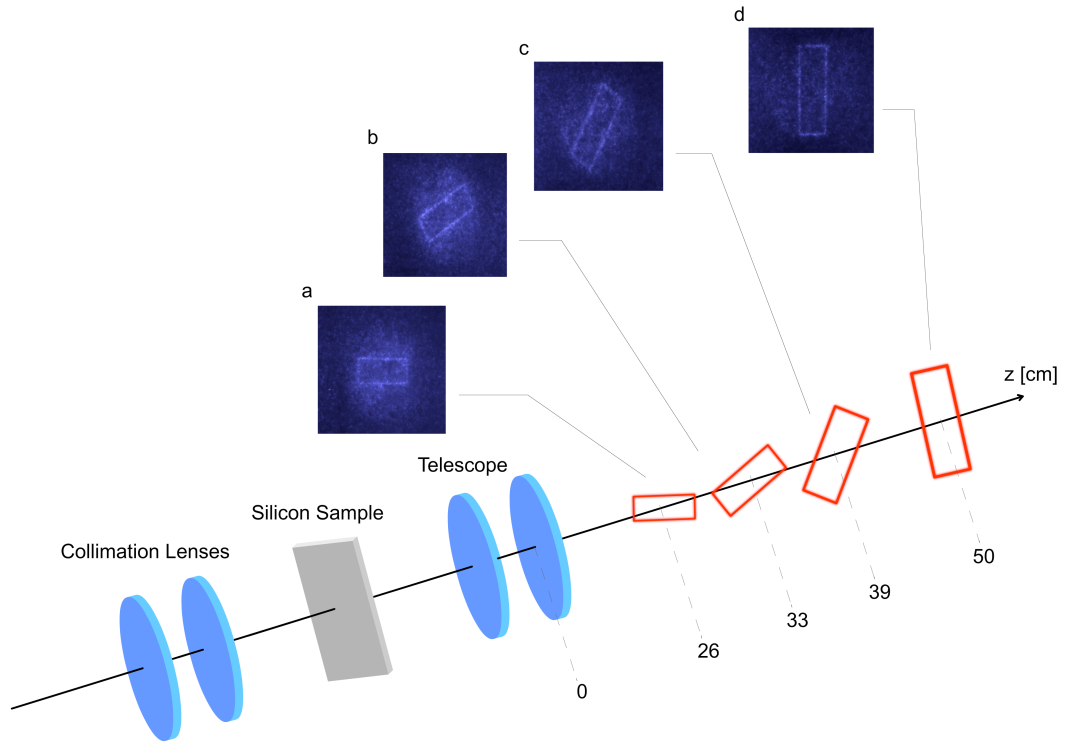


Figure 3.6: Illustration of the optical setup for Fresnel image reconstruction. We expanded the beam to from a larger image for capturing. Each slice of the total image is separated from each other by approximately 7 cm.

3.3 Development of a new algorithm for dynamic hologram generation

Fresnel holograms are commonly used for projecting 3D images. However, the methods to generate these holograms have certain limitations. The first algorithm for Fresnel CGHs works only for two planes [70]. Alternative approaches require heavy computations and specific holographic medium [71]. Using look-up tables have been proposed, but the method is restricted to low-resolution image reconstruction [72, 73]. Although, back-to-back projection of large number of images have been shown recently, the images were created sequentially, not simultaneously [74].

I contributed to the efforts to overcome these limitations of binary Fresnel

holograms. In the study led by Dr. Ghaith Makey from Bilkent Univeristy, adaptive-additive IFTA was modified and we demonstrated four-layer image projection using in-chip holograms (Fig. 3.6). Briefly, we generated each layer of the 3D image as Fourier holograms and combined them with Fresnel zone plates into a single hologram. While generating the Fourier holograms, we exploited the phase space to increase the quality of the target image (Section 3.1). Here, we further extended the algorithm for greyscale Fresnel holograms and improved the number of on-axis projection layers from 3-4 to 1000 [75].

We were able to enhance 3D depth by engineering the noise space of the images such that the crosstalk between the consecutive images were eliminated. We can map an image to an N -dimensional vector, where N represents the number of pixels ($N \approx 10^6$). Random vectors are approximately perpendicular when $N \rightarrow \infty$ (Fig. 3.7(a)). This result is due to the central limit theorem and the law of large numbers. In image reconstruction, this property corresponds to elimination of coherent traces of the images on other target planes (Fig. 3.7(b)).

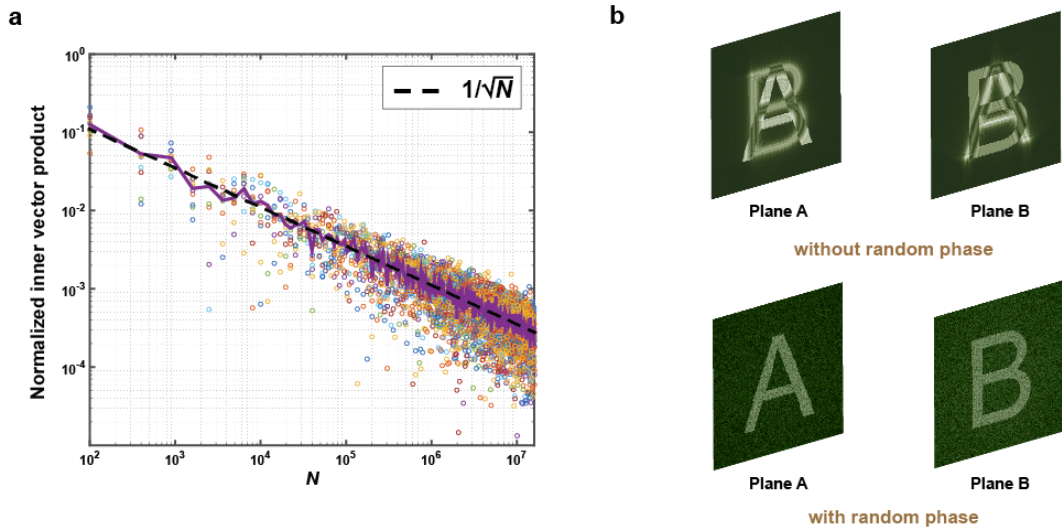


Figure 3.7: (a) Normalized inner product of two checkerboard patterns as a function of pixel number N . Both images have random phase between $0-2\pi$. As N increases, their inner product approximates to zero, indicating orthogonality. (b) Comparison of two-plane projection simulations generated with and without random phase. Adding random phase eliminated the crosstalk between the images.

For the experiments, we used a 800×600 pixels, reflective liquid crystal on

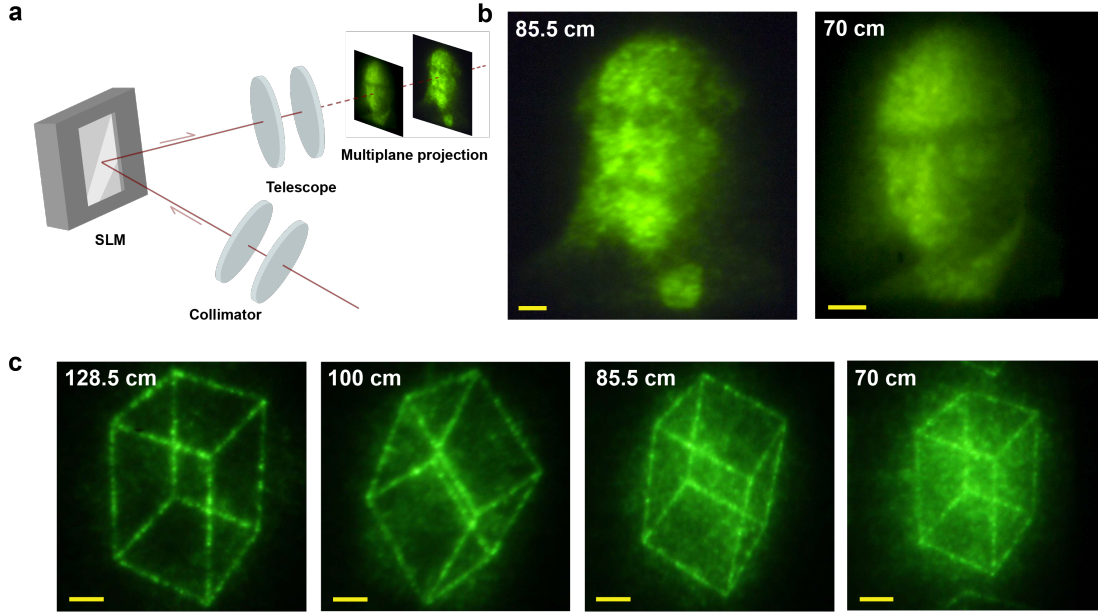


Figure 3.8: (a) Illustration of the optical setup used in image reconstruction. (b) Simultaneous projection of high-resolution grayscale images. Target planes are separated by 15 cm. (c) Recorded image of a four-layer projection of a rotating cube.

silicon spatial light modulator (LcoS-SLM) as the holographic medium. We collimated and polarized the incident laser beam ($\lambda = 1.03 \mu\text{m}$) for efficient modulation with the Fresnel CGH. Then we expanded the reflected beam with a telescope (magnification of $\times 3$) to eliminate the zero-order diffraction (Fig. 4.4(a)). We recorded the reconstructed images with a digital camera. Experimentally, we demonstrated high resolution grayscale images in two planes (Fig. 4.4(b)) and four-plane reconstruction of a rotating cube (Fig. 4.4(c)), both with a single Fresnel hologram.

In summary, we first demonstrated the first buried holograms inside silicon and later expanded the algorithms to be applicable universally on other holographic media. The algorithm is a modified version of adaptive-additive IFTA, to increase the quality of the Fourier holograms and used this method to generate both binary and grayscale images. We further created binary Fresnel holograms and implement them inside silicon using 3D-NLL method and projected four-layer on-axis

images. Finally, we developed a new algorithm for grayscale Fresnel holograms that enhances the number of projection levels for two orders of magnitude.

Chapter 4

Laser-written waveguides deep inside silicon

In the last two decades, laser-written waveguides have been widely studied inside a large set of transparent materials, including glasses, polymers and crystalline dielectrics [10, 13, 76, 77]. Using the material's bulk for devices with laser unlocks a third dimension for fabrication and provides an architectural advantage. Such a capability in light propagation control is vital for integrated optics and potentially useful for electronic-photonic integration [17, 78]. Photonic devices in various configurations, such as modulators, resonators, couplers and optical interconnects demonstrate the significant potential of laser-written devices in this direction [15, 16, 79–81]. Laser-written devices have also been exploited for other applications; for instance, in signal processing, in imaging and as well as in quantum photonics experiments [82–86].

Performance of photonic devices depends on the optical guiding properties of the laser-written modifications. Therefore, studies have been focused on decreasing the optical losses. The lowest loss coefficients are in the range of 0.3- 1.0 dB/cm for silica glasses [87, 88], 0.3- 3.0 dB/cm for PMMA polymers [89, 90] and 0.5- 3.5 dB/cm for crystals [91–94]. For silicon, laser-written waveguides have been realized for both nanosecond and ultrafast lasers [31, 95, 96]. However, they

suffer from scattering losses as the beam propagates and this problem results in high loss coefficients [31,96].

In this chapter, we explain two types of in-chip waveguides in detail; depressed-cladding waveguide where laser-written modifications form the cladding and type-I waveguide where laser-induced positive refractive index change is used as core. Depressed-cladding waveguide is fabricated with nanosecond pulses and refractive index depression of 3×10^{-4} induced by the laser writing can be used as the cladding of longitudinally written, tubular-shaped buried waveguides in silicon. We characterized the optical properties of the waveguides using near- and far-field imaging. From two measurements, from the output power and from the scattering experiments, we estimated the waveguide loss at $1.3 \mu\text{m}$ as 1.4 dB/cm and 2.1 dB/cm, respectively [32]. Type-I waveguide is written with femtosecond pulses and we calculated the laser-induced refractive index increase as 3.5×10^{-4} at $1.55 \mu\text{m}$ from far-field imaging [95]. Although, we did not fully characterize the loss coefficients of the waveguides, we estimated that it is smaller than 6 dB/cm.

4.1 Laser-written depressed-cladding waveguides inside bulk silicon

In most crystalline materials, laser-induced disruptions in the lattice results in a negative refractive index change in the effected zone. In this case, modifications can be placed in tubular shape such that they enclose unmodified region and form the cladding of the waveguide. Therefore, this type of waveguide fabrication requires a more complex writing scheme [76]. However, this architecture has an advantage in device design since the beam propagates in undisturbed, uniform material with known optical properties [79].

4.1.1 Waveguide fabrication

We used a home-built master-oscillator-power amplifier (MOPA) system that can generate 5 ns pulses with 30 μJ pulse energy at a repetition rate of 150 kHz and 1.55 μm center wavelength. The collimated beam from the laser output is directed to half-wave plate, polarizing beam splitter and half-wave plate sequence to control the beam polarization and the optical power. Sample is positioned on a processing station which is composed of a 3-axis, programmable translational stage (Aerotech, ANT130-XY, ANT95-L-Z) and an imaging system perpendicular to laser propagation direction (Fig. 4.1(a)). Since the structures are entirely embedded into the silicon sample, to monitor the position and the overall quality of the modifications, it is necessary to use infrared transmission microscope as the imaging system. We directed the reflected laser beam from the sample surface to a separate infrared camera with a help of a thin glass for the precise alignment of the sample. Details of the processing setup together with MOPA system are reported previously [19].

To create the subsurface structures, we focused a linearly-polarized beam by using an aspheric lens ($\text{NA} = 0.25$, $f = 1.1$ cm) into 1-mm thick, Si wafer (p-type, $< 100 >$, $1 \Omega\cdot\text{cm}$). We calculated the pulse energy approximately 12.6 μJ inside the sample, after accounting for the losses in the beam path, such as Fresnel reflection from the silicon-air interface. In order to have structures longer than 1-mm, we polished side surface of the wafer and used this side as the laser entrance surface. Using these parameters, we formed in-chip structures with 100 μm -long and 4 μm -wide without changing the focal position in the sample. We were able to extend the structure length by using longitudinal writing arrangement, by scanning the sample along the optical axis. With this method, both index change and the structure width remain the same for 3 mm, minimally affected by spherical aberration due to relatively loose focusing of low numerical aperture lens. A 500- μm -long section of a typical elongated modification is shown in Fig. 4.1(b).

Sign and the magnitude of the refractive index change of the laser-induced

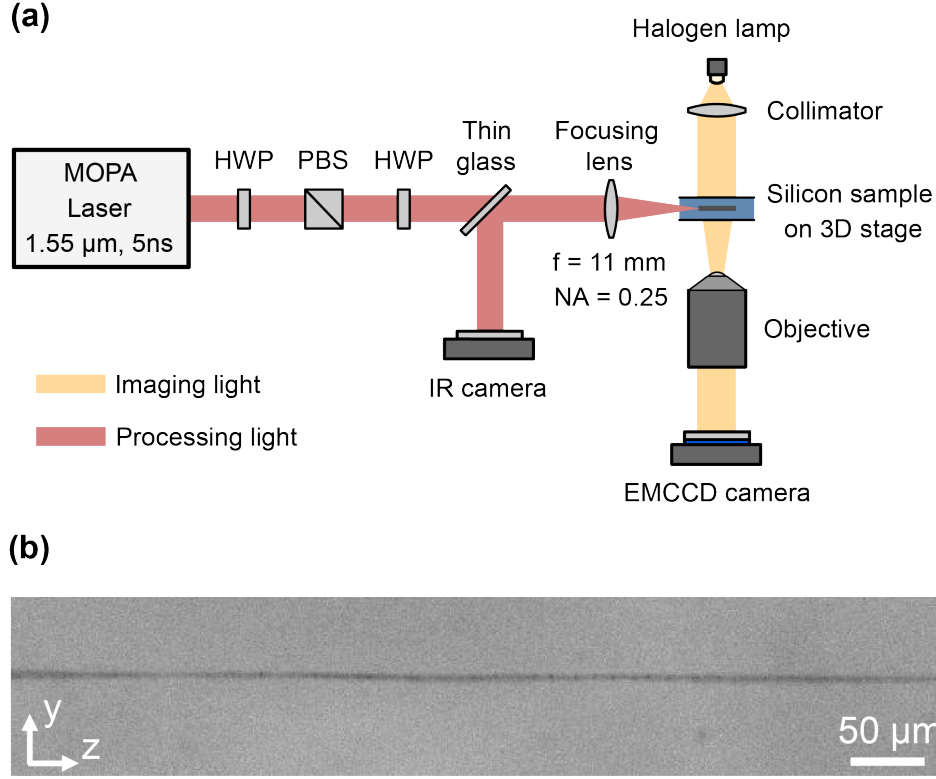


Figure 4.1: (a) Schematic of the experimental setup for waveguide fabrication and *in-situ* imaging of the writing process. A nanosecond laser operating at 1.55 μm is used for device fabrication and IR transmission microscope is used for characterization. MOPA: Master-Oscillator Power Amplifier; HWP: half-wave plate; PBS: polarizing beam splitter. (b) IR transmission microscope image of a single-line modification. Laser entrance surface is the polished side surface (x - y plane) and laser propagation direction is z -axis. To elongate the structures, scanning direction is set along the laser propagation direction.

modifications are critical information to design the physical properties of the waveguides. To get this information, we modified a volume of 4 mm \times 4 mm \times 0.3 mm silicon entirely buried in the wafer and used this sample for an interferometric measurement. First, we obtained an interference pattern as a reference by placing two identical unmodified silicon samples into interferometer's paths. Following that we placed the modified sample into one arm and obtained a second pattern, which is a shifted version of the reference pattern. The amount of the shift is related to the refractive index difference between the modified and unmodified silicon. The refractive index change can be calculated from the measured phase shift, using $\Delta\phi = 2\pi\Delta nL/\lambda$. In the formula, $\Delta\phi$ is the measured phase shift,

Δn is the refractive index difference, L is the structure length in the optical axis, and λ is the wavelength in air. We measured $\Delta\phi$ at $\lambda = 1.30 \mu\text{m}$ as 0.14π . We used a home-built Raman laser as light source that can generate picosecond pulses in the wavelength range of $1.06 \mu\text{m}$ and $1.35 \mu\text{m}$ [97] and calculated the magnitude of Δn as 3×10^{-4} . We produced in-chip holograms with a similar refractive index change [19], indicating modifications can be used for waveguide fabrication. Using IR transmission microscopy, we also found that nanosecond pulses induce a negative refractive index change inside Si.

Next, we fabricated buried waveguides using in-chip modifications as building blocks (Fig. 4.2). With $\Delta n < 0$ modifications, various waveguide configurations are possible. Two most common types are parallel track and depressed cladding configurations [76]. In our case, the latter architecture is more favorable since it can provide symmetric output profile by circularly enclosing the unmodified, higher-index waveguide core with depressed-index modifications (Fig. 4.2(a)). We also chose longitudinal writing geometry over the transverse writing to eliminate potential ellipticity in the waveguide cladding, and to minimize the asymmetry of the output beam [98]. In order to fabricate the in-chip waveguides, we took the following steps. First, we focused the laser to a depth of 2.9 mm in optical axis and formed concentric circles by scanning in x-y plane. Circle diameters were increased in step of $4 \mu\text{m}$ such that the smallest circle radius is $15 \mu\text{m}$ and the largest is $35 \mu\text{m}$, corresponding to $30 \mu\text{m}$ core diameter and $20 \mu\text{m}$ cladding size (Fig. 4.2(b)). Each concentric circle radius is $2 \mu\text{m}$ larger than the previous one, providing a uniform cladding. Then, we repeated this operation at $100 \mu\text{m}$ separated depths along the z-axis until we get 2.9 mm long waveguides. IR transmission microscope images of the cross-section and the top-view of the waveguides proves continuity and uniformity of the modifications (Fig. 4.2(b) and Fig. 4.2(c)).

We also analyzed the roughness of the core-cladding interface. We took 10 measurements across 5 different waveguides. The standard deviation of these measurements is calculated as $1 \mu\text{m}$, corresponding to 6.6 % deviation from the designed radius. This value is comparable with the roughness of depressed-cladding waveguides in other transparent materials [99, 100].

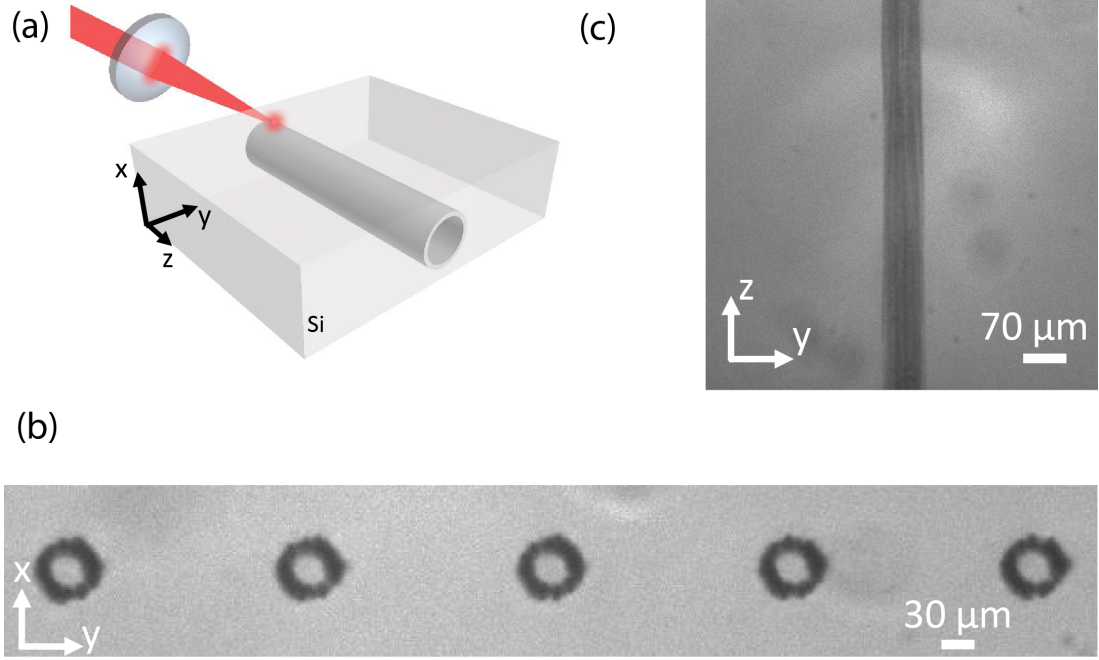


Figure 4.2: (a) Illustration of the longitudinal-writing scheme to form tubular waveguides. (b) IR transmission microscope image showing the exit ports of an array of waveguides. (c) IR image of the top view of a single waveguide.

4.1.2 Optical characterization

To characterize in-chip waveguides, we fabricated ten of them in array configuration with the same writing parameters described in section 4.1.1. From the interferometric measurement results, using $NA \approx (2n\Delta n)^{0.5}$, we expect the waveguides to have a numerical aperture of ≈ 0.05 at $1.3 \mu\text{m}$. Therefore, to increase the coupling efficiency, we coupled $1.3 \mu\text{m}$ laser beam into the waveguides using an aspheric lens with the smallest numerical aperture commercially available, NA of 0.17. We also polished the input and output surfaces of the samples after fabrication in optical quality to minimize scattering. For near field characterization, we imaged the output light from the waveguide exit port with an InGaAs camera (Artray, Artcam-031 TNIR) connected to $60\times$ (Nikon Plan Fluor $60\times /0.85$, WD 0.3) objective. For far field characterization, we moved the imaging plane 1 cm away from the exit port and changed objective to $20\times$ (Nikon Plan Fluor $20\times /0.5$, WD 2.1) to increase the field of view.

Typical near-field image of waveguide output and the corresponding intensity profile are shown in Fig. 4.3(a) and Fig. 4.3(b), respectively. Full-width-half-maximum (FWHM) measured from Gaussian fits of the horizontal and vertical axes in Fig. 4.3(b) are $31 \mu\text{m}$ and $29 \mu\text{m}$, respectively, demonstrating that the output profile is circularly symmetric as expected. Since the beam diameter matches with the core size of the waveguide, near field images prove waveguiding as well. We also used far-field characterization to confirm waveguiding. As the control experiment, we imaged the beam from bare silicon, *i.e.*, from a region without waveguides (Fig. 4.4(a)). Peak intensity of the output light from the waveguide (Fig. 4.4(b)) is higher than the control intensity as shown in Fig. 4.4(c), indicating the light is confined by the modifications and guided along the waveguide.

We repeated far-field measurements at two different imaging planes separated by $500 \mu\text{m}$ to estimate NA of the waveguide. Difference in the FWHM of two intensity profiles and the divergence angle calculated using this measurement can be used to estimate numerical aperture. For control experiment, we measured NA as 0.17, which is the same as the NA of the lens. For waveguide, we calculated divergence angle as 1.95° and estimated waveguide NA as 0.034. From the relation $\text{NA} \approx (2n\Delta n)^{0.5}$, where n is 3.502 at $1.3 \mu\text{m}$, we calculate the magnitude of Δn as 1.6×10^{-4} . This result is in agreement with Δn we obtained with interferometric method. Using the relation $V = 2\pi a \text{NA} / \lambda$, we calculated V-number as 2.4, confirming single-mode output profile from the waveguides.

Loss characteristic is a critical parameter in assessing the waveguide quality. In order to measure the loss coefficient, α , we used two different methods. The first one is based on the scattering measurements [101–103]. In this method, we assume that scattering is uniform along the waveguide and ratio of the scattered light to guided light is the same at any position. Given this condition, decay in the scattered light intensity along the waveguide is directly associated with the optical loss of the waveguide. We placed an InGaAs camera together with a $20\times$ objective normal to the waveguide direction to record the scattered light intensity profile during beam propagation. We performed the measurements around the middle of the waveguide, where effects of reflection from surfaces and uncoupled

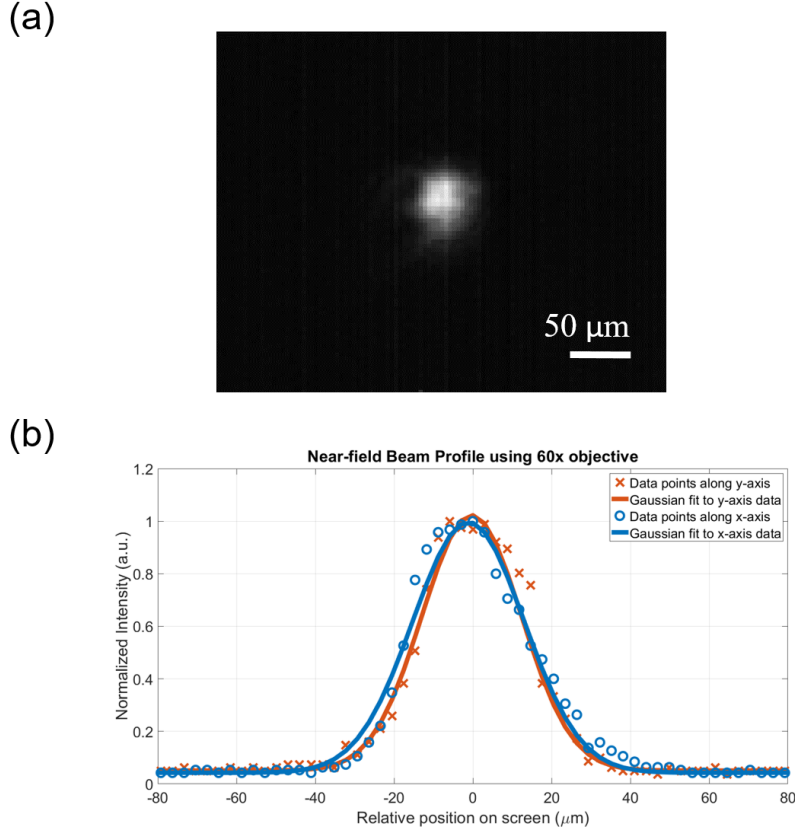


Figure 4.3: (a) The near-field image of the coupled light from the waveguide output taken with 60 \times objective. (b) Near-field intensity profile data measured from (a). Blue circles and red crosses correspond to measured data from horizontal axis and vertical axis, respectively. Solid curves are Gaussian fits to the measured data of the same color.

light are minimized. As predicted from $I(z) = I_0 e^{-\alpha z}$, where I_0 is the intensity at the waveguide entrance and α is the loss coefficient, we observed an exponential decay in the beam intensity in propagation direction (Fig. 4.5). The slope of the fitted curve gives the total loss coefficient, which varies between 1.84-2.44 dB/cm with a mean of 2.18 dB/cm and standard deviation of 0.18 dB/cm for eight waveguides. The loss is originated from the scattering at the core-cladding interface, since the beam propagates in unmodified Si core which has negligible absorption and nonlinear response at 1.3 μm with the operated power.

As an alternative method to measure waveguide loss, we directly evaluated the input-output power relationship. We positioned a 1-mm diameter iris 2.5 cm

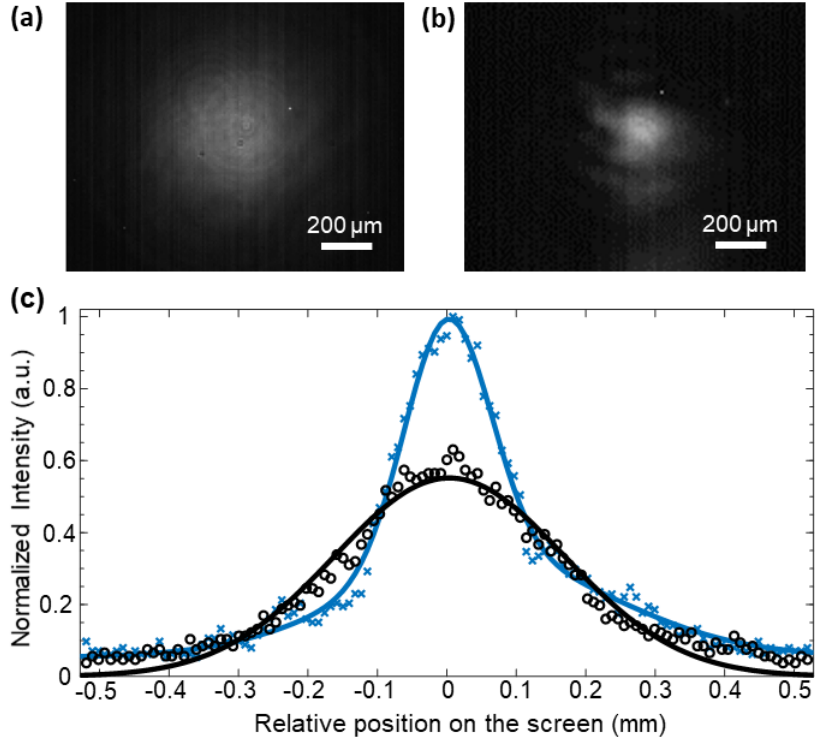


Figure 4.4: (a) Far-field image of the uncoupled light, after passing through unmodified silicon (control experiment). (b) Far-field image of the coupled light. (c) Far-field intensity profiles measured from coupled light (blue crosses) and uncoupled light (black circles). Solid curves are Gaussian fits to the measured data of the same color.

away from the output port, where guided beam size matches the aperture diameter and thus any light except the guided beam is blocked. We coupled 860- μW beam into the waveguide and measured 15 μW after the iris (P_{meas}). As the control experiment, we repeated the same measurement in bare Si and observed 8 μW . This result is consistent with the intensity increase in Fig. 4.4(d). We estimated the power without loss, P_0 , as 16.4 μW , after accounting for Fresnel reflections (3.22 dB), coupling loss (13.98 dB) and insertion loss (17.61 dB). The percentage of the measured power to the incident power before coupling determines the insertion loss and the coupling loss is originated from the mismatch between NA of the waveguide and the coupling lens. Using the relation, $\alpha = 10\log(P_{max}/P_{meas})/L$, where L is the waveguide length, we calculated α in the range of 1.36-1.52 dB/cm with a mean of 1.4 dB/cm and standard deviation of

0.06 dB/cm. Loss coefficients obtained from both scattering measurements and the power measurements are in reasonable agreement with each other and they are the lowest reported for buried waveguides in Si.

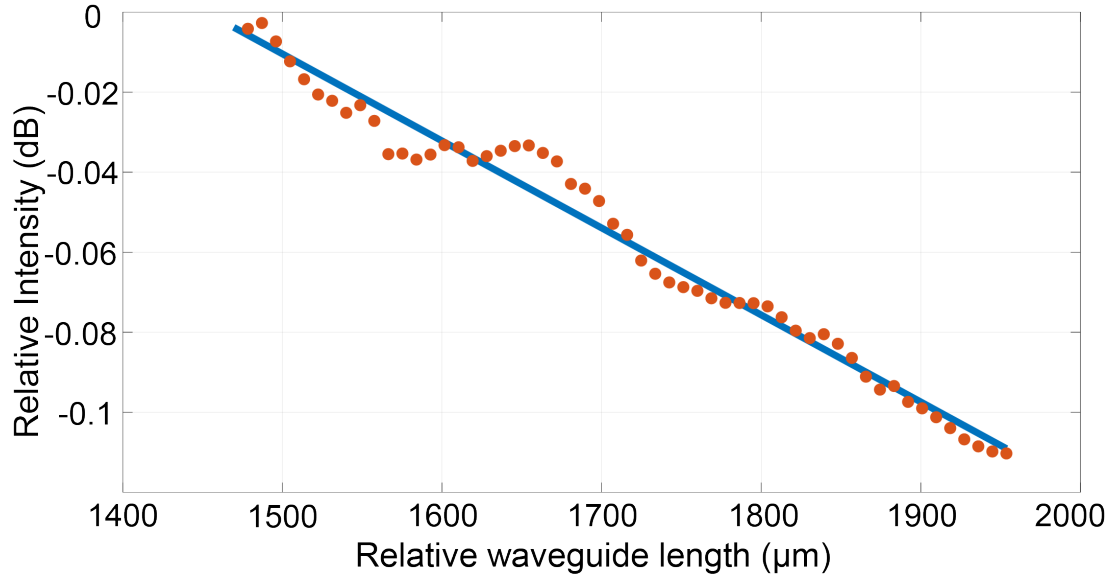


Figure 4.5: Scattered light intensity (orange dots) is used to characterize the waveguide loss. 10-pixel moving average filter is applied to get the general profile. Blue curve represents the fitted curve.

In summary, we demonstrated that laser-induced modifications with negative refractive index change can be used to fabricate in-chip waveguides. Index depression of $\approx 2 \times 10^{-4}$ allows a tubular geometry in waveguide design. The waveguides operating at $1.3 \mu\text{m}$ was characterized with the near- and far-field intensity profiles. Loss coefficient was estimated using two different methods and both measurements confirmed that the waveguides have the lowest loss reported so far. Their low loss, long extent, and the demonstrated in-chip capability is expected to contribute to near-IR applications in integrated optics, optofluidic sensors and Si-photonics [79].

4.2 Femtosecond laser written waveguides deep inside silicon

Femtosecond lasers are the dominant laser type in material processing, mainly due to better precision, minimal heat-affected zone, higher peak power. Previous attempts in generating permanent modifications inside silicon with femtosecond lasers encountered problems such as beam delocalization, preventing irreversible changes in the material [25, 26]. These studies mostly focused on single-shot regime, where pulse to pulse interaction is avoided. In this study, I contributed to the demonstration of the in-chip modifications using femtosecond pulses by exploiting cumulative effects [95]. Positive refractive index in this configuration allowed a simple geometry for the waveguides.

For the waveguide fabrication, we used a pump-probe setup, where the laser source operates at $1.5 \mu\text{m}$ and generates pulses with more than $2 \mu\text{J}$ energy and 350 fs pulse width. Repetition rate is set to 250 kHz . Collimated output from the laser is divided into two parts, namely pump and probe arms. On the pump arm, we placed a combination of half-wave plate (HWP) and polarizing beam splitter (PBS) to adjust the power for bulk Si modification. We focused the pump beam into the sample by using a 0.5 NA aspheric lens. On the probe arm, we implemented a delay line with a pair of mirrors to generate time delay between pump and probe beams so that we can investigate the plasma evolution. We imaged the probe beam with an InGaAs camera attached to $10\times$ objective. We prepared $\approx 5 \text{ mm}$ wide, 1 mm thick Si samples for the experiments by dicing a double side polished Si sample and polishing the sides.

We focused the pump beam close to the back surface of the sample or to the proximity of an already modified region and generated subsurface modifications with $2 \mu\text{J}$ pulse energy. By translating the sample in the laser propagation direction, it is possible to use previous modifications as seed for the next pulse and elongate the modification. We observed that continuous, 5 mm long, wire-like structures can be created with the scanning speeds in the range of $0.03\text{-}0.1 \text{ mm/sec}$. Limitation in the maximum scanning speed indicates the necessity of

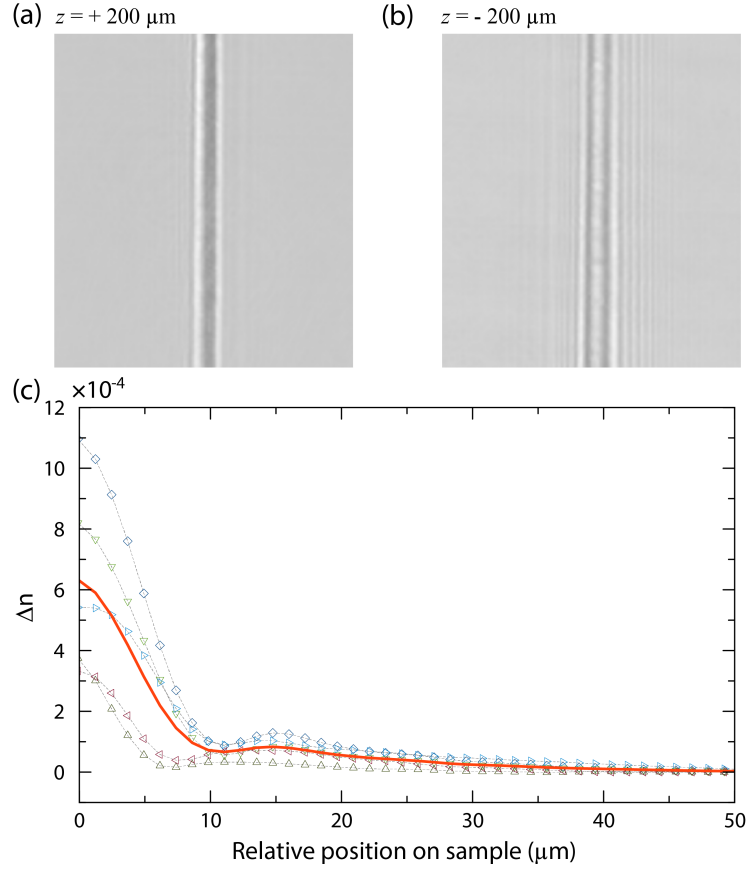


Figure 4.6: IR images obtained with InGaAs camera when the waveguide is located (a) $200 \mu\text{m}$ away from the focal plane closer to the camera, (b) $200 \mu\text{m}$ further away from the imaging plane. (c) Using such IR images and inverse Abel transform Δn profile is calculated. Red solid line is obtained from the average of the five waveguides, whereas black dashed lines show individual measurements.

pulse to pulse effect for structure formation. From the images we obtained by blocking the pump arm and using the probe arm as the light source, we found that the refractive index change (Δn) induced by the femtosecond pulses is positive and the modifications are phase object [104]. Therefore, we could apply inverse Abel transform to calculate Δn using the microscope images at different focusing Fig. 4.6(a) and Fig. 4.6(b). From five waveguides fabricated with the identical parameter set, we calculated Δn as 6×10^{-4} (Fig. 4.6(c)). Typical errors in the calculated refractive index change in optical fiber using this method is 15 % [105]. That indicates the large difference in Δn originates from the non-uniformities in the waveguide fabrication.

Further, we designed optical waveguides using $\Delta n > 0$ structures as building blocks. Fabricated waveguides have a diameter of $20 \mu\text{m}$ and are 5.5 mm long. We confirmed waveguiding with the same far-field measurement method detailed in 4.1.2. We coupled 10 mW continuous-wave (CW) laser at $1.5 \mu\text{m}$ into these waveguides with an aspheric lens of $\text{NA} = 0.2$. We recorded the light intensity from the unmodified silicon (control measurement (Fig. 4.7(a-i))) and the waveguide output intensity (Fig. 4.7(a-ii)) with an InGaAs camera recording at the far field. From these images, we observed that the light confined along the waveguide results in higher intensity compared to control measurement at the same distance ((Fig. 4.7(b))). Furthermore, beam diameter on the output port is $\approx 20 \mu\text{m}$ at the silicon surface, equal to the core diameter, demonstrates waveguiding (Fig. 4.7(a-iii)). We calculated the refractive index change from far-field images as 3.5×10^{-4} which is in good agreement with inverse- Abel transform calculation.

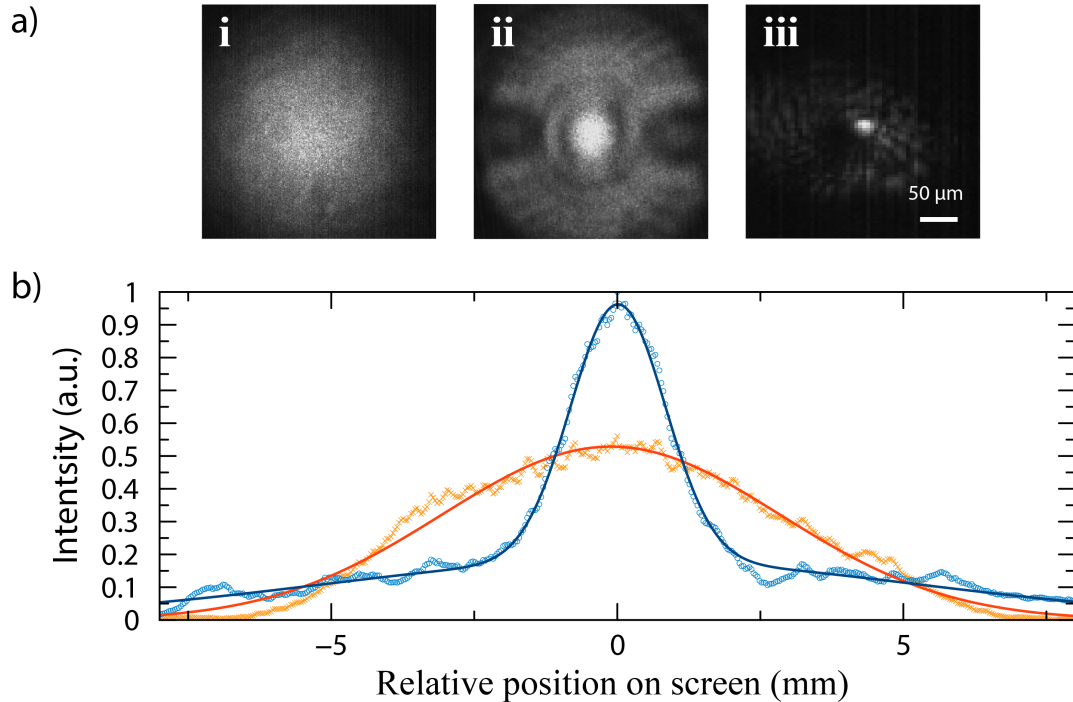


Figure 4.7: (a) i. Far-field image of the uncoupled light (control experiment), ii. Far-field image of the coupled light, iii. Near-field image of the coupled light. (b) Far-field intensity profiles measured from coupled light (blue circles) and uncoupled light (orange crosses). Solid curves are Gaussian fits to the measured data of the same color.

For loss characterization, we evaluated input-output power relationship, similar to the method explained in chapter 4.1.2. With 16 mW incident laser power, we measured the power from the unmodified Si (control experiment) and waveguide output power as 6.5 mW and 0.45 mW, respectively. Here, waveguide output power corresponds to 7.1 % of the power measured from control experiment. This value is comparable to coupling efficiency estimated from the NA mismatch between the coupling lens and waveguide ($\approx 7 - 8 \%$), indicating that the loss coefficient of the waveguide (α) is negligible compared to coupling loss and the Fresnel reflections. Therefore, we can put an upper limit to the loss coefficient by using Fresnel reflection (3.22 dB) as 5.85 dB/cm.

In summary, we demonstrated that it is possible to generate in-chip modifications with femtosecond pulses by exploiting the thermal effects originated from high repetition rates. We observed a positive refractive index change (Δn) induced by the femtosecond pulses using inverse-Abel transform. This allows type-I waveguide geometry, where modifications are directly used as the waveguide core. We characterized 5.5-mm long waveguides by analyzing their far-field images, concluding that $\Delta n = 3.5 \times 10^{-4}$.

Chapter 5

3D sculpting in Si with preferential etching

In order to etch in-chip Si structures selectively, a new etching process is needed. Although conventional anisotropic etchants like KOH is used for removing Si with crystal orientation other than $\langle 100 \rangle$ [106], there is no wet etchant specifically designed for laser induced subsurface modification removal. Ideally, the etching solution should be CMOS compatible for future potential electronic-photonics integration, stable, effective at room temperature, highly selective to modified regions and minimally damage unmodified crystal.

For this purpose, in collaboration with GUNAM-METU we developed an acid based, wet chemical etching process that satisfies all these conditions and demonstrated selective removal of in-chip Si modifications. Using this process, we were able to create through-Si vias, ultrathin Si slices with high uniformity and buried microchannels that were used for chip cooling [19].

5.1 Chemical etching process

The etching solution we develop is acid based and contains 0.05 M of copper (II) nitrate ($\text{Cu}(\text{NO}_3)_2$), 10 M of hydrofluoric acid (HF), 4 M of nitric acid (HNO_3) and 3.5 M of acetic acid (CH_3COOH). The process is based on the oxidation of Si and immediate dissolution of the oxidized Si [107]. In the etchant, HNO_3 acts as an oxidizing agent and HF dissolves the product of the oxidation [108, 109]. CH_3COOH is used for diluting the reactant concentration. It also helps for smoother etched surface by decreasing the solution's surface tension [110]. $\text{Cu}(\text{NO}_3)_2$ is used for higher selectivity due to its low activation energy [111, 112].

An electrochemical process occurring with the help of current on the local anode and cathode regions on the surface generated by oxidation-reduction reaction is the main mechanism of the developed process, similar to chemical etching of semiconductors [109, 110]. Therefore, the mechanism includes generation of excess charge carriers. We also suggest that the process is a two-step process, since H_2 is generated during dissolution. Experimentally, we observed a color change from light blue to green in the etchant, indicating nitric oxide generation (NO) [112]. During the process, HNO_3 and Cu^{+2} ions play a critical role in balancing carrier densities. Electron capturing of Cu^{+2} ions provide necessary holes for the current flow and HNO_3 prevents formation of Cu nanoparticles on the etching interface [113].

Furthermore, we evaluated the selectivity of the developed etchant on in-chip modifications and compared it KOH, which is a commonly used etchant for silicon (Fig. 5.1). We prepared a laser-processed sample containing 40 μm separated lines in the plane normal to the laser propagation direction (x - y plane). We diced the sample into two through x -axis and put one half into the developed solution and the other half into KOH for 10 minutes. Although KOH removed laser-induced modifications, the structure width increased from $\sim 1 \mu\text{m}$ to 10 μm after etching (Fig. 5.1(b)). However, the structure width remained the same after the developed etchant was used (Fig. 5.1(c)). We attributed the higher selectivity to the uneven Cu^{+2} ion concentration and consequently different electronegativity

on the interface between modified and unmodified silicon.

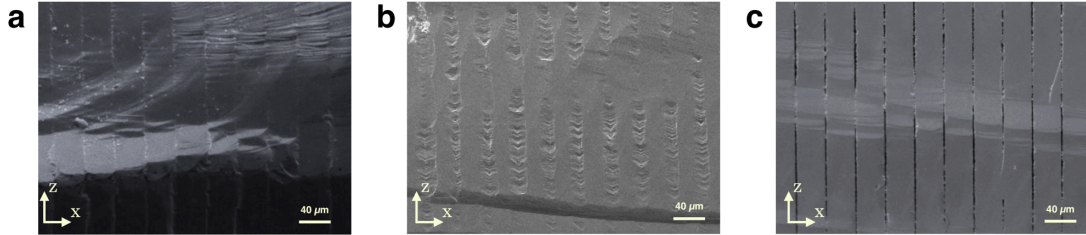


Figure 5.1: (a) SEM image of the cross-section of the laser processed region before etching. Laser propagation direction is $+z$. (b) Cross-section SEM image of the modified region after 10 minutes of KOH etching. (c) Cross-section SEM image of the modified region after treated with the developed etchant. Due to high selectivity, the etched region has a sharp contrast.

5.2 Examples of applications with developed etchant

5.2.1 Micropillar arrays

Selective removal of the in-chip structures can be used to create 3D complex structures in large area with high uniformity. Before etching, we used polish removal and made the modified region accessible to the etchant through $x-y$ plane. Dicing is an alternative method if the modified areas to be etched are positioned in $x-z$ plane. For the first case, $4\text{ mm} \times 4\text{ mm}$ area covered with $20\text{ }\mu\text{m}$ by $30\text{ }\mu\text{m}$ wide and $500\text{ }\mu\text{m}$ long pillars can be revealed in 20 minutes (Fig. 5.2). It is also possible to adjust the dimensions and the final shape by designing the laser processing pattern and the etching duration.

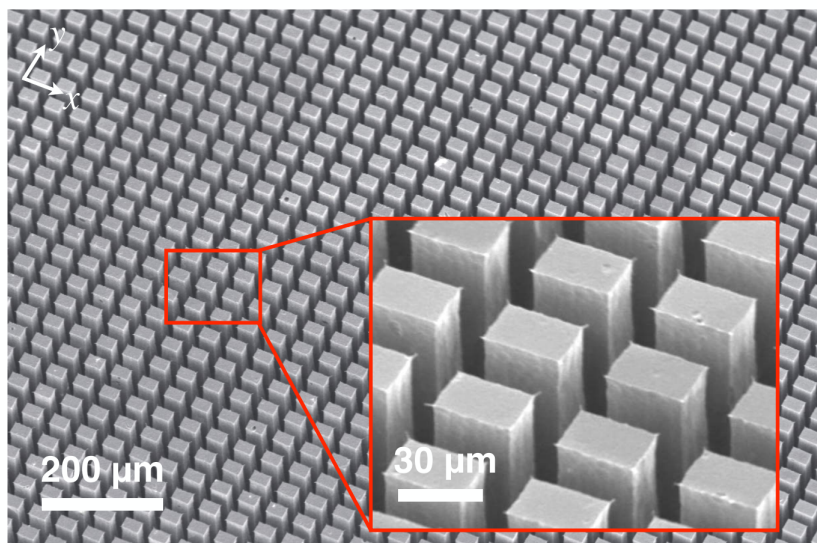


Figure 5.2: SEM image of the high-aspect ratio pillars covering $1.5 \text{ mm} \times 1 \text{ mm}$ area. The inset is the zoomed-in image of a portion of the same area.

5.2.2 Through-Si vias

Through-Si vias are crucial structures for three-dimensional, high-density, large-scale chip integration [114]. We demonstrated $50\text{-}\mu\text{m}$ radius vias using the etching solution we developed. The method we used is illustrated in Fig. 5.3. As the first step, we created in-chip cylinders with a single circular motion of the laser, which corresponds to the perimeter of the top surface (Fig. 5.3(a) and Fig. 5.3(b)). We polished top and bottom surfaces to reveal the laser written modifications. We treated the sample with the etchant for two minutes and $200\text{-}\mu\text{m}$ long cylinders were cut through (Fig. 5.3(d)). SEM image of the final structures is shown in Figure 5.4. Metal layer can be deposited in these vias to form a conductive channel between two sides of the wafer.

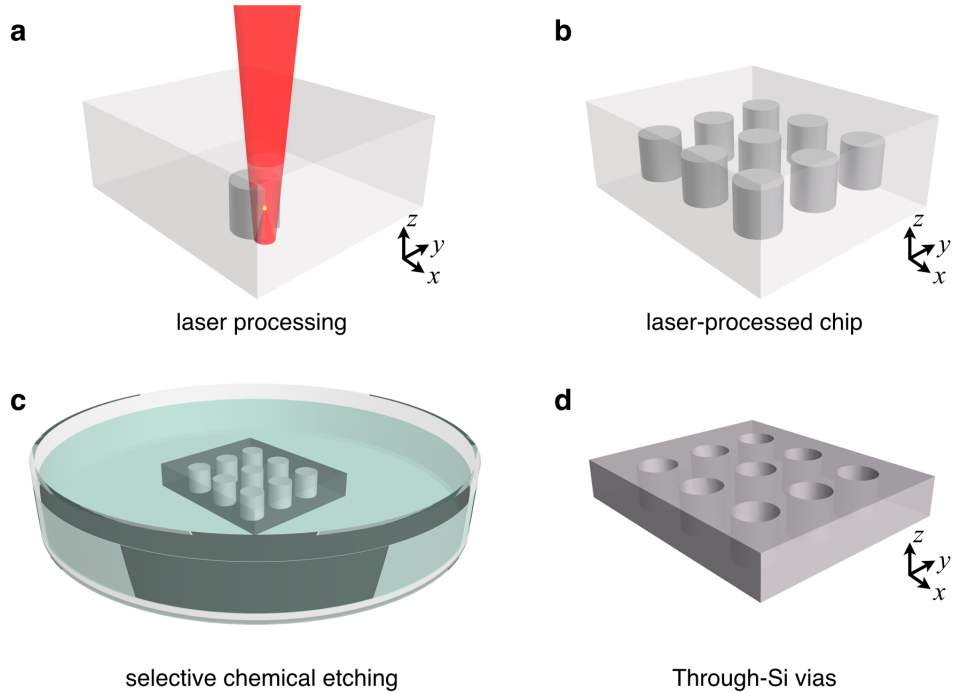


Figure 5.3: (a) A single circular motion is enough for the laser processing of vias. (b) An array of cylinders can be created in large area. (c) After polishing both sides of the sample, Si wafer is placed into etchant for two minutes. (d) Highly uniform array of vias can be obtained with the method.

5.2.3 Cantilever-like structures

As another example of complex 3D structures that can be fabricated using selective etching of silicon, we demonstrated cantilever-like structures (Fig. 5.5). To fabricate subsurface walls, we raster-scanned the sample. Single pass of the laser at 150 kHz generated 500 μm long in-chip walls. We polished top and bottom surfaces and treated the sample with the etchant. Similar to the process in chapter 5.2.2, removal of the modified Si revealed the final structure in the form of cantilevers. Period of the raster scan controls the cantilever thickness (Fig. 5.5(a)) and the roughness of the walls in Fig. 5.5(b) was measured as $\sim 1 \mu\text{m}$.

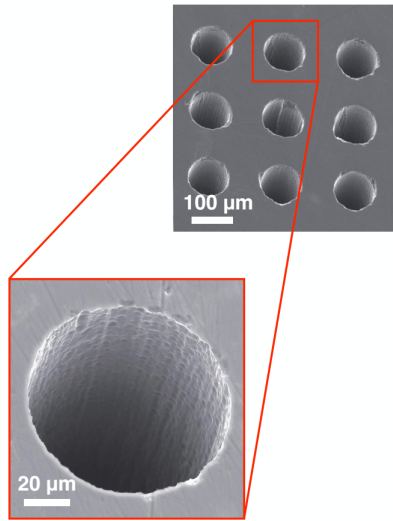


Figure 5.4: SEM image of through-Si-vias that cut across the entire chip.

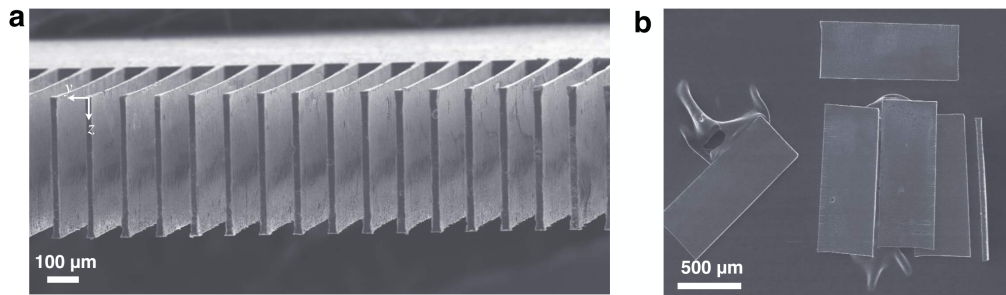


Figure 5.5: (a) Cantilever length can be designed during the scanning and can be few millimeters long. (b) SEM image of the $30\ \mu\text{m}$ -thick walls.

5.2.4 Silicon slicing

Ultrathin slicing of silicon ($< 100\ \mu\text{m}$ thickness) has important applications, specifically in photovoltaics. The active region of Si-based photovoltaic devices is generally fabricated on top the surface of the wafer, whereas the rest remains untouched. Developing crystal thin films have been proposed as a solution to this loss [115]. Although various methods are used in producing thin films such as reactive ion etching [116,117], there is no laser based approach for silicon thinning. We sliced Si wafer into $30\ \mu\text{m}$ thick pieces with $\sim 1\ \mu\text{m}$ surface roughness by combining laser processing and etching (Fig. 5.5(b)). Due to the flexibility of the process, we demonstrated wafer slicing in different geometries, which is a

potential alternative to surface structuring (Fig. 5.6).

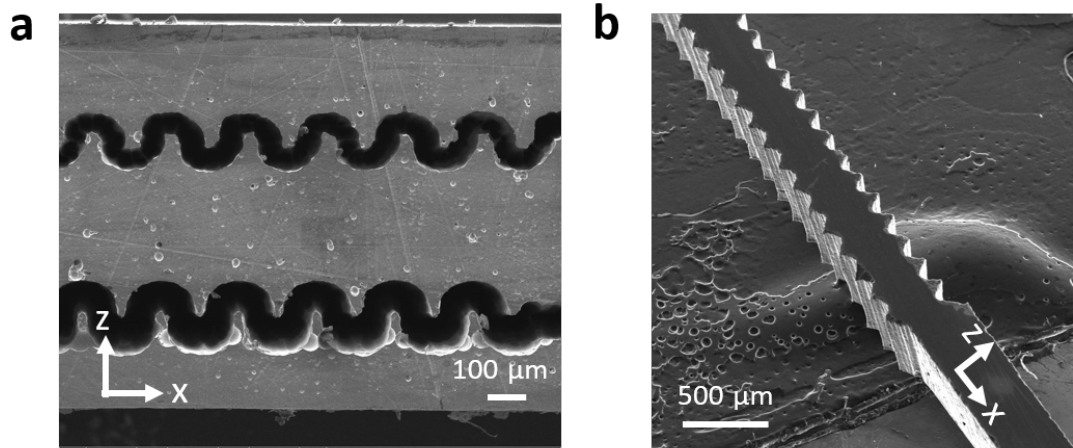


Figure 5.6: (a) Cross-section SEM image of the sliced Si during etching before it is fully detached. (b) SEM image of the sliced sample after etch treatment.

5.2.5 Microfluidic channels

Increase in the clock rates has slowed down, mainly due to overheating of microprocessors [118]. Replacing externally connected, metal heat sinks with fully buried microfluidic channels is considered as the most promising solution to overcome this bottleneck [119]. We demonstrated an example of chip cooling in silicon using the microfluidic channels we carved with the etchant we developed. First, we processed an 8-mm long rectangular volume with $200\ \mu\text{m} \times 200\ \mu\text{m}$ end surfaces. We chemically treated the sample for 8 hours, corresponding to $500\ \mu\text{m}/\text{hour}$ etch rate. Then, we passed $< 10\ ^\circ\text{C}$ water through the channel in room temperature and observed a $4\ ^\circ\text{C}$ drop on the surface temperature within seconds (Fig. 5.7(a)). It is also possible to increase the interaction area by creating curved microchannels.

In summary, we developed an acid-based etchant to remove laser induced sub-surface modifications with high uniformity and high selectivity. Using laser processing followed by etching, we demonstrated a variety of applications including large area structuring, through-Si vias, silicon slicing and chip cooling with fully

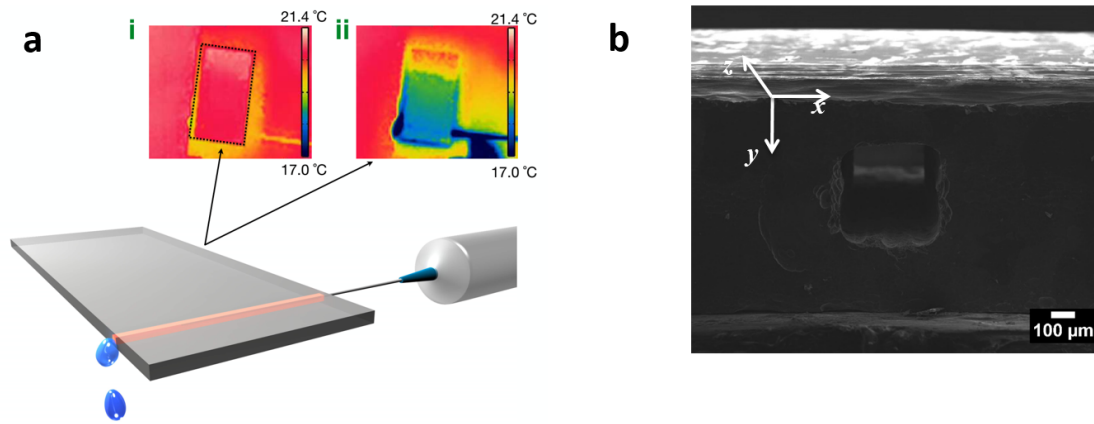


Figure 5.7: (a) The illustration of the cooling experiment. Inset shows the temperature profile before (i) and after (ii). (b) SEM image of a buried microfluidic channel.

buried microfluidic channels (Fig. 5.7(b)).

Chapter 6

Investigation of new processing regimes for in-chip structures

In order to extend the in-chip device fabrication capabilities and discover new dynamics, we investigated different pulse parameters and pulse shapes. Spatial-control of subsurface modifications can potentially provide precise phase control and they are highly desirable for in-chip gray-level holograms. For this purpose, we tried Gaussian beam operating at $2\ \mu\text{m}$ and Bessel beam for subsurface processing and characterized the fabricated structures.

We demonstrated $< 1\ \mu\text{m}$ modifications inside silicon for the first time, to the best of our knowledge, by using Bessel beams. With this approach, we obtained in-chip structures with an aspect ratio > 100 . We also demonstrated subsurface silicon processing with $2\ \mu\text{m}$ pulsed lasers. We measured multi-shot modification threshold as $\approx 0.2\ \text{GW}/\text{cm}^2$. For investigation of different regimes, we started to build a burst mode system operating at $1.98\ \mu\text{m}$ wavelength.

6.1 Spatial-control of laser-written in-chip Si structures with Bessel beams

In laser-material processing, Gaussian beam is the most commonly used beam type [120]. However, Gaussian beams have certain limitations in transparent material processing, such as spherical aberration and limited focal depth [121, 122]. Thus, to fabricate high-aspect-ratio structures inside a material, it may be necessary to scan the laser multiple times. On the other hand, Bessel beams can have longer depth-of-field compared to Gaussian beams due to their “non-diffracting” nature [123]. Using this property, it has been shown that it is possible to generate high-aspect-ratio modifications inside bulk glasses with a single shot [124, 125]. Similar approach has been tested in silicon with femtosecond pulses, but no subsurface modification has been observed [26]. Currently, the minimum feature size of in-chip structures remains at $1\text{-}\mu\text{m}$ scale, obtained with nanosecond pulses [19]. Subsurface modifications with nanoscale feature sizes and high-aspect ratios can be potentially useful for fabricating nanograting [126], photonic crystals [127] and phase holograms [128] operating in the near-IR.

6.1.1 Bessel beam generation

There are several methods to generate Bessel beams; such as aperture-based methods, axicon lenses and spatial light modulators (SLM) based methods. Although using axicon is the most common way for Bessel beam generation due to high power efficiency, SLM-based methods became popular thanks to their ability to get any phase pattern as input and produce corresponding beam profile without any change in the overall setup [122]. Due to its flexibility, we chose to use SLM in our experiments to transform Gaussian beam to Bessel beam.

The setup for subsurface Si processing with Bessel beams is shown in Fig. 6.1. As the laser source, we used a system operating at $1.55\ \mu\text{m}$ and generating $30\ \mu\text{J}$, $5\ \text{ns}$ pulses with $150\ \text{kHz}$ repetition rate [19]. To maximize the phase modulation

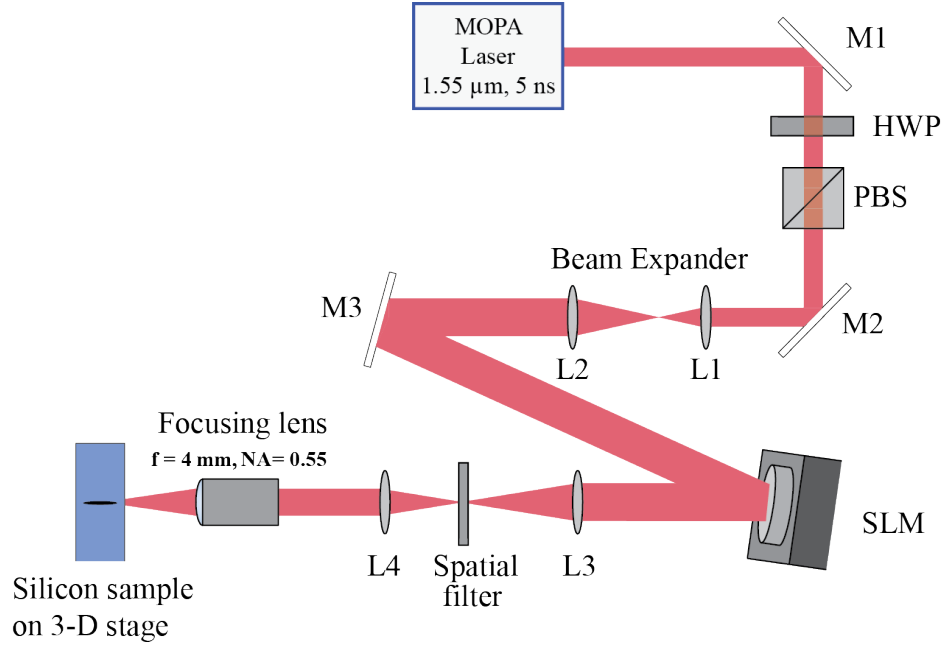


Figure 6.1: The schematic showing the experimental setup for generating Bessel beam. MOPA: Master-oscillator-power-amplifier; M1- M3: silver mirrors; L1- L4: plano-convex lenses; HWP: half-wave plate; PBS: polarizing beam splitter; SLM: Spatial light modulator.

provided by SLM (Hamamatsu X10468-8), we applied the following steps: Laser output is directed to a polarizing beam splitter (PBS) together with a half wave plate (HWP) to linearly polarize the beam. We placed a 4f system, consisting of $f = 1.5$ cm and $f = 4$ cm lenses, to expand 2.8 mm beam diameter to 7.5 mm diameter to cover the active area of the SLM and we kept the incidence angle lower than 10^0 degrees. To efficiently separate the diffraction orders, we added a blazed grating to the phase mask. We aligned the rest of the system such that +1 diffraction order is used for processing. We placed another 4f system after SLM, with $f = 12.5$ cm and $f = 10$ cm lenses, to scale down the beam diameter to 6 mm and to fill the focusing lens aperture completely without any loss in the beam profile. We eliminated zeroth and higher diffraction orders by placing a spatial filter between this 4f system. An aspheric lens ($NA = 0.55$, $f = 4$ cm) generated the zero order Bessel function of the first kind at the focal point. A typical transverse image and the corresponding intensity profile of a Bessel pattern generated with this configuration is simulated and shown in Fig.

6.2(a) and 6.2(b), respectively.

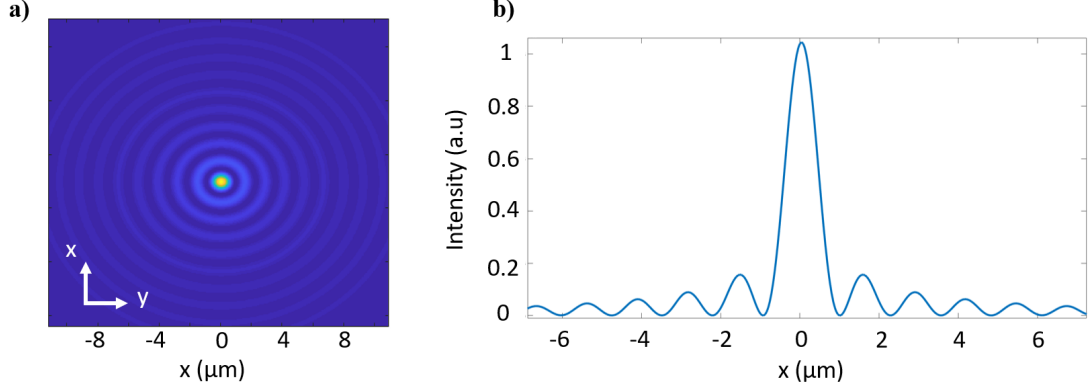


Figure 6.2: (a) Simulation of transverse profile of a Bessel pattern at the focal point of the aspheric lens. (b) Horizontal intensity profile of the pattern shown in (a).

6.1.2 In-chip structures and characterization

We generated in-chip structures using two different writing schemes, namely longitudinal and transverse writing. In both cases, we set the pulse energy to $3.5 \mu\text{J}$ and polarization to linear. In order to test the effect of Bessel beam central diameter on the structure width, we first created in-chip modifications with longitudinal writing. We focused the beam close to the back surface of the double side polished, 1 mm thick Si sample and moved the focal position of the beam towards the front surface with a speed of 0.1 mm/sec. We repeated the experiment for different Bessel beam diameters ranging from $\sim 1 \mu\text{m}$ to $10 \mu\text{m}$. Fig 6.3 shows IR microscope images of structures written with two different Bessel beam diameters, ($\sim 1 \mu\text{m}$ and $3 \mu\text{m}$). Although, we kept all processing parameters the same, modification diameter tripled, increasing from $6.15 \mu\text{m}$ to $18.45 \mu\text{m}$. This demonstrates control over the structure width using Bessel beams. The mismatch between expected and observed structure diameters is originated in the multipulse effect due to longitudinal scanning. In this configuration, in-chip structures generated by Gaussian beam has also larger diameters than calculated.

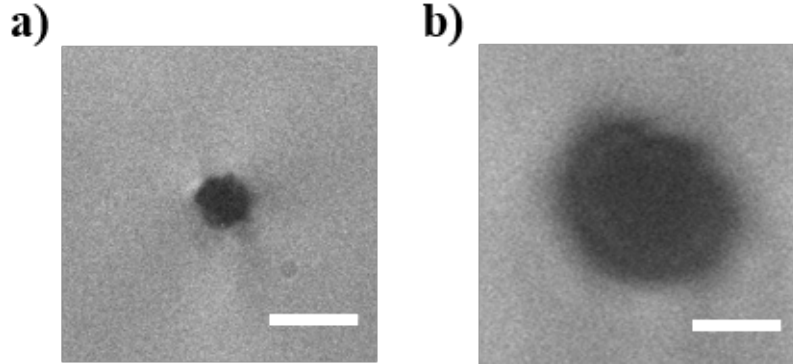


Figure 6.3: Infrared transmission microscope images of longitudinally-written structures from the top. In-chip structures written using Bessel beam with core diameter (a) $\sim 1 \mu\text{m}$ and (b) $3 \mu\text{m}$. Scale bar is $10 \mu\text{m}$ for both images

In transverse writing scheme, we focused on creating in-chip modifications using Bessel beams with $< 1 \mu\text{m}$ diameter. It should be noted that due to the nature of multi-photon absorption, it is possible to obtain submicron structures with $\sim 1 \mu\text{m}$ spot size. We focused the beam $500 \mu\text{m}$ below the entrance surface and scanned the laser in the plane perpendicular to optical axis, parallel to polarization direction with a speed of 1 mm/sec . To image the cross section of the structures, we diced the sample perpendicular to scanning direction in unmodified region and applied mechanical force to fully separate the sample. SEM images of the in-chip modifications induced by $1.28 \mu\text{m}$ diameter Bessel beam is shown in Fig 6.4(a). The structures elongate for $300 \mu\text{m}$ in optical axis and we measured their width as 500 nm , demonstrating the first in-chip nanostructuring of silicon. From SEM images in Fig 6.4(b), it can be seen that modifications are accompanied by $\sim 150 \text{ nm}$ voids. High aspect ratio structures with voids are observed in silica and explained with microexplosions [129].

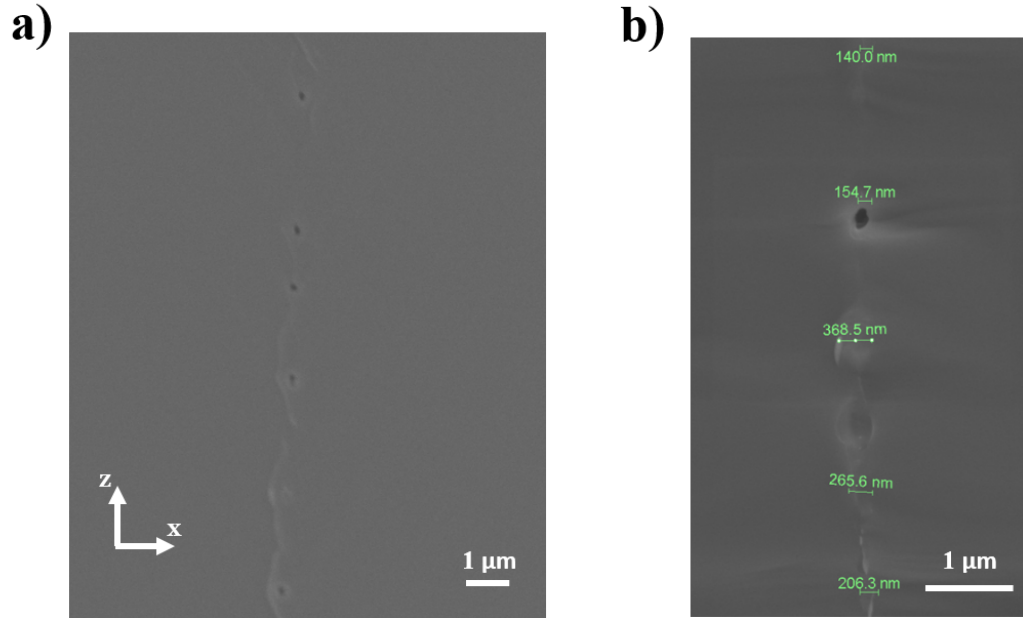


Figure 6.4: SEM images of transversely written structures from the cross-section. (a) Submicron structures written using Bessel beam with core diameter of $\sim 1 \mu\text{m}$. (b) Zoomed-in image showing 150-nm void.

6.2 Processing at $2 \mu\text{m}$

Nonlinear Kerr index of silicon reaches its maximum at $2 \mu\text{m}$ and approximately doubles the index at $1.55 \mu\text{m}$ [130, 131]. Such a change might affect the nonlinear mechanism during the structure formation. Therefore, in-chip modifications generated with $2 \mu\text{m}$ lasers might have different optical properties than those fabricated with $1.55 \mu\text{m}$.

6.2.1 Results

In the experiments, we used a home-built Thulium system operating at $2.09 \mu\text{m}$ and generating 32 ns pulses with 100 kHz repetition rate. In this configuration, the pulse energy reaches $32 \mu\text{J}$. Since pulse duration, repetition rate and pulse energy are similar to the $1.5 \mu\text{m}$ system we used [19], it is possible for us to investigate the effect of processing wavelength on in-chip structures using this

system. We adjusted the processing power by changing the pump power of the last amplifier stage and used unpolarized light. Silicon samples were p-doped (5-15 $\Omega\cdot\text{cm}$), 1-mm thick, double side polished, having the same properties with our earlier experiments.

We scanned the laser at 400 μm below the entrance surface with different pulse energies to determine the modification threshold experimentally. During the threshold calculation, we assumed that the only loss in the optical path after the focusing lens is the reflection from the entrance surface and the beam energy is confined in the calculated beam diameter. IR microscope images in Fig. 6.5(a) and Fig. 6.5(b) shows in-chip structures written with pulse energies 10 μJ and 1 μJ , respectively. As the energy decreases structures form in a discontinuous manner, indicating the intensity is getting closer to the threshold. We didn't observe any modifications with pulse energies below 600 nJ. Thus, modification threshold can be calculated as 0.15 GW/cm^2 , considering the beam diameter of $1/e^2$ is 4 μm at the focal point. The estimated threshold intensity at 2 μm is approximately one order of magnitude smaller than the ones reported at 1.5 μm and 1.3 μm [19,31].

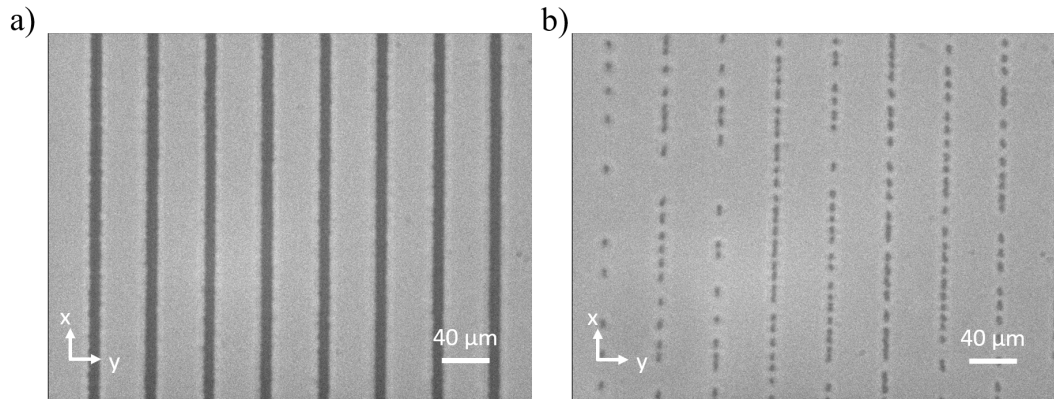


Figure 6.5: IR microscope images of in-chip modifications written with 2 μm pulses. Pulse energies are (a) 10 μJ and (b) 1 μJ .

6.2.2 Development of burst-mode thulium system

In order to investigate different laser-material interaction regimes inside silicon at high repetition rates, we built a burst-mode thulium fiber laser system operating at $1.98 \mu\text{m}$. The system is a modified version of a published study [132] and produces 500 ns burst envelopes at 100 kHz repetition rate with an average power of 1 W. Intra-burst repetition rate is set to 1 GHz and depends on the order of the harmonically mode-locked oscillator. Individual pulses have 20 nJ energy and 15 ps temporal width. Pulse duration can be decreased to < 1 picosecond by dispersion management, if femtosecond pulses are needed for the experiments.

Schematic of the system is shown in Fig. 6.6. We used a harmonically mode-locked oscillator whose fundamental repetition rate is 114 MHz at its ninth order to generate optical signals. The output power is 40 mW and the pulse duration is 1.5 ps. We measured the spectral width as 14 nm, centered around 1980 nm. To enable amplification, we stretched the pulses to 30 ps by using 26.9 m of UHNA7 fiber. In the first amplifier stage, we used 3.45 m of double-clad Tm-doped fiber and increased the signal power to 2 W with a conversion efficiency of 35 %. Using an acousto-optic modulator (AOM), signal is converted into bursts with 50 kHz repetition rate and 500 ns burst duration. Since, the system is polarization-maintaining (PM) until this point, pulse duration drops to 1 ps and soliton self-frequency shift (SSFS) is generated [133,134]. To overcome this problem, we added 50 m of UHNA7 to the system so that polarization is converted to mixed polarization and pulse duration increases to 50 ps. Due to burst generation and splice losses between UHNA7 and SMF28, we measured the power as 600 mW. Therefore, we built another amplifier stage increasing the power to 1 W and pulse energy to 20 nJ. Optical spectrum and measured autocorrelation of the output pulses are shown in Fig. 6.7(a) and Fig. 6.7(b), respectively.

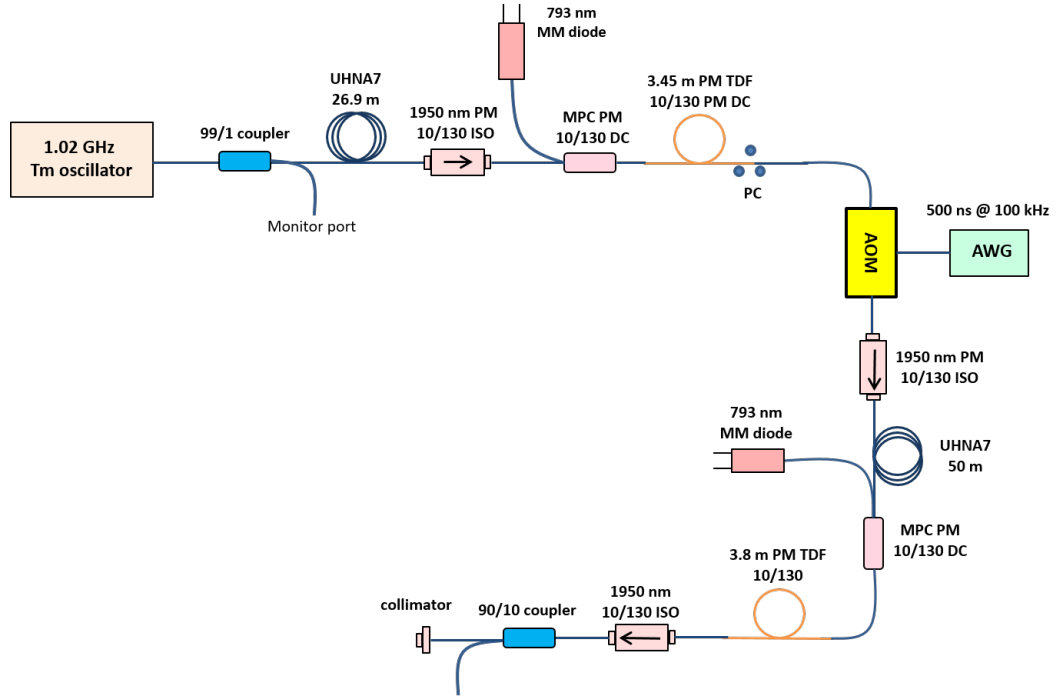


Figure 6.6: Schematic of the burst-mode Tm fiber laser system.

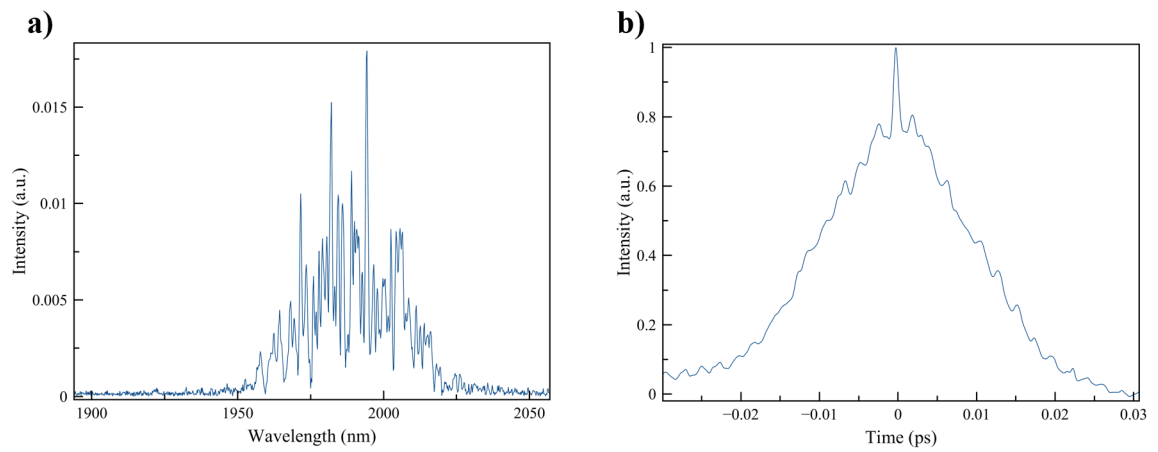


Figure 6.7: (a) Output spectrum is centered around 1980 nm. (b) Pulse duration is measured as 15 ps.

6.3 Subsurface structuring of GaAs

Gallium arsenide (GaAs) has many advantages over Silicon (Si) in different fields such as photovoltaics [135] and in optoelectronics [136, 137] due to its unique properties such as wide transparency window, from 870 nm to 16 μm [138], high electron mobility, high thermal conductivity and its direct bandgap. GaAs-based optoelectronics components can be used in high frequency applications and generate less noise, which is critical in small signal amplification. Currently, using conventional techniques only the top layer can be used for optical device fabrication. Considering high cost of the wafers is one of the main limitations in the widespread use of GaAs in photonics industry, creating three-dimensional modifications buried inside GaAs to utilize the whole bulk becomes more critical. Moreover, such capability can open up new paths for novel design architectures for various fields. Recently, we reported a laser-based method to fabricate 3D structures deep inside silicon [19]. In this work, we demonstrated the first laser-induced modifications inside GaAs with nanosecond pulses using a similar method and showed that it is possible to transfer the capability we demonstrated in Si to other semiconductors, in this instance, GaAs. Refractive index difference in the laser-modified region can be used as building blocks for optical device fabrication, including lenses, waveguides and holograms.

Furthermore, we demonstrated self-organized nanogratings inside GaAs which is desirable for fabricating 2D photonic crystals with sub-micron spacing and increasing second harmonic generation efficiency [139, 140]. In ferroelectric materials such as LiNbO_3 , electrically induced periodic poling improved phase matching during second harmonic generation, which resulted in higher conversion efficiencies [141]. GaAs is favorable in such applications due to its wide infrared transparency and its high nonlinearity. So far, wafers with different crystal orientation are grown or bonded on top each other to have that effect [142, 143]. Although it is possible to reach feature sizes in the order of nanometers with that method, it requires multiple steps to get periodic structures. Laser-induced, self-organized nanogratings can significantly reduce the complexity of the procedure.

In our experiments, we used a home-built master oscillator power amplifier (MOPA) system that works at $1.55 \mu\text{m}$, producing 5 ns pulses with $30 \mu\text{J}$ pulse energy at 150 kHz repetition rate. The laser system is coupled to a computer-controlled 3-axis motorized stage (Aerotech, ANT130-XY, ANT95-L-Z) which is used for sample alignment the processing. Details of this system is explained in our paper [19]. Experiments were performed using Si-doped, double side polished, $500 \mu\text{m}$ thick GaAs wafers with doping concentration of 10^{18} cm^{-3} .

We focused IR pulses into GaAs using a lens with numerical aperture (NA) of 0.68. Under this focusing condition, Rayleigh length is calculated as $57 \mu\text{m}$ in GaAs. Although this is comparably smaller than the wafer thickness ($500 \mu\text{m}$), when we focused the beam directly inside GaAs and increase the power gradually, we observed surface damage together with the subsurface modifications. This means that by the time we reach the bulk damage threshold, surface modification threshold is already reached even the laser is not focused on the surface. We confirmed this claim with a simple calculation: Visible modifications with IR microscope starts at the pulse energy of $12 \mu\text{J}$. In that case, considering the laser parameters together with the focusing conditions, intensity on the surface can be calculated as 14 MW/cm^2 , which is comparable to the surface damage threshold reported in the literature [144]. Therefore, we investigated the modifications formed in 3D NLL configuration [19] that prevents surface damage.

We tested pulse energies up to $20 \mu\text{J}$ to find subsurface damage threshold with multi-shots in 3D-NLL configuration. At 150 kHz, scanning speed of 0.1 mm/sec corresponds to ~ 3000 pulses in beam spot. At a fixed depth, $\Delta x = 170 \mu\text{m}$, and in transverse writing mode, we scanned parallel lines with $40 \mu\text{m}$ separation and investigated the morphology change of laser-induced region with IR transmission microscope. With this parameter set, we couldn't observe modifications below $8 \mu\text{J}$. Close to threshold energy, modification formation is relatively random and little perturbation in the process can result in no modification. As the energy increases further, controllability of the process increases (Fig. 6.8). Considering nonzero linear absorption due to doping concentration, in different depth, threshold may vary. One thing to note is that modification formation response to laser power variation is the same with what we observed in Si.

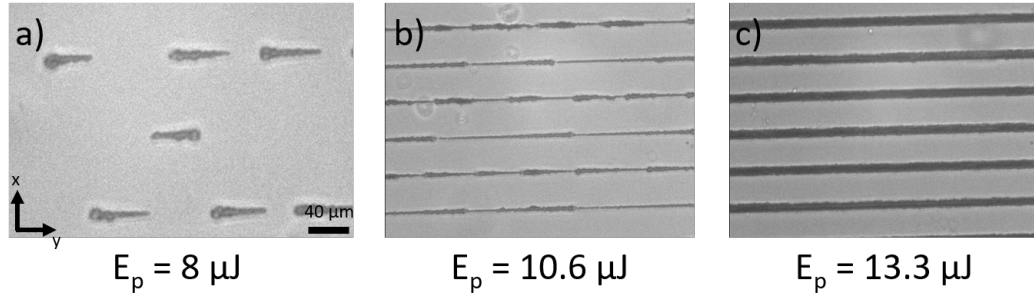


Figure 6.8: Effect of the pulse energy on the structures, (a) When the pulse energy is close to the modification threshold, random modifications are formed. (b) Above the threshold energy, modifications get more continuous with relatively lower uniformity. (c) Uniformity increases as the energy increases further. Laser propagation direction is $+z$, scanning direction is alternating between $+y$ and $-y$ with each line.

Another parameter that effects the modifications is the polarization. Preliminary analysis showed that polarization direction with respect to scanning direction can determine nanograting formation. Although linear polarization produces permanent changes deep inside GaAs, independent of scanning direction, morphology of the laser-induced structures are different. Nanostructuring is possible when the polarization is perpendicular to the scanning direction. We used the same parameters whose results are shown in Fig. 6.8 with a fixed pulse energy of $12 \mu\text{J}$. To investigate the structures, we cut them perpendicular to the scanning direction (in $+x$ direction) and imaged with high resolution SEM. We observed sub-micron modification as narrow as 300 nm with a periodicity of 500 nm , which is equal to λ/n , whereas beam waist is $2 \mu\text{m}$ (Fig. 6.9). Such nanometer scale modifications are indications of nonlinear effects such as beam collapsing and self-organization. Moreover, from a structural point of view, polarization dependent modifications in GaAs are very similar with self-organized nanogratings in glass [126, 145–147].

Further, we investigated refractive index change induced in the laser modified region. We scanned the sample as explained previously and we imaged the structures with IR transmission microscope. By moving the imaging plane $120 \mu\text{m}$ away from the modification plane in both directions, we observed an intensity contrast change, characteristics to positive refractive index change, $\Delta n >$

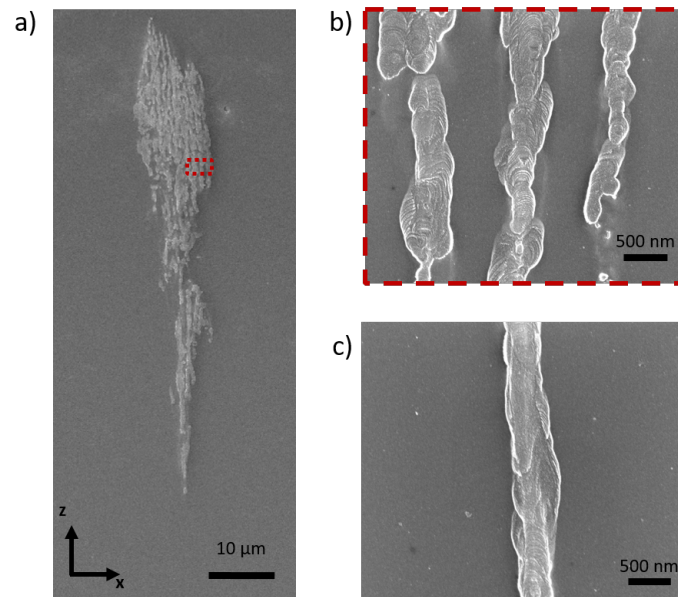


Figure 6.9: SEM image of nanogratings (a) Cross-section image of the buried structures. (b) Zoomed in image of periodic nanostructures in (a). (c) Towards the end of the modification, single nanostructures are also possible. Laser propagation direction is z , scanning direction is y .

0, in the laser-modified region. This opens up new possibilities in building buried photonic devices in GaAs, similar to what we demonstrated earlier in Si.

Chapter 7

Conclusion

In the first part of our study, we provide the foundations for generating modifications deep inside silicon with the nanosecond pulses. For the experimental parameters we used, we showed that the dominant carrier generation mechanism is two photon absorption and other mechanisms such as avalanche ionization can be neglected. Similarly, we calculated that Auger recombination is the main mechanism that decreases the free carrier density. We showed that thermal lensing due to $\Delta n_{thermal}$ and free carrier induced diffraction due to Δn_{FCI} are two major competing diffractive effects. The nonlinear coupling during the interaction of two counter-propagating beams favors thermal lensing so that the beam self-focuses. Moreover, we simulated this configuration by solving the nonlinear paraxial equation together with the heat equation to predict how carrier and temperature profiles evolve. Further, we developed a simple model that explains the structure formation and the shift in the focal points of the next pulses due to previously modified area. Experimental results are consistent with that the predictions hold.

In the experimental part of the study, we used the in-chip modifications as building blocks to fabricate functional optical elements inside silicon. First, we demonstrated diffractive optical elements, namely binary and grayscale Fourier

holograms and binary Fresnel hologram. To this end, we modified adaptive-additive iterative Fourier transform algorithm to improve the hologram quality. Briefly, we added random phase to increase the degree of freedom that the algorithm uses. With the new algorithm, we implemented a binary Fourier hologram that projects an image with high spatial frequencies. We further modified the algorithm for the generation of Fresnel holograms, which are superior in forming 3D images than the Fourier holograms. We considered a 3D image as a combination of images at different depths and generated each image as Fourier hologram. We superimposed these Fourier holograms with Fresnel zone plates into a single hologram such that each image can be reconstructed at a different depth. This method enabled us to generate four on-axis images with a single binary Fresnel hologram buried in silicon. In an extension of this study, I contributed to the development of a new algorithm for grayscale Fresnel hologram generation. The orthogonality of the random vectors in high dimensions was to eliminate the crosstalk between the consecutive reconstructed images. This resulted in unprecedented improvement in the number of projection layers, from 3-4 layers to $\sim 10^3$ layers. The maximum number of layers is not limited by the algorithm but the total pixel number, indicating that as the new devices with higher pixel numbers become available, the number of layers inherently increase.

As the second functional optical element, we fabricated waveguides inside silicon with two different configurations. In the first configuration, we used the negative refractive index change induced by the nanosecond pulses to form the tubular cladding of the waveguide. This architecture has advantages and is expected to have low losses, since its core is formed by the unmodified crystal silicon. We fabricated ~ 3 mm long waveguides with $30 \mu\text{m}$ core diameter and $20 \mu\text{m}$ cladding thickness. We measured NA of the waveguide as 0.034, corresponding to the refractive index difference of $\sim 2 \times 10^{-4}$. We characterized the optical losses with two different measurements. In the first method, we used the scattered light intensity in the direction perpendicular to the light propagation. Slope of the intensity drop resulted in a loss coefficient of ≈ 2.2 dB/cm. In the second method, we measured the coupled power from the waveguide output and by taking account of the other losses, we calculated the loss coefficient as ≈ 1.4 dB/cm. These

values are the lowest reported loss coefficients for buried silicon waveguides, to the best of our knowledge. In the second configuration, we modified the bulk silicon with femtosecond pulses to form the waveguide core. Calculated positive refractive index change of 3.5×10^{-4} from NA was confirmed with inverse-Abel transform calculation. 5.5 mm-long waveguides were predicted to have lower loss coefficients than 6 dB/cm.

In parallel to the fabrication of buried optical elements, the method we developed allows another set of applications with the help of selective etching. The morphological change induced by the laser exposure can be etched away using specific etchants. An acid based etchant that can “attack” the modified region with high selectivity was developed. It includes two chemicals that balance the electrochemical process for less rough interfaces. With the etchant, we demonstrated micropillars covering a large area with high uniformity. The roughness of the etched interfaces was estimated $\sim 1 \mu\text{m}$. Further, we demonstrated 50- μm radius through-Si vias that extend 200 μm with high reproducibility. We also carved microfluidic channels with few hundreds of micron side length with an etching rate of 500 $\mu\text{m}/\text{hour}$. To exemplify the capability, we fabricated a 8-mm long microchannel and used it to cool a chip.

We investigated the possibility of new processing regimes for in-chip Si modifications. One approach was to use Bessel beam instead of Gaussian beam. Submicron beam diameters are within reach with Bessel beams due to their profile. We generated Bessel beams using a spatial light modulator and a 4f system. We tested both longitudinal and transverse writing schemes to analyze the variations in the depth of field and the beam diameter with respect to the divergence angle of the virtual axicon. We observed that Bessel beams can routinely generate submicron structures, which is several times smaller than what Gaussian beam with the same focusing generates. Another interesting observation was that quasi-periodic voids reside in the modification region. The second approach was to use a laser operating at 2 μm . Nonlinear Kerr index of silicon maximizes around 2 μm , which potentially affects the pulse propagation and carrier density evolution in silicon. We measured the modification threshold with nanosecond pulses at 2 μm as 0.15 GW/cm^2 , which is lower than the modification threshold

at 1.55 μm . Further, we developed a new thulium-doped fiber amplifier system operating in burst mode to study femtosecond pulse interaction in silicon at 2 μm wavelength. Finally, we extended the method we developed to GaAs. We obtained periodic nanostructures in GaAs with positive refractive index change.

Further optimization of the method we developed may result in both performance increase in the currently demonstrated devices and new set of applications. For instance, higher refractive index difference generation enables curved waveguides with high bend radius or the pixel density of a hologram can be scaled up by decreasing the feature size. Further improvements of in-chip holograms can pave the way for application in adaptive optics.

In addition the combined use of two existing applications might lead to a new set of applications. In-chip waveguides and buried microchannels on the same chip can have applications in optofluidics. Moreover, curved microfluidic channels can have applications in local temperature control of a chip and can be used to tune optical or electrical properties of the devices within the same wafer.

Spatial control of the modifications with Bessel beams can provide precise phase control and create opportunity for the new hologram designs. The same property can also be used for fabricating microchannels with controllable widths.

We think that the capability we demonstrated in this thesis is a stepping stone for high performance photonic device fabrication which are necessary for electronic-photonic integration as well as other technological improvements.

Bibliography

- [1] D. Liang, G. Roelkens, R. Baets, and J. E. Bowers, “Hybrid integrated platforms for silicon photonics,” *Materials*, vol. 3, no. 3, pp. 1782–1802, 2010.
- [2] E. Kuramochi, K. Nozaki, A. Shinya, K. Takeda, T. Sato, S. Matsuo, H. Taniyama, H. Sumikura, and M. Notomi, “Large-scale integration of wavelength-addressable all-optical memories on a photonic crystal chip,” *Nature Photonics*, vol. 8, no. 6, pp. 474–481, 2014.
- [3] B. Jalali and S. Fathpour, “Silicon photonics,” *Journal of Lightwave Technology*, vol. 24, no. 12, pp. 4600–4615, 2006.
- [4] A. J. Pedraza, J. D. Fowlkes, and D. H. Lowndes, “Silicon microcolumn arrays grown by nanosecond pulsed-excimer laser irradiation,” *Applied Physics Letters*, vol. 74, no. 16, pp. 2322–2324, 1999.
- [5] G. D. Tsibidis, M. Barberoglou, P. A. Loukakos, E. Stratakis, and C. Fotakis, “Dynamics of ripple formation on silicon surfaces by ultrashort laser pulses in subablation conditions,” *Physical Review B*, vol. 86, p. 115316, Sep 2012.
- [6] M. Shen, J. E. Carey, C. H. Crouch, M. Kandyla, H. A. Stone, and E. Mazur, “High-density regular arrays of nanometer-scale rods formed on silicon surfaces via femtosecond laser irradiation in water,” *Nano Letters*, vol. 8, no. 7, pp. 2087–2091, 2008.

- [7] A. Serpenguzel, A. Kurt, I. Inanc, J. Carey, and E. Mazur, “Luminescence of black silicon,” *Journal of Nanophotonics*, vol. 2, no. 1, pp. 021770–021770–9, 2008.
- [8] A. Y. Vorobyev and C. Guo, “Laser turns silicon superwicking,” *Optics Express*, vol. 18, no. 7, pp. 6455–6460, 2010.
- [9] H. Misawa and S. Juodkasis, eds., *3D Laser Microfabrication*. Wiley-VCH Verlag GmbH & Co. KGaA, 2006.
- [10] R. R. Gattass and E. Mazur, “Femtosecond laser micromachining in transparent materials,” *Nature Photonics*, vol. 2, pp. 219–225, 2008.
- [11] B. C. Stuart, M. D. Feit, S. Herman, A. M. Rubenchik, B. W. Shore, and M. D. Perry, “Nanosecond-to-femtosecond laser-induced breakdown in dielectrics,” *Physical Review B*, vol. 53, pp. 1749–1761, 1996.
- [12] C. W. Carr, H. B. Radousky, A. M. Rubenchik, M. D. Feit, and S. G. Demos, “Localized dynamics during laser-induced damage in optical materials,” *Physical Review Letters*, vol. 92, pp. 87401–1–87401–4, Feb 2004.
- [13] K. Davis, K. Miura, N. Sugimoto, and K. Hirao, “Writing waveguides in glass with a femtosecond laser,” *Optics Letters*, vol. 21, pp. 1729–1731, 1996.
- [14] Y. Nasu, M. Kohtoku, and Y. Hibino, “Low-loss waveguides written with a femtosecond laser for flexible interconnection in a planar light-wave circuit,” *Optics Letters*, vol. 30, no. 7, pp. 723–725, 2005.
- [15] A. Kowalewicz, V. Sharma, E. Ippen, J. Fujimoto, and K. Minoshima, “Three-dimensional photonic devices fabricated in glass by use of a femtosecond laser oscillator,” *Optics Letters*, vol. 30, pp. 1060–1062, 2005.
- [16] G. D. Marshall, A. Politi, J. C. F. Matthews, P. Dekker, M. Ams, M. J. Withford, and J. L. O’Brien, “Laser written waveguide photonic quantum circuits,” *Optics Express*, vol. 17, pp. 12546–12554, Jul 2009.

- [17] S. Nolte, M. Will, J. Burghoff, and A. Tuennermann, “Femtosecond waveguide writing: a new avenue to three-dimensional integrated optics,” *Appl. Phys. A Mater. Sci. Process.*, vol. 77, pp. 109–111, June 2003.
- [18] G. Corrielli, A. Crespi, R. Geremia, R. Ramponi, L. Sansoni, A. Santinelli, P. Mataloni, F. Sciarrino, and R. Osallame, “Rotated waveplates in integrated waveguide optics,” *Nature communications*, vol. 5, 2014.
- [19] O. Tokel, A. Turnali, G. Makey, P. Elahi, T. Çolakoglu, E. Ergecen, Ö. Yavuz, R. Hübner, M. Z. Borra, I. Pavlov, A. Bek, R. Turan, D. K. Kesim, S. Tozburun, S. Ilday, and F. Ö. Ilday, “In-chip microstructures and photonic devices fabricated by nonlinear laser lithography deep inside silicon,” *Nature Photonics*, vol. 11, no. 10, pp. 639–645, 2017.
- [20] I. Pavlov, E. Dulgergil, E. Ilbey, and F. Ö. Ilday, “Diffraction-limited, 10-W, 5-ns, 100-kHz, all-fiber laser at 1.55 μm ,” *Optics Letters*, vol. 39, no. 9, pp. 2695–2698, 2014.
- [21] A. Turnali, O. Tokel, I. Pavlov, and F. Ö. Ilday, “Direct laser writing of volume Fresnel zone plates in silicon,” *European Conference on Lasers and Electro-Optics - European Quantum Electronics Conference, paper CM-4-5*, 2015.
- [22] A. H. Nejadmalayeri, P. R. Herman, J. Burghoff, M. Will, S. Nolte, and A. Tuennermann, “Inscription of optical waveguides in crystalline silicon by mid-infrared femtosecond laser pulses,” *Optics Letters*, vol. 30, no. 9, pp. 964–966, 2005.
- [23] S. Leyder, D. Grojo, P. Delaporte, W. Marine, M. Sentis, and O. Utéza, “Multiphoton absorption of 1.3 μm wavelength femtosecond laser pulses focused inside Si and SiO₂,” in *Seventeenth International School on Quantum Electronics: Laser Physics and Applications* (T. N. Dreischuh and A. T. Daskalova, eds.), pp. 877004–8, SPIE, Mar. 2013.
- [24] A. Mouskeftaras, A. V. Rode, R. Clady, M. Sentis, O. Uteza, and D. Grojo, “Self-limited underdense microplasmas in bulk silicon induced by ultrashort laser pulses,” *Applied Physics Letters*, vol. 105, no. 19, p. 191103, 2014.

- [25] V. V. Kononenko, V. V. Konov, and E. M. Dianov, “Delocalization of femtosecond radiation in silicon,” *Optics Letters*, vol. 37, pp. 3369–3372, 2012.
- [26] D. Grojo, A. Mouskeftaras, P. Delaporte, and S. Lei, “Limitations to laser machining of silicon using femtosecond micro-Bessel beams in the infrared,” *Journal of Applied Physics*, vol. 117, pp. 153105–153112, 2015.
- [27] Y. Ito, H. Sakashita, R. Suzuki, M. Uewada, K. P. Luong, and R. Tanabe, “Modification and machining on back surface of a silicon substrate by femtosecond laser pulses at 1552 nm,” *Journal of Laser Micro Nanoengineering*, vol. 9, no. 2, pp. 98–102, 2014.
- [28] I. Pavlov, E. Dulgergil, E. Ilbey, and F. Ö. Ilday, “10 W, 10 ns, 50 kHz all-fiber laser at 1.55 μm ,” *Conference on Lasers and Electro-Optics 2012, paper CTu2M.5*, May 2012.
- [29] O. Tokel, A. Turnali, I. Pavlov, S. Tozburun, I. Akca, and F. Ö. Ilday, “Laser-writing in silicon for 3D information processing,” *arXiv.org*, Sept. 2014.
- [30] P. C. Verburg, G. R. B. E. Romer, and A. J. Huis in’t Veld, “Two-photon-induced internal modification of silicon by erbium-doped fiber laser,” *Optics Express*, vol. 22, no. 18, pp. 21958–21971, 2014.
- [31] M. Chambonneau, Q. Li, M. Chanal, N. Sanner, and D. Grojo, “Writing waveguides inside monolithic crystalline silicon with nanosecond laser pulses,” *Optics Letters*, vol. 41, no. 21, pp. 4875–4878, 2016.
- [32] A. Turnali, M. Han, and O. Tokel, “Laser-written depressed-cladding waveguides deep inside bulk silicon,” *Journal of Optical Society of America B*, vol. 36, no. 4, pp. 966–970, 2019.
- [33] B. Öktem, I. Pavlov, S. Ilday, H. Kalaycıoğlu, A. Rybak, S. Yavaş, M. Erdoğan, and F. Ö. Ilday, “Nonlinear laser lithography for indefinitely large-area nanostructuring with femtosecond pulses,” *Nature Photonics*, vol. 7, no. 11, pp. 897–901, 2013.

- [34] M. S. Tyagi and R. V. Overstraeten, “Minority carrier recombination in heavily-doped silicon,” *Solid State Electronics*, vol. 26, no. 6, pp. 577–597, 1983.
- [35] N. G. Nilsson, “Band-to-band auger recombination in silicon and germanium,” *Physica Scripta*, vol. 8, no. 4, p. 165, 1973.
- [36] J. Dziewior and W. Schmid, “Auger coefficients for highly doped and highly excited silicon,” *Applied Physics Letters*, vol. 31, no. 5, pp. 346–348, 1977.
- [37] N. D. Arora, J. R. Hauser, and D. J. Roulston, “Electron and hole mobilities in silicon as a function of concentration and temperature,” *IEEE Transactions on Electron Devices*, vol. 29, no. 2, pp. 292–295, 1982.
- [38] R. F. Wood and G. E. Giles, “Macroscopic theory of pulsed-laser annealing. i. thermal transport and melting,” *Phys. Rev. B*, vol. 23, pp. 2923–2942, Mar 1981.
- [39] H. R. Shanks, P. D. Maycock, P. H. Sidles, and G. C. Danielson, “Thermal conductivity of silicon from 300 to 1400 K,” *Phys. Rev.*, vol. 130, pp. 1743–1748, Jun 1963.
- [40] H. M. van Driel, “Kinetics of high-density plasmas generated in si by 1.06- and 0.53- μm picosecond laser pulses,” *Phys. Rev. B*, vol. 35, pp. 8166–8176, May 1987.
- [41] M. C. Downer and C. V. Shank, “Ultrafast heating of silicon on sapphire by femtosecond optical pulses,” *Phys. Rev. Lett.*, vol. 56, pp. 761–764, Feb 1986.
- [42] R. Soref and B. Bennett, “Electrooptical effects in silicon,” *IEEE Journal of Quantum Electronics*, vol. 23, pp. 123–129, Jan 1987.
- [43] P. J. Timans, “Emissivity of silicon at elevated temperatures,” *Journal of Applied Physics*, vol. 74, no. 10, pp. 6353–6364, 1993.
- [44] R. Bekenstein, R. Schley, M. Mutzafi, C. Rotschild, and M. Segev, “Optical simulations of gravitational effects in the Newton-Schrödinger system,” *Nature Physics*, vol. 11, no. 10, pp. 872–878, 2015.

- [45] A. D. Bristow, N. Rotenberg, and H. M. van Driel, “Two-photon absorption and Kerr coefficients of silicon for 850-2200 nm,” *Applied Physics Letters*, vol. 90, no. 19, p. 191104, 2007.
- [46] G. Cocorullo and I. Rendina, “Thermo-optical modulation at 1.5 μm in silicon etalon,” *Electronics Letters*, vol. 28, pp. 83–85, Jan 1992.
- [47] M. R. Watts, J. Sun, C. DeRose, D. C. Trotter, R. W. Young, and G. N. Nielson, “Adiabatic thermo-optic Mach-Zehnder switch,” *Optics Letters*, vol. 38, pp. 733–735, Mar 2013.
- [48] A. Brodeur, C. Y. Chien, F. A. Ilkov, S. L. Chin, O. G. Kosareva, and V. P. Kandidov, “Moving focus in the propagation of ultrashort laser pulses in air,” *Optics Letters*, vol. 22, no. 5, pp. 304–306, 1997.
- [49] G. Agrawal, *Nonlinear Fiber Optics*. Academic Press, Boston, 2013.
- [50] A. Couarion, , and A. Mysyrowicz, “Femtosecond filamentation in transparent media,” *Physics Reports*, vol. 441, no. 2-4, pp. 47–189, 2007.
- [51] J. Leuthold, C. Koos, and W. Freude, “Nonlinear silicon photonics,” *Nature Photonics*, vol. 4, pp. 535–544, 2010.
- [52] J. Verdeyen, *Laser Electronics (2nd Edition)*. Prentice-Hall International Edition, 1989.
- [53] B. E. A. Saleh and M. C. Teich, *Fundamentals of Photonics*. Wiley Series in Pure and Applied Optics, Wiley, 2007.
- [54] S. A. Benton and J. V. Michael Bove, *Holographic Imaging*. John Wiley and Sons, 2008.
- [55] R. Soref, “Mid-infrared photonics in silicon and germanium,” *Nature Photonics*, vol. 4, pp. 495–497, Aug 2010.
- [56] D. G. Grier, “A revolution in optical manipulation,” *Nature*, vol. 424, pp. 810–816, 2003.

- [57] J. Rosen and G. Brooker, “Non-scanning motionless fluorescence three-dimensional holographic microscopy,” *Nature Photonics*, vol. 2, pp. 190–195, 2008.
- [58] S. Reichelt, R. Häussler, G. Fütterer, N. Leister, H. Kato, N. Usukura, and Y. Kanbayashi, “Full-range, complex spatial light modulator for real-time holography,” *Optics Letters*, vol. 37, no. 11, pp. 1955–1957, 2012.
- [59] L. Pugliese and G. M. Morris, “Computer-generated holography in photorefractive materials,” *Optics Letters*, vol. 15, no. 6, pp. 338–340, 1990.
- [60] S. Larouche, Y.-J. Tsai, T. Tyler, N. M. Jokerst, and D. R. Smith, “Infrared metamaterial phase holograms,” *Nature Materials*, vol. 11, pp. 450–454, 2012.
- [61] Y. Li, Y. Dou, R. An, H. Yang, and A. Q. Gong, “Permanent computer-generated holograms embedded in silica glass by femtosecond laser pulses,” *Optics Express*, vol. 13, pp. 2433–2438, 2005.
- [62] Z. Guo, S. Qu, and S. Liu, “Generating optical vortex with computer-generated hologram fabricated inside glass by femtosecond laser pulses,” *Optics Communications*, vol. 273, pp. 286–289, 2007.
- [63] J. F. Heanue, M. C. Bashaw, and L. Hesselink, “Volume holographic storage and retrieval of digital data,” *Science*, vol. 265, no. 5173, pp. 749–752, 1994.
- [64] P.-A. Blanche, A. Bablumian, R. Voorakaranam, C. Christenson, W. Lin, T. Gu, D. Flores, P. Wang, W.-Y. Hsieh, M. Kathaperumal, B. Rachwal, O. Siddiqui, J. Thomas, R. A. Norwood, M. Yamamoto, and N. Peyghambarian, “Holographic three-dimensional telepresence using large-area photorefractive polymer,” *Nature*, vol. 468, pp. 80–83, 2010.
- [65] J. W. Goodman, *Introduction to Fourier Optics*. Roberts and Company, 2005.
- [66] E. R. Dufresne, G. C. Spalding, M. T. Dearing, S. A. Sheets, and D. G. Grier, “Computer generated holographic optical tweezer arrays,” *Review of Scientific Instruments*, vol. 72, no. 3, pp. 1810–1816, 2001.

- [67] G. Makey, M. S. El-Daher, and K. Al-Shufi, “Utilization of a liquid crystal spatial light modulator in a gray scale detour phase method for fourier holograms,” *Applied Optics*, vol. 51, no. 32, pp. 7877–7882, 2012.
- [68] V. K. Soifer and L. Doskolovich, *Iterative Methods for Diffractive Optical Elements Computation*. Taylor and Francis, 1997.
- [69] E. G. Loewen and E. Popov, *Diffraction Gratings and Applications*. Marcel Dekker Inc., 1997.
- [70] R. G. Dorsch, A. W. Lohmann, and S. Sinzinger, “Fresnel ping-pong algorithm for two-plane computer-generated hologram display,” *Applied Optics*, vol. 33, pp. 869–875, 1994.
- [71] B. J. Jackin and T. Yatagai, “360° reconstruction of a 3D object using cylindrical computer generated holography,” *Applied Optics*, vol. 50, pp. 147–152, 2011.
- [72] S. C. Kim and E. S. Kim, “Fast computation of hologram patterns of a 3D object using run-length encoding and novel look-up table methods,” *Applied Optics*, vol. 48, pp. 1030–1041, 2009.
- [73] P. W. M. Tsang and T. C. Poon, “Review on the state-of-the-art technologies for acquisition and display of digital holograms,” *IEEE Transactions on Industrial Informatics*, vol. 12, pp. 886–901, 2016.
- [74] H. Yu, K. Lee, J. Park, and y. Park, “Ultrahigh-definition dynamic 3d holographic display by active control of volume speckle fields,” *Nature Photonics*, vol. 11, pp. 186–192, 2017.
- [75] G. Makey, O. Yavuz, D. K. Kesim, A. Turnalı, P. Elahi, S. Ilday, O. Tokel, and F. Ö. Ilday, “Breaking crosstalk limits to dynamic holography using orthogonality of high-dimensional random vectors,” *Nature Photonics*, vol. 13, pp. 251–256, 2019.
- [76] F. Chen and J. R. V. Aldana, “Optical waveguides in crystalline dielectric materials produced by femtosecond-laser micromachining,” *Laser and Photonics Reviews*, vol. 8, no. 2, pp. 251–275, 2014.

- [77] A. Demircan, C. Reinhardt, U. Morgner, and W. M. Pätzold, “Cascaded-focus laser writing of low-loss waveguides in polymers,” *Optics Letters*, vol. 41, no. 6, pp. 1269–1272, 2016.
- [78] S. J. B. Yoo, B. Guan, and R. P. Scott, “Heterogeneous 2D/3D photonic integrated microsystems,” *Microsystems and Nanoengineering*, vol. 2, pp. 16030–9, 2016.
- [79] S. Gross and M. J. Withford, “Ultrafast-laser-inscribed 3D integrated photonics: challenges and emerging applications,” *Nanophotonics*, vol. 4, no. 3, pp. 332–352, 2015.
- [80] A. A. Said, G. Li, K. A. Winick, M. Dugan, and P. Bado, “Waveguide electro-optic modulator in fused silica fabricated by femtosecond laser direct writing and thermal poling,” *Optics Letters*, vol. 31, no. 6, pp. 739–741, 2006.
- [81] G. Della Valle, R. Osellame, and P. Laporta, “Micromachining of photonic devices by femtosecond laser pulses,” *Journal of Optics A: Pure and Applied Optics*, vol. 11, no. 1, p. 013001, 2009.
- [82] R. M. Vázquez, R. Osellame, D. Nolli, C. Dongre, H. van den Vlekkert, R. Ramponi, M. Pollnau, and G. Cerullo, “Integration of femtosecond laser written optical waveguides in a lab-on-chip,” *Lab on a Chip*, vol. 9, no. 1, pp. 91–96, 2009.
- [83] Y. Bellouard, A. Champion, B. Lenssen, M. Matteucci, A. Schaap, M. Beresna, C. Corbari, M. Gecevicius, P. Kazansky, O. Chappuis, M. Kral, R. Clavel, F. Barrot, J. M. Breguet, Y. Mabillard, S. Bottinelli, M. Hopper, C. Hoenninger, E. Mottay, and J. Lopez, “The Femtoprint project,” *Journal of Laser Micro Nanoengineering*, vol. 7, no. 1, pp. 1–10, 2012.
- [84] S. Weimann, A. Perez-Leija, M. Lebugle, R. Keil, M. Tichy, M. Gräfe, R. Heilmann, S. Nolte, H. Moya-Cessa, G. Weihs, D. N. Christodoulides, and A. Szameit, “Implementation of quantum and classical discrete fractional Fourier transforms,” *Nature Communications*, vol. 7, p. 11027, 2016.

- [85] M. Heinrich, R. Keil, F. Dreisow, A. Tunnermann, A. Szameit, and S. Nolte, “Nonlinear discrete optics in femtosecond laser-written photonic lattices,” *Applied Physics B*, vol. 104, pp. 469–480, July 2011.
- [86] T. Meany, M. Gräfe, R. Heilmann, A. P. Leija, S. Gross, M. J. Steel, M. J. Withford, and A. Szameit, “Laser written circuits for quantum photonics,” *Laser and Photonics Reviews*, vol. 9, no. 4, pp. 363–384, 2015.
- [87] S. Li, P. Han, M. Shi, Y. Yao, B. Hu, M. Wang, and X. Zhu, “Low-loss channel optical waveguide fabrication in Nd⁺³-doped silicate glasses by femtosecond laser direct writing,” *Optics Express*, vol. 19, no. 24, pp. 23958–23964, 2011.
- [88] L. Tong, R. Gattass, I. Maxwell, J. Ashcom, and E. Mazur, “Optical loss measurements in femtosecond laser written waveguides in glass,” *Optics Communications*, vol. 259, no. 2, pp. 626–630, 2006.
- [89] W. Yuan, J. Lv, C. Cheng, X. Hao, and F. Chen, “Waveguides and proportional beam splitters in bulk poly(methyl methacrylate) produced by direct femtosecond laser direct writing,” *Optical Materials*, vol. 49, no. 1, pp. 110–115, 2015.
- [90] W. Patzold, A. Demircan, and U. Morgner, “Low-loss curved waveguides in polymers written with a femtosecond laser,” *Optics Express*, vol. 25, no. 1, pp. 263–270, 2017.
- [91] W. Nie, Y. Jia, J. Vazquez de Aldana, and F. Chen, “Efficient second harmonic generation in 3D nonlinear optical lattice-like cladding waveguide splitters by femtosecond laser inscription,” *Scientific Reports*, vol. 6, no. 1, pp. 22310–22320, 2016.
- [92] J. Lv, X. Hao, and F. Chen, “Green upconversion and near-infrared luminescence of femtosecond laser written waveguides in Er⁺³, MgO co-doped nearly stoichiometric LiNbO₃ crystals,” *Optics Express*, vol. 24, no. 22, pp. 25482–25490, 2016.

- [93] C. Zhang, N. Dong, J. Yang, F. Chen, J. Vazquez de Aldana, and Q. Lu, “Channel waveguide lasers in Nd:GGG crystals fabricated by femtosecond laser inscription,” *Optics Express*, vol. 19, no. 13, pp. 12503–12508, 2011.
- [94] R. Nie, W. He, C. Cheng, U. Rocha, J. Vazquez de Aldana, D. Jaque, and F. Chen, “Optical lattice-like cladding waveguides by direct laser writing: fabrication, luminescence and lasing,” *Optics Letters*, vol. 41, no. 10, pp. 2169–2172, 2016.
- [95] I. Pavlov, O. Tokel, S. Pavlova, V. Kadan, G. Makey, A. Turnali, Ö. Yavuz, and F. Ö. Ilday, “Femtosecond laser written waveguides deep inside silicon,” *Optics Letters*, vol. 42, no. 15, pp. 3028–3031, 2017.
- [96] G. Matthaus, H. Kammer, K. Lammers, C. Vetter, W. Watanabe, and S. Nolte, “Inscription of silicon waveguides using picosecond pulses,” *Optics Express*, vol. 26, no. 18, pp. 24089–24097, 2018.
- [97] P. Elahi, G. Makey, A. Turnali, O. Tokel, and F. Ö. Ilday, “1.06 μm -1.35 μm coherent pulse generation by a synchronously-pumped phosphosilicate raman fiber laser,” *2017 European Conference on Lasers and Electro-Optics and European Quantum Electronics Conference*, pp. CJ-2-1, 2017.
- [98] A. Courvoisier, M. J. Booth, and P. S. Salter, “Inscription of 3D waveguides in diamond using an ultrafast laser,” *Applied Physics Letters*, vol. 109, no. 3, 2016.
- [99] J. Martinez de Mendevil, D. Sola, J. R. Vazquez de Aldana, G. Lifante, A. H. de Aza, P. Pena, and J. I. Pena, “Ultrafast direct laser writing of cladding waveguides in the $0.8\text{CaSiO}_3\text{-}0.2\text{Ca}_3(\text{PO}_4)_2$ eutectic glass doped with Nd^{3+} ions,” *Journal of Applied Physics*, vol. 117, p. 043104, 2015.
- [100] W. Tang, W. Zhang, X. Liu, S. Liu, R. Stoian, and G. Cheng, “Tubular depressed cladding waveguide laser realized in Yb:YAG by direct inscription of femtosecond laser,” *Journal of Optics*, vol. 17, no. 3, p. 105803, 2015.
- [101] S. Rao, K. Moutzouris, M. Ebrahimzadeh, A. De Rossi, G. Gintz, M. Calligaro, V. Ortiz, and V. Berger, “Influence of scattering and two-photon

- absorption on the optical loss in GaAs-Al₂O₃ nonlinear waveguides measured using femtosecond pulses,” *IEEE Journal of Quantum Electronics*, vol. 39, pp. 478–486, 2003.
- [102] S. Eaton, H. Zhang, P. Herman, F. Yoshino, L. Shah, J. Bovatsek, and A. Arai, “Heat accumulation effects in femtosecond laser-written waveguides with variable repetition rate,” *Optics Express*, vol. 13, pp. 4708–4716, 2005.
- [103] J. Xia, A. Rossi, and T. Murphy, “Laser-written nanoporous silicon ridge waveguide for highly sensitive optical sensors,” *Optics Letters*, vol. 37, pp. 256–258, 2012.
- [104] A. Mysyrowicz, A. Couairon, and U. Keller, “Self-compression of optical pulses by filamentation,” *New Journal of Physics*, vol. 10, p. 025023, 2008.
- [105] M. R. Hutsel, C. C. Montarou, A. I. Dachevski, and T. K. Gaylord, “Algorithm performance in the determination of the refractive-index profile of optical fibers,” *Applied Optics*, vol. 47, no. 6, pp. 760–767, 2008.
- [106] K. E. Bean, “Anisotropic etching of silicon,” *IEEE Transactions on Electron Devices*, vol. 25, no. 10, pp. 1185–1193, 1978.
- [107] Z. Huang, N. Geyer, P. Werner, J. de Boor, and U. Gosele, “Metal-assisted chemical etching of silicon: a review,” *Advanced Materials*, vol. 23, no. 2, pp. 285–308, 2011.
- [108] B. Schwartz and H. Robbins, “Chemical etching of silicon,” *Journal of the Electrochemical Society*, vol. 123, no. 12, pp. 1903–1909, 1976.
- [109] D. Turner, “On the mechanism of chemically etching germanium and silicon,” *Journal of the Electrochemical Society*, vol. 107, no. 10, pp. 810–816, 1960.
- [110] S. Shih, K. H. Jung, T. Y. Hsieh, J. Sarathy, J. C. Campbell, and D. L. Kwong, “Photoluminescence and formation mechanism of chemically etched silicon,” *Applied Physics Letters*, vol. 60, no. 15, pp. 1863–1865, 1992.

- [111] A. Abbadie, J.-M. Hartmann, and F. Brunier, “A review of different and promising defect etching techniques: From Si to Ge,” *ECS Transactions*, vol. 10, no. 1, pp. 3–19, 2007.
- [112] T. Chandler, “MEMC Etch- A chromium trioxide-free etchant for delineating dislocations and slip in silicon,” *Journal of The Electrochemical Society*, vol. 137, no. 3, pp. 944–948, 1990.
- [113] Y. Wang, L. Yang, Y. Liu, Z. Mei, W. Chen, J. Li, H. Liang, A. Kuznetsov, and X. D., “Maskless inverted pyramid texturization of silicon,” *Scientific Reports*, vol. 5, p. 10843, 2015.
- [114] G. Katti, M. Stucchi, K. Meyer, and W. Dehaene, “Electrical modeling and characterization of through silicon via for three-dimensional ICs,” *IEEE Transactions on Electron Devices*, vol. 57, no. 1, pp. 256–262, 2010.
- [115] A. Shah, P. Torres, R. Tscharnner, N. Wyrsh, and H. Keppner, “Photovoltaic technology: the case for thin-film solar cells,” *Science*, vol. 285, no. 5428, pp. 692–698, 1999.
- [116] Q.-Y. Tong and U. Goesele, *Semiconductor wafer bonding: science and technology*. John Wiley, 1999.
- [117] I. Mizushima, T. Sato, S. Taniguchi, and Y. Tsunashima, “Empty-space-in-silicon technique for fabricating a silicon-on-nothing structure,” *Applied Physics Letters*, vol. 77, no. 20, pp. 3290–3292, 2000.
- [118] B. Dang, M. Bakir, D. Sekar, C. King, and J. Meindl, “Integrated microfluidic cooling and interconnects for 2D and 3D chips,” *IEEE Transactions of Advanced Packaging*, vol. 33, pp. 79–87, 2010.
- [119] P. Ball, “Feeling the heat,” *Nature*, vol. 492, pp. 174–176, 2012.
- [120] J. Hawkes and J. Wilson, *Laser principles and applications*. Prentice Hall International, 1987.
- [121] Q. Sun, H. Jiang, Y. Liu, Y. Zhou, H. Yang, and Q. Gong, “Effect of spherical aberration on the propagation of a tightly focused femtosecond laser

- pulse inside fused silica,” *Journal of Optics A: Pure and Applied Optics*, vol. 7, pp. 655–659, 2005.
- [122] M. Duocastella and C. Arnold, “Bessel and annular beams for materials processing,” *Laser and Photonics Review*, vol. 6, no. 5, pp. 607–621, 2012.
- [123] D. McGloin and K. Dholakia, “Bessel beams: Diffraction in a new light,” *Contemporary Physics*, vol. 46, no. 1, pp. 15–28, 2005.
- [124] R. Stoian, M. Bhuyan, G. Zhang, G. Cheng, R. Meyer, and F. Courvoisier, “Ultrafast Bessel beams: Advanced tools for laser material processing,” *Advanced Optical Technologies*, vol. 7, no. 3, pp. 165–174, 2018.
- [125] M. Bhuyan, F. Courvoisier, P. Lacourt, M. Jacquot, L. Furfaro, M. Withford, and J. Dudley, “High aspect ratio taper-free microchannel fabrication using femtosecond Bessel beams,” *Optics Express*, vol. 18, no. 2, pp. 566–574, 2010.
- [126] Y. Shimotsuma, P. Kazansky, J. Qiu, and K. Hirao, “Self-organized nanogratings in glass irradiated by ultrashort light pulses,” *Physical Review Letters*, vol. 91, p. 247405, 2003.
- [127] M. Deubel, G. Freynman, M. Wegener, S. Pereira, K. Busch, and C. Soukoulis, “Direct laser writing of three-dimensional photonic-crystal templates for telecommunications,” *Nature Materials*, vol. 3, pp. 444–447, 2004.
- [128] G. Zheng, H. Muhlenbernd, M. Kenney, G. Li, T. Zentgraf, and S. Zhang, “Metasurface holograms reaching 80 % efficiency,” *Nature Nanotechnology*, vol. 10, pp. 308–312, 2015.
- [129] M. Bhuyan, M. Somayaji, A. Mermillod-Blondin, F. Bourquard, J. Colombier, and R. Stoian, “Ultrafast laser nanostructuring in bulk silica, a slow microexplosion,” *Optica*, vol. 4, no. 8, pp. 951–958, 2017.
- [130] T. Wang, N. Venkatram, J. Gosciniaik, Y. Cui, G. Qian, W. Ji, and D. Tan, “Multi-photon absorption and third-order nonlinearity in silicon at mid-infrared wavelengths,” *Optics Express*, vol. 21, no. 26, pp. 32192–32198, 2013.

- [131] L. Zhang, A. Agarwal, L. Kimerling, and J. Michel, “Nonlinear group IV photonics based on silicon and germanium: from near-infrared to mid-infrared,” *Nanophotonics*, vol. 3, no. 4, pp. 257–268, 2014.
- [132] P. Elahi, H. Kalaycıoğlu, O. Akcaalan, C. Senel, and F. Ö. Ilday, “Burst-mode thulium all-fiber laser delivering femtosecond pulses at a 1 GHz intraburst repetition rate,” *Optics Letters*, vol. 42, no. 19, pp. 3808–3811, 2017.
- [133] J. K. Lucek and K. J. Blow, “Soliton self-frequency shift in telecommunications fiber,” *Physical Review A*, vol. 45, no. 9, pp. 6666–6674, 1992.
- [134] J. Luo, B. Sun, J. Ji, E. Tan, Y. Zhang, and X. Yu, “High-efficiency femtosecond Raman soliton generation with a tunable wavelength beyond 2 μm ,” *Optics Letters*, vol. 42, no. 8, pp. 1568–1571, 2017.
- [135] A. Bett, F. Dimroth, G. Stollwerck, and O. Sulima, “III-V compounds for solar cell applications,” *Applied Physics A*, vol. 69, pp. 119–129, 1999.
- [136] O. Wada, “Optoelectronic integration based on GaAs material,” *Opt. Quantum Electron.*, vol. 20, pp. 441–474, 1988.
- [137] J. Yoon, S. Jo, S. Ik, H. Jung, I. Kim, M. Meitl, E. Menard, X. Li, J. Coleman, U. Paik, and J. Rogers, “GaAs photovoltaics and optoelectronics using releasable multilayer epitaxial assemblies,” *Nature*, vol. 465, pp. 329–333, 2010.
- [138] D. Petrov, “Nonlinear phase shift by cascaded quasi-phase-matched second harmonic generation,” *Optics Communications*, vol. 131, pp. 102–106, 1996.
- [139] S. Buckley, M. Radulaski, J. Petykiewicz, K. Lagoudalis, J. Kang, M. Brongersma, K. Biermann, and J. Vuckovic, “Second-harmonic generation in GaAs photonic crystal cavities in (111)B and (001) crystal orientations,” *ACS Photonics*, no. 1, pp. 516–523, 2014.
- [140] P. Kuo, J. Bravo-Abad, and G. Solomon, “Second-harmonic generation using 4-quasi-phases matching in a GaAs whispering gallery-mode microcavity,” *Nature Communications*, vol. 5, no. 3109, 2014.

- [141] Y. Lee, N. Yu, C. Jung, and B. Yu, “Second-harmonic generation in periodically poled lithium niobate waveguides fabricated by femtosecond laser pulses,” *Applied Physics Letters*, vol. 89, p. 171103, 2006.
- [142] L. Eyres, P. Turreau, T. Pinquet, C. Ebert, J. Harris, M. Fejer, L. Becouarn, B. Gerard, and E. Lallier, “All-epitaxial fabrication of thick, orientation-patterned GaAs films for nonlinear optical frequency conversion,” *Applied Physics Letters*, vol. 79, p. 904, 2001.
- [143] P. Karpinski, X. Chen, V. Shvedov, C. Hnatovsky, A. Grisard, E. Lallier, B. Luther-Davies, W. Krolikowski, and Y. Sheng, “Nonlinear diffraction in orientation-patterned semiconductors,” *Optics Express*, vol. 23, no. 11, pp. 14903–14912, 2015.
- [144] A. Huang, M. Becker, and R. Walser, “Laser-induced damage and ion emission of GaAs at 1.06 μm ,” *Applied Optics*, vol. 25, no. 21, pp. 3864–3870, 1986.
- [145] W. Yang, E. Bricchi, P. Kazansky, J. Bovatsek, and A. Arai, “Self-assembled periodic sub-wavelength structures by femtosecond laser direct writing,” *Optics Express*, vol. 14, no. 21, pp. 10117–10124, 2006.
- [146] Y. Dai, G. Wu, X. Lin, G. Ma, and J. Qui, “Femtosecond laser induced rotated 3D self-organized nanograting in fused silica,” *Optics Express*, vol. 20, no. 16, pp. 18072–18078, 2012.
- [147] V. R. Bhardwaj, E. Simova, P. P. Rajeev, C. Hnatovsky, R. S. Taylor, D. M. Rayner, and P. B. Corkum, “Optically produced arrays of planar nanostructures inside fused silica,” *Physical Review Letters*, vol. 96, p. 057404, 2006.

Appendix A

Paraxial approximation for nonlinear wave equation

Helmoltz Eqn:

$$\left(\nabla^2 + n^2 \frac{\omega^2}{c^2}\right) \vec{E} = 0 \quad (\text{A.1})$$

Substitute in $E(x, y)$ with $A(x, y) e^{ikz}$ in Eqn. (1):

$$\left(\partial_x^2 + \partial_y^2 + \partial_z^2 + n^2 \frac{\omega^2}{c^2}\right) A(x, y) e^{ikz} = 0 \quad (\text{A.2})$$

$$\left(\partial_x^2 + \partial_y^2 + n^2 \frac{\omega^2}{c^2}\right) A(x, y) e^{ikz} + \partial_z^2 A(x, y) e^{ikz} = 0 \quad (\text{A.3})$$

$$\left(\partial_x^2 + \partial_y^2 + n^2 \frac{\omega^2}{c^2}\right) A(x, y) e^{ikz} + [\partial_z^2 A(x, y)] e^{ikz} + 2ik [\partial_z A(x, y)] e^{ikz} - k^2 A(x, y) e^{ikz} = 0 \quad (\text{A.4})$$

Since $|\partial_z^2 A| \ll |k \partial_z A|$ (Paraxial approximation)

$$(\partial_x^2 + \partial_y^2) A(x, y) e^{ikz} + 2ik \partial_z A(x, y) e^{ikz} + \left(n^2 \frac{\omega^2}{c^2} - k^2\right) A(x, y) e^{ikz} = 0 \quad (\text{A.5})$$

Substitute n with $n + \Delta n$, where Δn is nonlinear perturbation.

$$\nabla_{\perp}^2 A(x, y) e^{ikz} + 2ik\partial_z A(x, y) e^{ikz} + \left(n^2 \frac{\omega^2}{c^2} + 2n\Delta n \frac{\omega^2}{c^2} + \Delta n^2 \frac{\omega^2}{c^2} - k^2 \right) A(x, y) e^{ikz} = 0 \quad (\text{A.6})$$

Neglecting the higher order Δn term under the assumption of $|\Delta n^2| \ll |\Delta n|$ reads,

$$\nabla_{\perp}^2 A(x, y) e^{ikz} + 2ik\partial_z A(x, y) e^{ikz} + \left(k^2 + \Delta n \frac{2n\omega^2}{c^2} - k^2 \right) A(x, y) e^{ikz} = 0 \quad (\text{A.7})$$

$$\nabla_{\perp}^2 A(x, y) e^{ikz} + 2ik\partial_z A(x, y) e^{ikz} + 2 \frac{k^2 \Delta n}{n} A(x, y) e^{ikz} = 0 \quad (\text{A.8})$$

$$i\partial_z A(x, y) e^{ikz} + \frac{1}{2k} \nabla_{\perp}^2 A(x, y) e^{ikz} + \frac{k\Delta n}{n} A(x, y) e^{ikz} = 0 \quad (\text{A.9})$$

Finally, substituting $A(x, y)$ with $E(x, y) e^{-ikz}$ back yields,

$$i\partial_z E + \frac{1}{2k} \nabla_{\perp}^2 E + \frac{k\Delta n}{n} E = 0 \quad (\text{A.10})$$